

4

GA-A19800

HIGH-TEMPERATURE CERAMIC SUPERCONDUCTORS

FOR PERIOD
MAY 24, 1988 TO JUNE 31, 1989

ANNUAL REPORT

Prepared for
OFFICE OF NAVAL RESEARCH
1400 WILSON BOULEVARD
ARLINGTON, VIRGINIA 22217-5000

DARPA/ONR CONTRACT N00014-88-C-0714

APPROVED FOR PUBLIC RELEASE

DTIC
ELECTE
AUG 02 1989
S D

Prepared by
K.S. MAZDIYASNI, PROGRAM MANAGER

K.C. CHEN
W.J. DeHOPE
D.M. DUGGAN
E.Y. GLATTER
Y.R. LIN-LIU
B.W. McQUILLAN

F.C. MONTGOMERY
S.S. PAK
R.B. STEPHENS
P.K. TSAI (UCSD)
L. PAULIUS (UCSD)

The views and conclusions contained in this document are those of the authors and should not be interpreted as necessarily representing the official policies, either expressed or implied, of the Defense Advanced Research Projects Agency or the U.S. Government.

APPROVED BY: 
T.D. GULDEN
DIRECTOR, DEFENSE MATERIALS



GENERAL ATOMICS

REPORT DOCUMENTATION PAGE

Form Approved
OMB No. 0704-0188

1a. REPORT SECURITY CLASSIFICATION Unclassified			1b. RESTRICTIVE MARKINGS	
2a. SECURITY CLASSIFICATION AUTHORITY			3. DISTRIBUTION / AVAILABILITY OF REPORT Unlimited	
2b. DECLASSIFICATION / DOWNGRADING SCHEDULE				
4. PERFORMING ORGANIZATION REPORT NUMBER(S) GA-A19800 Project No. 3850			5. MONITORING ORGANIZATION REPORT NUMBER(S)	
6a. NAME OF PERFORMING ORGANIZATION General Atomics		6b. OFFICE SYMBOL (If applicable) DARPA		7a. NAME OF MONITORING ORGANIZATION Office of Naval Research
6c. ADDRESS (City, State, and ZIP Code) P. O. Box 85608 San Diego, CA 92138			7b. ADDRESS (City, State, and ZIP Code) 800 North Quincy Avenue Arlington, VA 22217	
8a. NAME OF FUNDING / SPONSORING ORGANIZATION Defense Advanced Research Project		8b. OFFICE SYMBOL (If applicable) DARPA		9. PROCUREMENT INSTRUMENT IDENTIFICATION NUMBER N00014-88-C-0714
3c. ADDRESS (City, State, and ZIP Code) 1400 Wilson Blvd. Arlington, VA 22209			10. SOURCE OF FUNDING NUMBERS	
			PROGRAM ELEMENT NO.	PROJECT NO.
			TASK NO.	WORK UNIT ACCESSION NO.
1. TITLE (Include Security Classification) High Temperature Ceramic Superconductors				
2. PERSONAL AUTHOR(S) K. S. Mazdhyasni				
3a. TYPE OF REPORT Annual Technical Report		13b. TIME COVERED FROM 5-24-88 TO 6-30-89		14. DATE OF REPORT (Year, Month, Day) July 15, 1989
15. PAGE COUNT				
16. SUPPLEMENTARY NOTATION				
17. COSATI CODES			18. SUBJECT TERMS (Continue on reverse if necessary and identify by block number)	
FIELD	GROUP	SUB-GROUP		
			Precursor compounds, Thin Film, Electromagnetic	
			Processing, Powder High Q Cavity, properties,	
			Sol-Gel Monolith, Fiber Flux-Creep, Microstructures.	
9. ABSTRACT (Continue on reverse if necessary and identify by block number)				
<p>The principal goals of this program are (1) to demonstrate fabrication of high-temperature ceramic superconductors via sol-gel method that can operate at or above 90K with appropriate current density, J_c, in forms useful for application in resonant cavities, magnets, motors, sensors, computers, and other devices; and (2) to fabricate and demonstrate selected components made of these materials, including microwave cavities and magnetic shields.</p> <p>The chemical pathways for preparation of 123 powder, fiber and film have been identified. A new technique for synthesis of fine particle $DyBa_2Cu_3O_{7-x}$ as seed material for grain orientation in a magnetic field experiment has been developed. Monolithic powder compacts achieved $T_c \sim 91K$. The width of transition temperature is consistently $\sim 2K$. 123 gel monolith was produced.</p>				
20. DISTRIBUTION / AVAILABILITY OF ABSTRACT <input checked="" type="checkbox"/> UNCLASSIFIED/UNLIMITED <input type="checkbox"/> SAME AS RPT. <input type="checkbox"/> DTIC USERS			21. ABSTRACT SECURITY CLASSIFICATION	
22a. NAME OF RESPONSIBLE INDIVIDUAL Dr. Wallace Arden Smith			22b. TELEPHONE (Include Area Code) (202) 696-0284	22c. OFFICE SYMBOL ONR

Process parameters for production of high T_c ceramic superconductors have been developed. Sintered dense flexible sol-gel derived 123 monofilaments with diameter of 15-20 μ m have been produced. Adherent crack free 123 thin films by sol-gel dip coating method on yttria stabilized zirconia polycrystals (YSZP) has been demonstrated. Fiber microstructures and heat treatment process cycle relationships were established. The sintered powder compact critical temperature $T_c = T_{0.5} = 91K$ with a transition width $T_c = T_{0.9} - T_{0.1}$ of $>2K$ was measured. Resistivity measurements in applied magnetic field, H , up to 10T were carried out. The upper critical field slope (dH_{C2}/dT) $T_c = -2.75$ T/K for $n=0.1$, 0.5 and 0.9 were determined. The magnetic susceptibility at $H = 25$ Oe = 89K and the strength of diamagnetic signal greater than the Meisner signal by a factor of 3.9 was observed. The critical current density values of $J_c \sim 4.1 \times 10^4$ A/Cm 2 at 3 KOe and $J_c \sim 1 \times 10^4$ A/Cm 2 at 50 KOe at 5K have been calculated. GA constructed table top continuous fiber spinner, equipped with magnet with the field strength of 0.75T at 0.5 cm spacing, was completed and is operational. GA constructed automatic dip coating machine was completed and is operational. Spinning of continuous, meters in length, preceramic 123 monofilament was accomplished. Design and technique for measuring cavity quality factor Q have been identified. Theory assessment was made of flux creep on the surface resistance of high T_c ceramic superconductors.

FOREWORD

This report summarizes mostly experimental and some theoretical work conducted during the first year, May 24, 1988 to June 31, 1989, of DARPA/ONR Contract N00014-88-C-0714, High Temperature Ceramic Superconductors. Dr. Kay Adams is the DARPA program manager and Dr. Wallace Arden Smith, Materials Division, Department of the Navy, ONR, is the Navy project scientist.

Also included as part of this summary technical report is an appendix which covers more detailed experimental aspects of the work performed during the course of the research program.



Accession For		
NTIS	CRA&I	<input checked="checked" type="checkbox"/>
DTIC	TAB	<input type="checkbox"/>
Unannounced		<input type="checkbox"/>
Justification		
By		
Distribution		
Availability Codes		
Dist	Avail and/or Special	
A-1		

CONTENTS

FOREWORD	11
1. INTRODUCTION	1-1
1.1. Project Outline	1-2
2. SUMMARY OF ACCOMPLISHMENTS	2-1
2.1. Metal Alkoxide Precursor Compound Synthesis and Processing to Powders, Compact and Monolith	2-1
2.2. Sol-Gel Processing	2-1
2.3. Microstructure and Electromagnetic Property Characterization	2-2
2.4. Ceramic Superconductor Fiber and Film Processing	2-2
2.5. Component Design and Fabrication	2-2
3. PUBLICATIONS AND PRESENTATIONS	3-1
3.1. Publication	3-1
3.2. Presentation	3-1
APPENDIX A: METAL ALKOXIDE PRECURSOR COMPOUNDS SYNTHESIS AND PROCESSING	A-1
A.1. YTTRIUM AND LANTHANIDE ALKOXIDES	A-1
A.1.1. Synthesis	A-1
A.1.2. High T_c Ceramic Superconductors Powders	A-2
A.1.3. Powder Synthesis	A-4
A.1.4. Seed-Powder Synthesis	A-11
A.1.5. Sol-Gel Processing	A-11
A.1.6. Thin Films	A-17
A.1.7. Synthesis of Precursor Compounds Suited for Film and Fibers Processing	A-17
A.2. SOL-GEL COATING	A-28
A.2.1. Dip Coating	A-28
A.2.2. Sol-Gel Derived Fiber	A-30
A.2.3. Preparation of Solution Containing the Necessary Elements with Fiber and Film Forming Abilities	A-33
A.2.4. Calibration of Solution Concentrations	A-36

A.3.	FIBER HEAT TREATMENT	A-3-1
A.3.1.	Optimization of Fiber Heat Treatment Schedule .	A-3-1
A.3.2.	Further Improvement in Composition Stoichiometry	A-3-10
A.3.3.	Continuous Fiber Drawing Development	A-3-11
A.3.4.	Fiber Preferred Crystallographic-Orientation Development (Texturing)	A-3-15
A.4.	ELECTRICAL AND MAGNETIC PROPERTY DETERMINATION	A-4-1
A.4.2.	Magnetic Susceptibility	A-4-1
A.4.3.	Magnetization Measurements	A-4-5
A.4.5.	Cavity Q Measurements	A-4-15
A.5.	THE EFFECT OF FLUX CREEP ON THE SURFACE RESISTANCE OF HIGH T_c SUPERCONDUCTORS	A-5-1
A.5.1.	Introduction	A-5-1
A.5.2.	Flux Creep Equations	A-5-1
A-5.3.	Superconducting Resistance Zero Frequency . . .	A-5-6
A-5.4.	Superconducting Resistance High Frequency . . .	A-5-10
A-5.5.	Summary	A-5-14
APPENDIX II	A-II-1
A.II.1.	Minimum Flexible Length of Flux Line, s	A-II-1
A.II.2.	Distance Between Effective Pinning Centers	A-II-1
6.	REFERENCES	6-1

FIGURES

A-1.	Flow Diagram For BaYCuO High-Temperature Superconductor . .	A-3
A-2.	EDX Analysis of Cu Methoxide Powder	A-5
A-3.	XRD Patterns of 123 Powder.	A-7
A-4.	TEM Image of As-prepared Powder	A-8
A-5.	TEM Image of 123 Powder	A-9
A-6.	XRD Patterns of 123 Powder.	A-10
A-7.	TEM image of 123 Powder Heated at 750°C	A-12

A-8.	DyBa ₂ Cu ₃ O _{7-x} Powder Prepared by Pyrolysis of Solution . . .	A-13
A-9.	DyBa ₂ Cu ₃ O _{7-x} Powder Calcined	A-14
A-10.	XRD Patterns of 123 Gel-Powder	A-16
A-11.	Scanning Electron Micrograph of 123 Superconductor	A-20
A-12.	SEM Images and XRD Pattern	A-18
A-13.	Comparison of Thermal Decomposition	A-21
A-14.	X-ray Diffraction Pattern for Powder	A-23
A-15.	Weight Loss During Ramp and Hold Test	A-27
A-16.	Photomicrograph of a Coating Prepared by Dip Coating Yttria	A-29
A-17.	Photomicrograph of a Coating Prepared by Dip Coating Yttria Stabilized Zirconia	A-31
A-18.	Fiber Process Parameters.	A-32
A-19.	Flow Diagram for BaYCuO High-Temperature Superconductor . .	A-34
A-20.	Sol-gel Derived Preceramic Superconductor	A-35
A-21.	SEM Micrographs of Sol-gel Derived Ceramic Superconductor .	A-37
A-3-1.	Isothermal TGA on Preceramic Fiber	A-3-2
A-3-2.	Isothermal TGA Curve of Preceramic Fiber	A-3-3
A-3-3.	X-ray Diffraction of Sample Heat Treated at 900°C	A-3-5
A-3-4.	Time-temperature-phase Diagram	A-3-6
A-3-5.	Microstructural Evolution of the Fibers	A-3-7
A-3-6.	Effect of High Temperature Annealing of Grain Size	A-3-8
A-3-7.	Pores Formation in Fiber Using High Heating	A-3-9
A-3-8.	Dense Y123 Fiber Obtained by Proper Heat Treatment	A-3-9
A-3-9.	X-ray and DTA Characterization	A-3-12
A-3-10(a).	Continuous Preceramic Fibers	A-3-13
A-3-10(b).	Continuous Preceramic Fibers Spool	A-3-13
A-3-11.	Continuous Preceramic Fiber Prepared by Down-Drawing . .	A-3-14
A-4-1.	Resistivity, Normalized to the Value at 300 K	A-4-2
A-4-2.	Upper Critical Field H _{c2}	A-4-3
A-4-3.	Magnetic Susceptibility as a Function of Temperature . . .	A-4-4
A-4-4.	Magnetization as a Function of Magnetic Field	A-4-7
A-4-5.	Estimated Critical Current Density	A-4-8
A-4-6.	Resistance-temperature Plot	A-4-9

A-4-7. Magnetic Susceptibility for Sol-Gel	A-4-10
A-4-8. Schematic Drawing of Cavity Design	A-4-16
A-5-1. Effect of Lorentz Force	A-5-4
A-5-2. Effective Resistivity from Flux Creep	A-5-8
A-5-3. When Flux Lines are Floppy	A-5-11

TABLES

A-1. Molar Ratio of Additives	A-24
A-2. Stability and Products of Hydrolyzing Solutions	A-26
A-1-2. Calibration Tolerances	A-40
A-2-2. Alkoxide Operations and Errors	A-41
A-5-1. Material Parameters	A-5-15

1. INTRODUCTION

Three new types of ceramic superconductors have been discovered in the past two years: $\text{YBa}_2\text{Cu}_3\text{O}_7$ ($T_c \sim 95$ K) and its rare earth congeners, $\text{Bi}_2\text{Sr}_2\text{CaCu}_2\text{O}_8$ ($T_c \sim 110$ K), and $\text{Tl}_2\text{Sr}_2\text{CaCu}_2\text{O}_8$ ($T_c \sim 125$ K) (Ref. 1). The thallium material is hazardous and toxic and must be handled with great care. The bismuth material is currently synthesized within ~ 5 deg. of its melting point. The $\text{YBa}_2\text{Cu}_3\text{O}_7$ material is the most studied material, and its chemistry is the best understood. As opposed to the thallium and bismuth materials, the $\text{YBa}_2\text{Cu}_3\text{O}_7$ must be annealed in oxygen in the temperature range of 450° to 550°C , after its synthesis above 900 deg. This temperature-dependent oxygen sensitivity is a process variable which may prove useful in understanding the microstructure processing property relationships of monolith, fibers, and films.

The crystal chemistry of High Temperature Superconductors has been recently reviewed by A. W. Sleight (Ref. 2) and needs no further discussion. Various correlations between material properties and T_c have been made as oxide superconductors have been so intensively studied. Some of these correlations are so interdependent that it is difficult to sort out the truly meaningful correlations at this time.

The principal goals of this program are (1) to demonstrate fabrication of high-temperature ceramic superconductors via a sol-gel method that can operate at or above 90 K with appropriate current density, J_c , in forms useful for application in resonant cavities, magnets, motors, sensors, computers, and other devices; and (2) to fabricate and demonstrate selected components made of these materials, including microwave cavities and magnetic shields.

The General Atomics (GA) approach is to develop the sol-gel technology processing of high-temperature ceramic superconductors to make

sol-gel a viable process for fabricating high T_c (>90 K) superconductors in forms useful for applications. The nature of sol-gel processing makes it inherently amenable to fabricating the thin films and fibers that are needed for many applications. In addition, the relatively low temperature characteristics of sol-gel processing make it advantageous for many applications in which the superconducting materials must be applied to heat sensitive substrates.

The scope of the effort includes the following:

- Synthesis of sol precursors.
- Optimization of sol-gel processed material, including purity, homogeneity, stoichiometry, sintering temperatures, grain size and orientation, and dopants for grain boundary and flux pinning and for control of mechanical properties.
- Fabrication of forms, including powders, thin and thick films, and fibers.
- Evaluation of environmental stability, physical, mechanical, electrical, and magnetic properties.
- Fabrication and testing of a model component.

1.1. PROJECT OUTLINE

This program has been divided into six tasks: (1) metal alkoxide synthesis and processing, (2) microstructural evaluation and property measurement, (3) electrical and magnetic property measurement, (4) superconductor ceramic processing, (5) component fabrication and demonstration, and (6) reporting.

Task 1 is to synthesize a homogeneous metal alkoxide, $M(OR)_n$, where n is the valence of metal, M , and R is an organic group, solution that contains all the constituent elements which can be easily made to powders, thin film, or drawn into fiber form. Ideally, this solution should possess precise stoichiometry, adequate stability, polymerizability, adherence, and spinnability. Also, the polymeric materials formed from this solution should be thermosetting, be able to be dissolved in organic solvents, and contain as little as possible low-temperature pyrolyzable organics with high char yield.

Task 2 is to study the microstructure as a function of processing parameters. The study includes: density, pore size and pore size distribution, phase identification, chemical composition and purity, environmental stability, effects of heat treatment, residual strain, seeding, annealing in magnetic fields, and epitaxy on grain growth and orientation.

Task 3 is to study the electrical and magnetic properties of the $YBa_2Cu_3O_{7-x}$ (123) high T_c ceramic superconductors. It will include both the ac electrical resistance (R_{ac}) and the ac magnetic susceptibility (χ_{ac}) magnetic properties.

The dc current versus voltage curve will be measured at liquid nitrogen temperatures for all promising superconducting materials and a value for J_c (77 K) determined. For the samples with the highest values of J_c (77 K), critical currents will be measured as a function of magnetic fields of up to 8 T at temperatures between 1.4 K and near the superconducting transition temperature T_c . These data will be collected in liquid He or flowing He using a Janis Superveritemp dewar equipped with an 8 T superconducting magnet. As required, Hall effect measurements can be performed in this apparatus to determine the type and density of the current carriers. Both χ_{ac} and R_{ac} at pressures up to 20 kbar, can be used in this dewar to measure the superconducting and magnetic properties of samples at high pressures, at high magnetic fields, and at temperatures from 1.4 to 300 K.

As a subcontractor to GA, the Superconductivity and Magnetism group, under the direction of Professor M. Brian Maple, at the University of California, San Diego (UCSD), has performed the electromagnetic characterization of high-temperature superconducting oxide compounds, which are fabricated at GA. UCSD personnel have and will continue to measure the superconducting and magnetic properties by means of measurements of the upper critical magnetic field, critical current density inferred from both direct and magnetization measurements, magnetic susceptibility, Meissner effect, and specific heat.

Task 4 is an investigation of superconductor ceramic processing. Most of the important applications of superconductors require material in the form of fiber or films. Magnets, conductors, motors, and generators are examples of applications employing fiber; while detectors, microwave cavities, and microcircuitry require superconducting material in the form of films. The sol-gel process is ideally suited to producing materials in these forms; in fact, it is used commercially to produce antireflection and mirror coatings and to produce continuous ceramic fibers for structural reinforcement in composite materials and for thermal insulation.

Task 5 is to demonstrate component fabrication. GA will design and build a high Q, high T_c superconducting cavity using its unique sol-gel coating process capabilities. This task would proceed after some initial coating tests verified dc superconductivity and questions of adhesiveness, surface preparation, and processing procedures are answered. As the fabrication process and the materials quality are improved throughout the three-year program, two additional cavities will be constructed and tested. Coupling would be through a waveguide inductive iris into an end wall with a logarithmic decrement technique of Q measurement being considered most appropriate for the high Q anticipated. An X-band (10 GHz) frequency choice allows for convenient dimensions of 4.3 cm diameter by 2.8 cm height.

2. SUMMARY OF ACCOMPLISHMENTS

In the following section, a brief narrative description of the major advances that have been accomplished under each task are presented.

2.1. METAL ALKOXIDE PRECURSOR COMPOUND SYNTHESIS AND PROCESSING TO POWDERS, COMPACT AND MONOLITH

1. The chemical pathways for preparation of 123 powder, fiber, and film have been identified.
2. A new technique for synthesis of fine particle $\text{DyBa}_2\text{Cu}_3\text{O}_{7-x}$ as seed material has been developed.
3. Monolithic powder compacts achieved a $T_c \sim 91$ K. The width of transition temperature is consistently ~ 2 K.
4. 123 Gel Monolith was produced.

2.2. SOL-GEL PROCESSING

1. Process parameters for production of 123 high T_c ceramic superconductors have been developed.
2. Sintered dense flexible sol-gel derived 123 monofilaments with diameter of 15 to 20 μm have been produced.
3. Adherent crack free 123 thin film by sol-gel dip coating method on yttria stabilized zirconia polycrystals (YSZP) substrate has been demonstrated.

2.3. MICROSTRUCTURE AND ELECTROMAGNETIC PROPERTY CHARACTERIZATION

1. Grain microstructures and heat treatment process cycle relationships were established.

2. The sintered powder compact critical temperature $T_c = T_{0.5} = 91$ K with a transition width $T_c = T_{0.9} - T_{0.1}$ of < 2 K was measured; resistivity measurements in applied magnetic field, H , up to 10 T were carried out; the upper critical field slope $(dH_{c2}/dT)_{T_c} = -2.75$ T/K for $n = 0.1, 0.5$, and 0.9 were determined; the magnetic susceptibility at $H = 250$ Oe $= 89$ K and the strength of the diamagnetic signal greater than the Meissner signal by a factor of 3.9 was observed; the critical current density values of $J_c \approx 4.1 \times 10^4$ A/cm² at 3 KOe and $J_c \approx 1 \times 10^4$ A/cm² at 50 KOe at 5 K have been calculated.

2.4. CERAMIC SUPERCONDUCTOR FIBER AND FILM PROCESSING

1. GA-constructed table top continuous fiber spinner machine was completed and is operational.
2. GA-constructed automatic dip coater machine was completed and is operational.
3. Spinning of continuous meters in length preceramic 123 monofilaments was accomplished.

2.5. COMPONENT DESIGN AND FABRICATION

1. Design and technique for measuring cavity quality factor, Q , have been identified.
2. Theory assessment was made of flux creep on the surface resistance of high T_c superconductors.

3. PUBLICATIONS AND PRESENTATIONS

3.1. PUBLICATIONS

1. K. C. Chen, F. H. Elsner and K. S. Mazdiasni, "High T_c Superconductor Powders, Fibers and Film from Organometallic Precursors," 4th U.S.-Japan Workshop on Dielectric and Piezoelectric Materials, October 30 through November 2, 1988. U. S. Department of Commerce, NIST publication, pp. 833-847, December 1988.

3.2. PRESENTATIONS

1. K. C. Chen and K. S. Mazdiasni, "High T_c Superconductor Powders and Fibers from Organometallic Precursor," 91st Annual Meeting of the American Ceramic Society, Indianapolis, Indiana, April 23 through 27, 1989.
2. K. C. Chen and K. S. Mazdiasni, "High T_c Superconductor Fibers from Metallo-organic Precursors," to be presented in the Materials Research Society, 1989 Fall Meeting, Boston, Massachusetts.
3. Sung, S. Pak and K. S. Mazdiasni, "Sol-Gel Synthesis and Characterizations of Submicron High T_c Ceramic Superconducting Powders," to be presented in The 3rd International Conference on Ceramic Powder Processing Science, February 4 through 7, 1990, San Diego, California.

APPENDIX A
METAL ALKOXIDE PRECURSOR COMPOUNDS SYNTHESIS AND PROCESSING

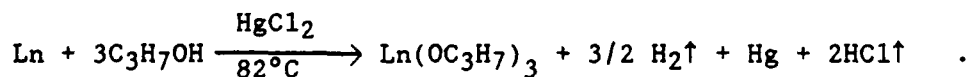
A.1. YTTRIUM AND LANTHANIDE ALKOXIDES

The electronegativity of yttrium and lanthanides places these elements between metals such as aluminum, which forms covalent alkoxides, and sodium, which forms ionic alkoxides. The degree of ionic character of the M-O bond, which is dependent on the size and electronegativity of the metal atom, is important in determining the character of the alkoxide.

The study of alkoxides of yttrium and the lanthanides has been limited due to expensive starting materials and preparation and handling difficulties. Successful characterization of most of the alkoxides is complicated by their extreme sensitivity to moisture, heat, light, and atmospheric conditions.

A.1.1. Synthesis

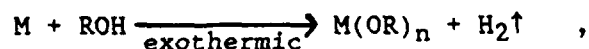
The yttrium and lanthanide tris-isopropoxides are prepared by the reaction of metal turnings with excess isopropyl alcohol and a small amount of HgCl_2 (10^{-4} mol per mol of metal) as a catalyst (Ref. 3).



After filtration, the crude product is purified by recrystallization from hot isopropyl alcohol or vacuum sublimation. Yields of 75% or better are realized with this method. For some of the larger metal ions (lanthanum through neodymium), the reaction rate and percentage yield are increased by using a mixture of HgCl_2 and $\text{Hg}(\text{C}_2\text{H}_3\text{O}_2)_2$ or HgI_2 (Ref. 3) for the catalyst.

Substitution of other R groups for the isopropoxy groups is accomplished by the alcohol exchange technique.

The alkaline earth metal alkoxides are prepared by the reaction of metal with alcohol. The reaction is highly exothermic with evolution of excess hydrogen.

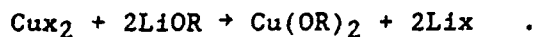


where M = the metal,

R = the isopropyl group,

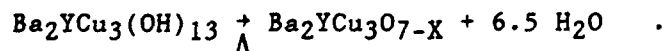
n = 1 or 2.

The copper methoxide and ethoxide are commercially available and are prepared by the reaction of anhydrous copper chloride/fluoride with lithium methoxide, $LiOCH_3$ or lithium ethoxide, $LiOC_2H_5$ in accordance with the following reaction:



A.1.2. HIGH T_c CERAMIC SUPERCONDUCTOR POWDERS

Initially the barium yttrium copper hydroxide, $Ba_2YCu_3(OH)_{13}$ was prepared by hydrolytic decomposition of their respective metal alkoxides. The hydroxide was then concentrated by evaporating the alcohol solvent and dried at $110^\circ C$ for 1 to 2 h. The flow diagram, as applied to preparation of powder, fiber, and film, is shown in Fig. A-1.



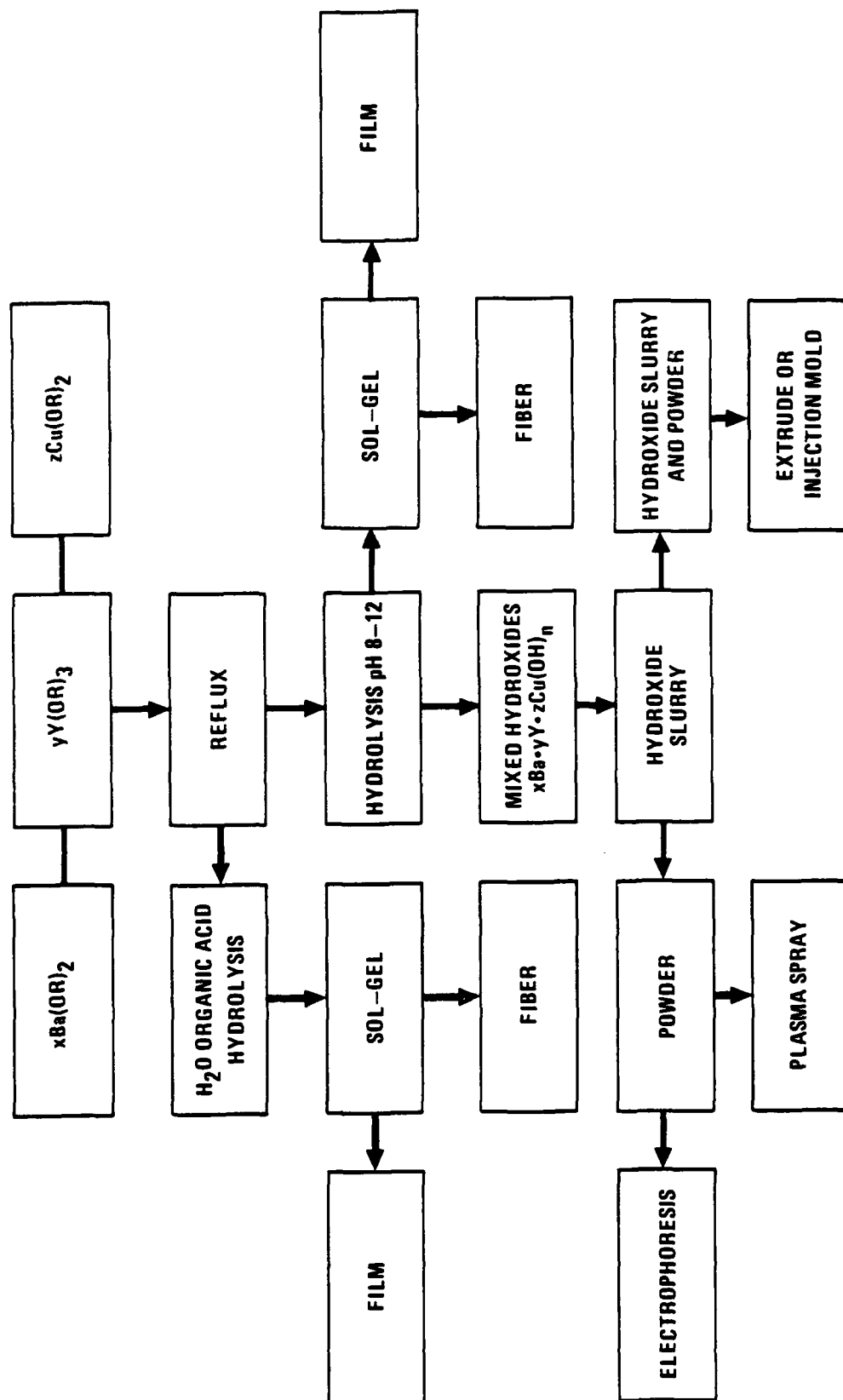


Fig. A-1. Flow diagram for BaYCuO high-temperature superconductor precursor preparation

At this stage, the hydrated hydroxides consist of finely divided particles. The as-prepared powder showed a mixture of various yttrium barium cuprates when examined by X-ray diffraction. Also, the emission spectrographic analyses of the powder after it was calcined at 675°C for 1 h indicated that the powder contained ~300 ppm Si and unacceptable levels of Li and chlorine. The source of Si impurity is from the silicone grease used in the laboratory preparative glass wears and was eliminated in the subsequent powder batches. The elimination of Li and chlorine from the commercially available copper alkoxide containing LiCl was accomplished by repeated washing of the as-received copper methoxide, $\text{Cu}(\text{OCH}_3)_2$, with methanol.

The reduction of the chloride ion by EDX from the copper methoxide is illustrated in Fig. A-2. Although the purification of copper alkoxide was found cumbersome and labor intensive, the result indicates that the Cl content is virtually eliminated from the alkoxide after washing five times with dry methanol. As a further confirmation of the effectiveness of the methanol wash, a chemical analysis (ion chromatography) of the filtrate showed Cl content of 8 ppm and the solid alkoxide had a Cl content that was less than the lowest detectable limit, which is 0.08%.

A.1.3. Powder Synthesis

After the purity of the starting materials was ensured, the next task was to form a homogeneous solution from the three alkoxides. First, Cu methoxide was solubilized in MeOH by complexing with ammonia. The blue solution is then mixed with hydrogen peroxide (containing 31.6% water). By adding the isopropoxides of Y and Ba to this solution, all three alkoxides are kept in solution.

In order to obtain a large number of nucleation sites during hydrolysis, thus allowing the formation of fine precipitates, the homogeneous solution obtained was mixed quickly with an excess amount of

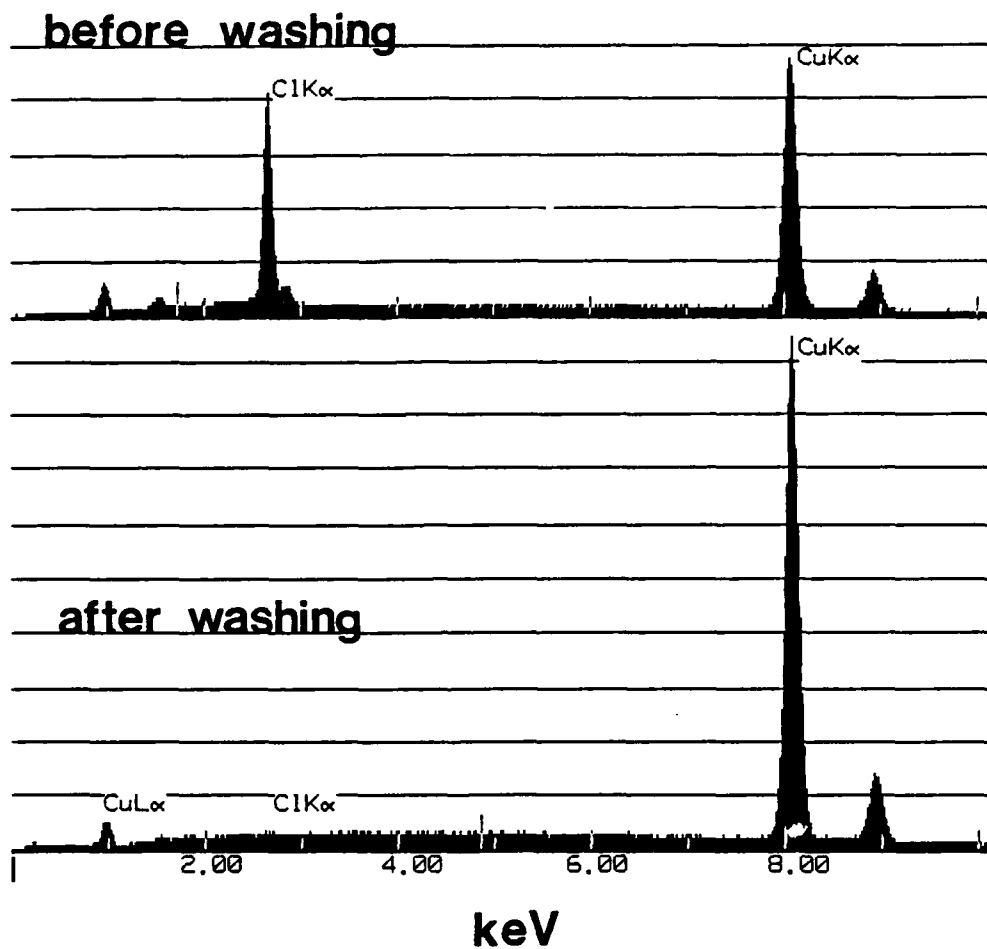


Fig. A-2. EDX analysis of Cu methoxide powder before and after washing

hydrogen peroxide and water. Gelatinous precipitates formed immediately. The sol and/or gel was then concentrated to dryness at 40°C in a rotary evaporator. Due to the moisture sensitivity and reactivity of high T_c superconductor material with CO_2 , excessive exposure of the powder material to an ambient atmosphere was avoided by gentle crushing of the dried powder in the dry box and storing the powder under inert atmosphere.

The X-ray diffraction pattern of the as-prepared powder and isothermally aged for 1 h in oxygen at 750°, 800°, and 900°C are shown in Fig. A-3. The primary result based on X-ray diffraction data indicates that the phase transformation in 123 system is a bulk phenomenon and is not a function of nucleation and growth of primary crystalite to larger crystalite size.

Figure A-4 shows a TEM image of the as-prepared powder. The particles are mostly amorphous and their size ranges are between 20 and 50 nm in diameter. The fine particles, however, do not maintain their size upon calcination. They tend to agglomerate severely and sinter even as low a temperature as 400°C. An example of such an aggregate is given in Fig. A-5. It is clearly evident from this experiment that calcination temperature must be maintained as low as possible if particle size is to be kept small and the degree of agglomeration is to be minimized.

Since it is advantageous to keep the powder particle size small for higher activity, the calcination temperature must be lowered. Recently, it has been reported that the 123 formation temperature was lowered to 650° to 700°C when the hyponitrate derived 123 was heat treated in argon (Ref. 4). Similar heat treatment was adopted in this study. The powders were calcined initially in oxygen at 400°C for an hour and then in argon. A summary of the experiment is presented in Fig. A-6. The XRD patterns clearly show that tetragonal 123 was formed at as low a temperature as 750°C in just one hour, which is 150°C lower than when the powder was calcined in oxygen atmosphere.

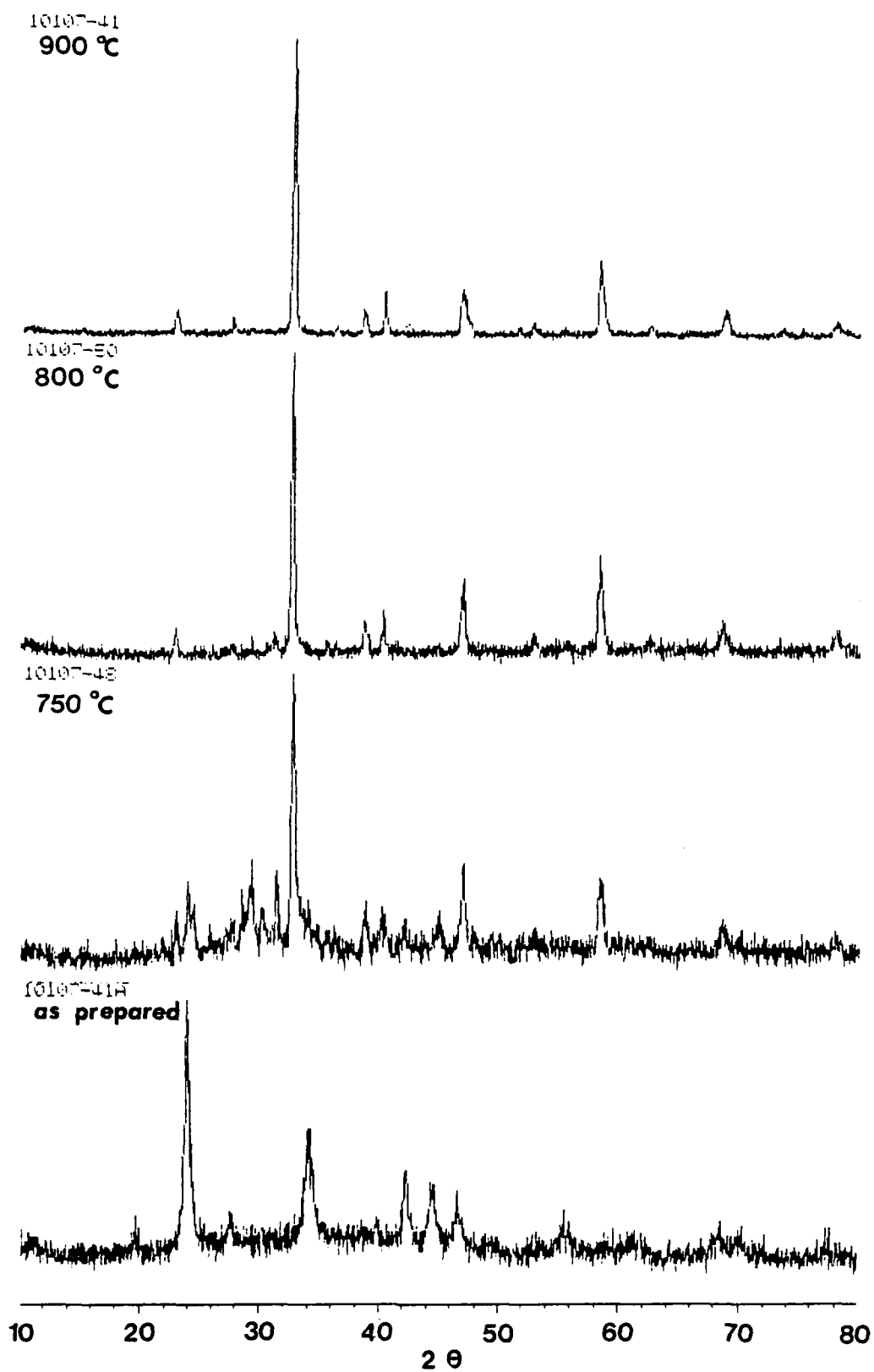


Fig. A-3. XRD patterns of 123 powder fired in oxygen for 1 h



Fig. A-4. TEM image of as-prepared powder



200 nm

Fig. A-5. TEM image of 123 powder heated at 400°C for 1 h in flowing oxygen

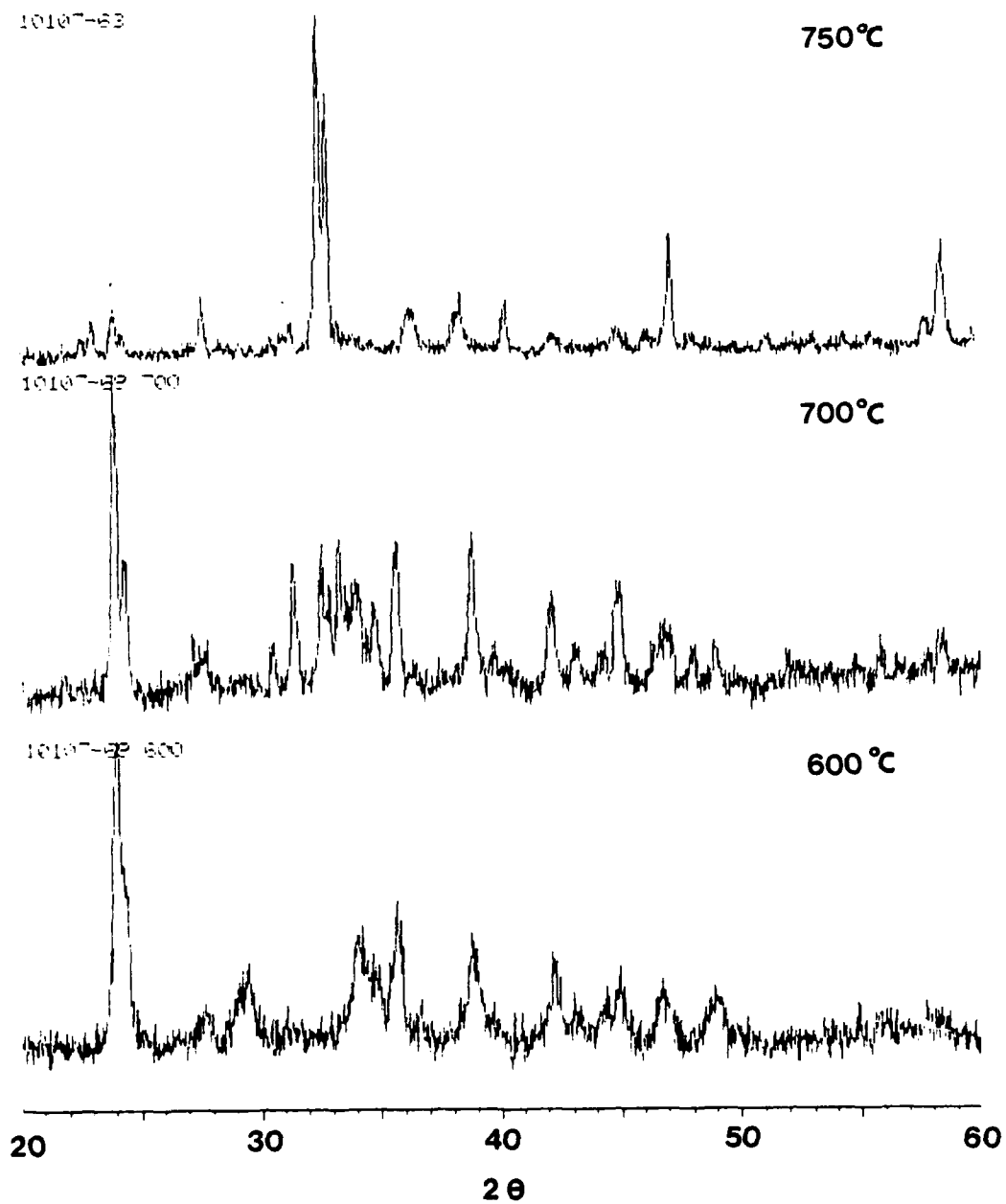


Fig. A-6. XRD patterns of 123 powder heated in flowing argon

To observe the effect of atmosphere and calcination temperatures on 123 powder particle size and particle morphology, powder samples were heat treated at 750°C for 1 h in air and viewed by TEM. Figure A-7 shows that the particle size is still in submicron range and less agglomerated.

A.1.4. Seed-Powder Synthesis

A new and innovative approach to preparation of fine crystals of $\text{DyBa}_2\text{Cu}_3\text{O}_{7-x}$ was developed by pyrolysis of paper filament coated with metallo-organic solution containing the 123 constituent. The objective was to produce highly crystalline submicron 123 particulates for seeding purposes. The experimental results indicate that in the aforementioned process, agglomeration, nucleation, and growth of the powder formed at 850° to 950°C were avoided. While the crystallinity is improved, the well-developed crystal facets are achieved by prolonged firing.

A typical $\text{DyBa}_2\text{Cu}_3\text{O}_{7-x}$ powder sample after firing at different temperatures and times are shown in Figs. A-8(a) and A-8(b). In some areas where solution is trapped by the capillary force, the grain growth is more prominent [Figs. A-9(a) and A-9(b)]. This implies that a paper filament coated with a very dilute solution is a potential source for 123 fine crystals as seed material. Detailed study is being performed to determine the best procedure for production of single-phase submicron $\text{DyBa}_2\text{Cu}_3\text{O}_{7-x}$ powders. The preliminary results indicate the crystallization is similar to that of $\text{YBa}_2\text{Cu}_3\text{O}_{7-x}$.

A.1.5. Sol-Gel Processing

By controlling the concentrations of solvent and the constituent materials, a sol can be cast into a mold and concentrated into a gel. It is hoped that this gel can then be dried into a fully dense 123 superconducting monolith.

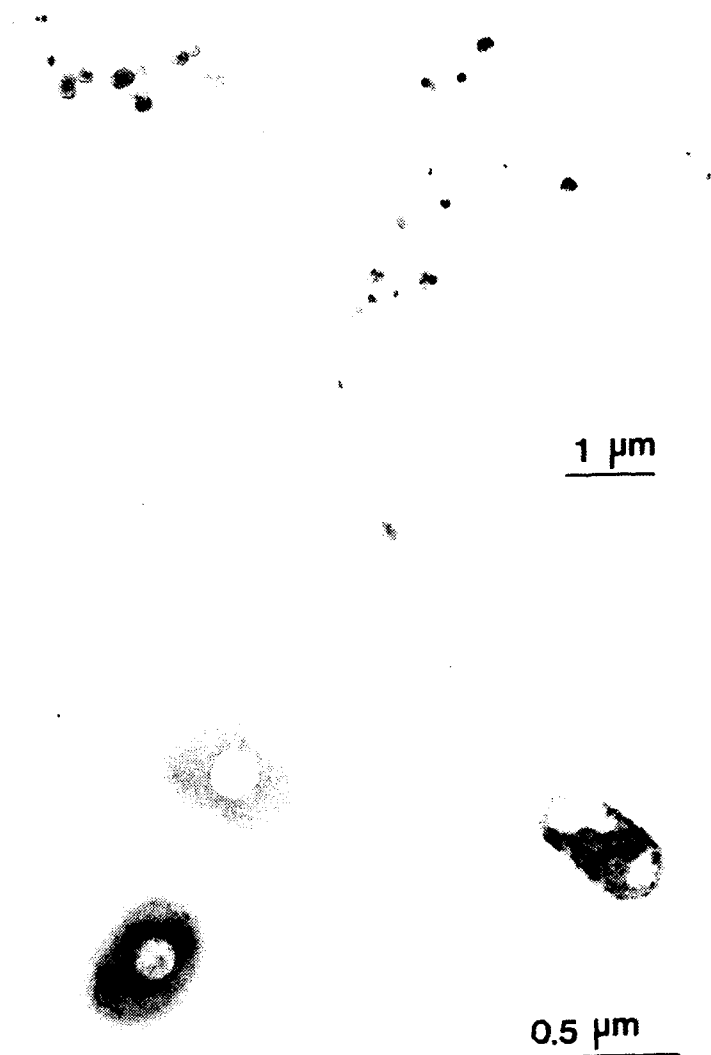
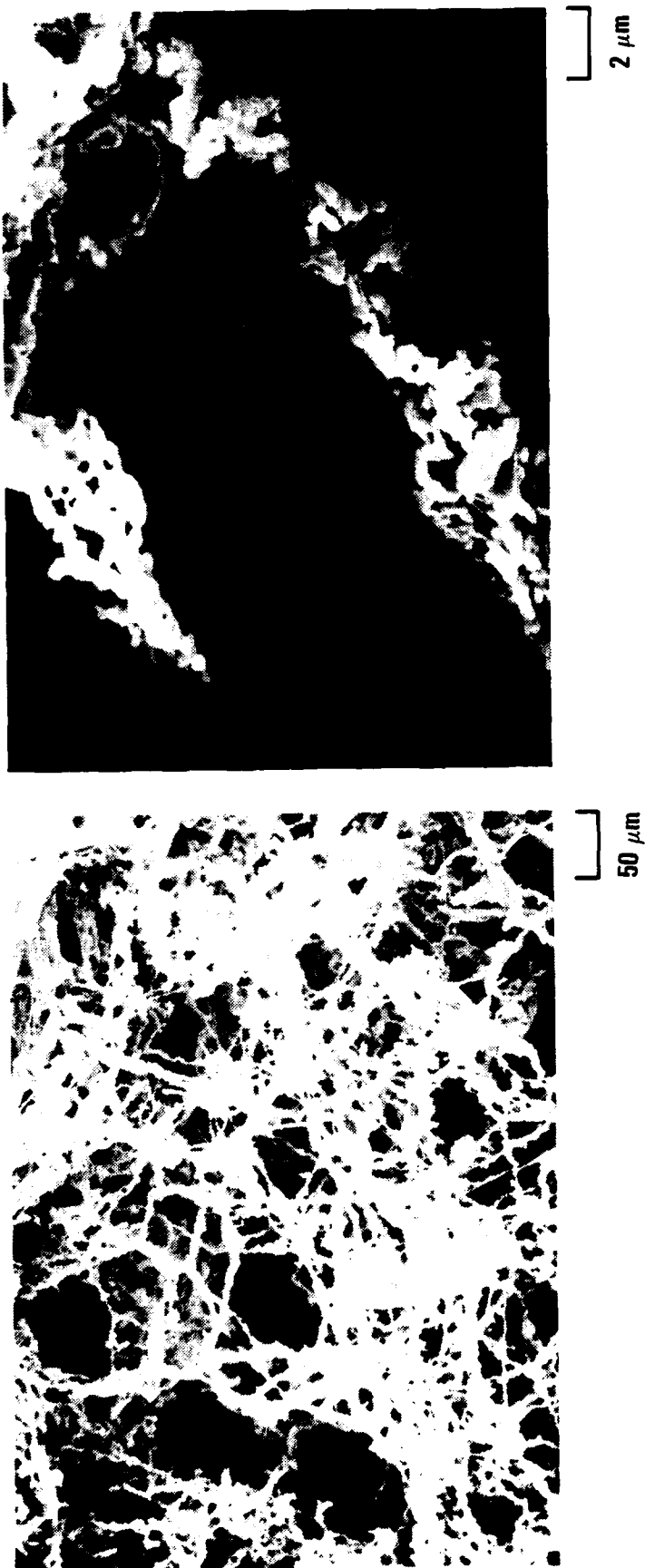


Fig. A-7. TEM image of 123 powder heated at 750°C for 1 h in flowing air

**SUB-MICRON SOFT-AGGLOMERATE
DyBa₂Cu₃O_{7-x} POWDER AT 900°C 4 HR**



J-047(1)
4-14-89

Fig. A-8. (a) DyBa₂Cu₃O_{7-x} powder prepared by the pyrolysis of solution coated on paper filaments and (b) a higher magnification shows the crystals are loosely agglomerated even after 900°C, 4-h heat treatment

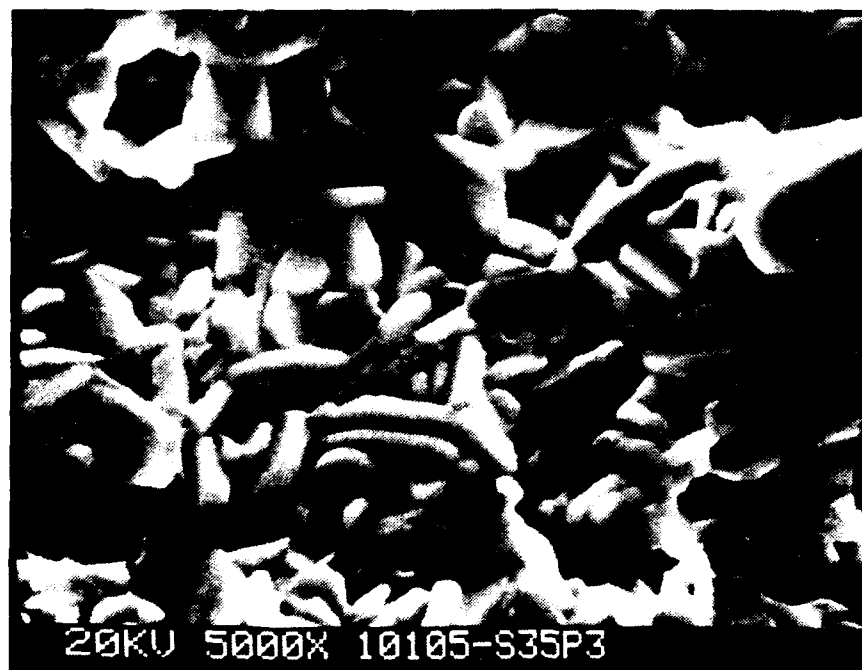
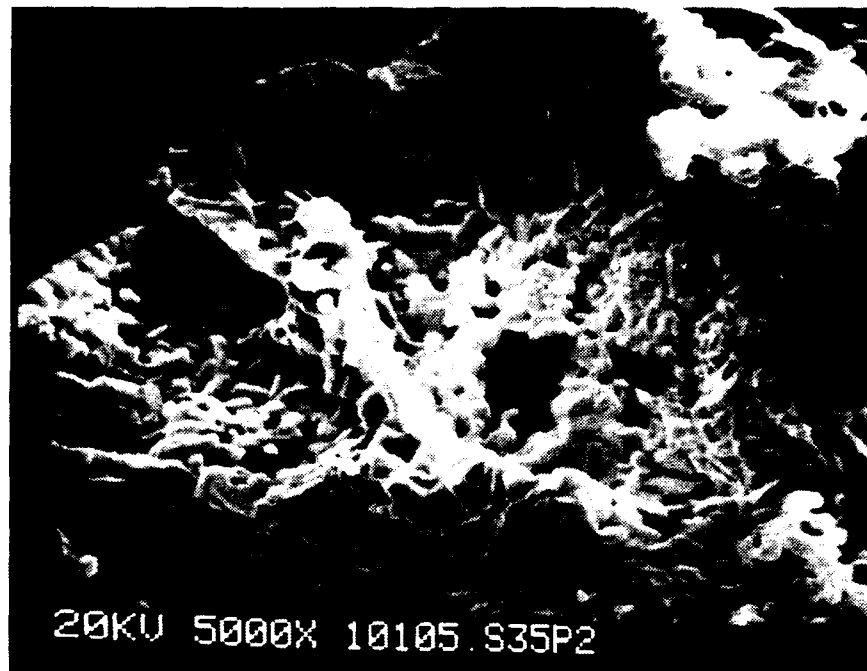


Fig. A-9. $\text{DyBa}_2\text{Cu}_3\text{O}_{7-x}$ powder calcined at (a) 900°C, 4 h and (b) 900°C, 8 h

The method used to make the sol is similar to that used in making films and powders; however, for this application, the amount of solvent used is critical to later drying of the gel. Using an excessive amount of solvent in preparing the gel means that there is more liquid to be removed upon drying. Conversely, not enough solvent prevents the formation of an initial homogeneous 123 solution. By an iterative process, a weight ratio of 62:1 dry methanol to solid copper methoxide was determined to be appropriate for producing a gel.

Controlled, uniform drying of 123 monolithic gels, as with any other gel, is very critical. The gels need to be dried slowly enough to prevent cracking. Initially, the gels were dried through surface contact with air. The top of the sample vial was left off to allow the gel to dry. This resulted in the surface drying more rapidly than the rest of the gel and inevitably led to cracking of the gel. The air drafts, variations in temperature, and humidity within the laboratory also made this method unacceptable for drying gels.

In an effort to obtain more uniform drying conditions, the gels were partially submerged in both water and oil baths. The bath temperatures were maintained between 40° and 50°C to promote slow drying. The purpose of using the baths was to initiate drying below the surface as well as at the surface. The water bath treatment was quickly abandoned, since the presence of water vapor was found detrimental to the superconducting properties of the gel. However, by controlling the time and temperature of drying, the tendency of the gel to crack was minimized.

After drying, the gels were reacted and sintered at various temperatures to obtain a clean, impurity-free 123 composition. Preliminary X-ray diffraction studies were performed to obtain the optimum reaction temperature for the yttrium barium copper oxide gel conversion to superconducting 123. Dried gels were ground to powder and reacted from 750° to 900°C, as shown in Fig. A-10. From this figure, it is obvious that the 900°C reaction temperature yields a clean 123 powder; therefore,

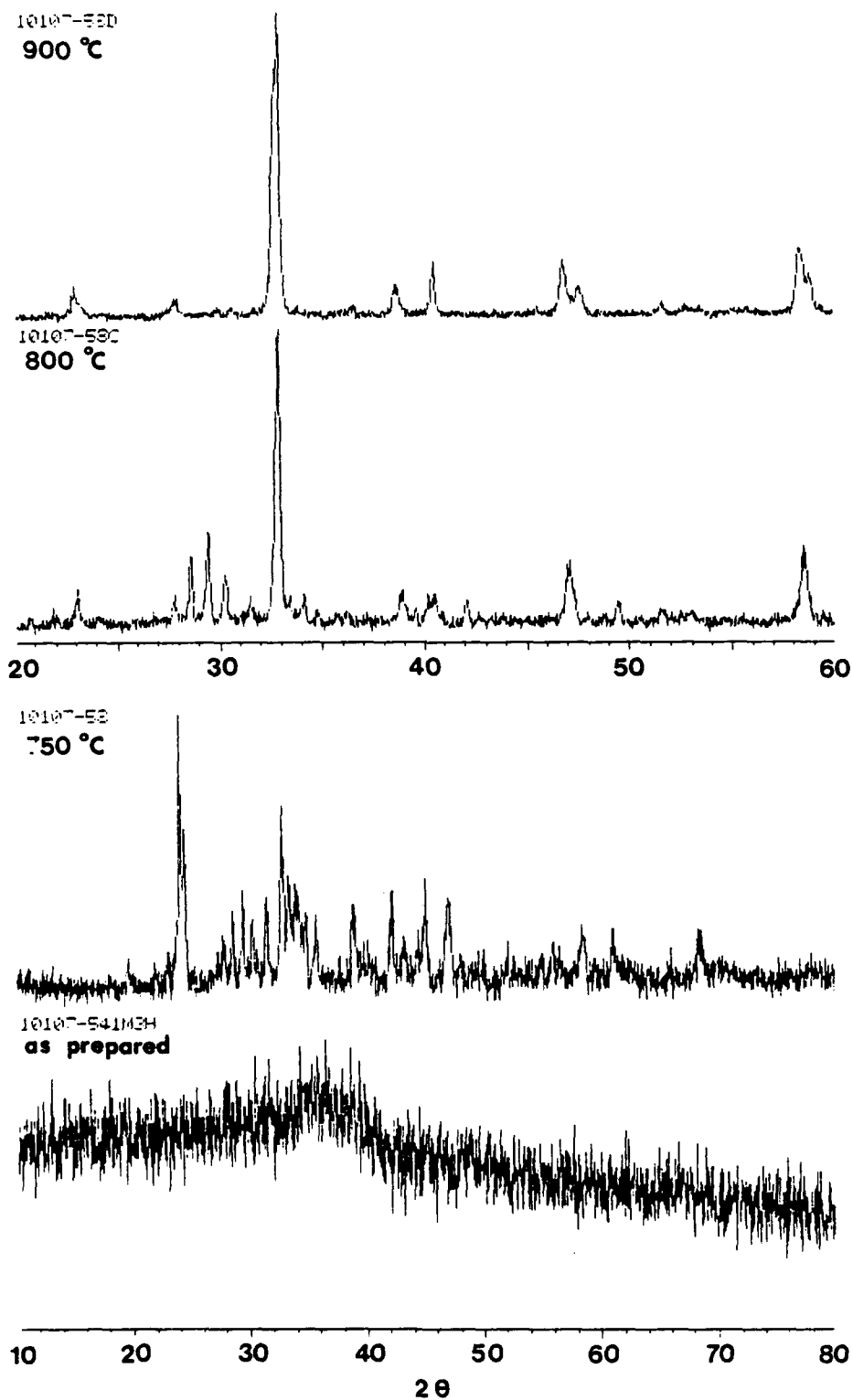


Fig. A-10. XRD patterns of 123 gel-powder fired in oxygen for 1 hour

subsequent gels were reacted at 900°C with oxygen anneals performed at 350°C.

Once the reaction temperature was determined, it was necessary to begin densifying the gels. A partially densified piece of gel is shown in Fig. A-11. This gel was heated to 900°C over 4 h and held at 900°C for 30 min. Upon cooling, it was subjected to an oxygen anneal at 350°C for 1 h. Although deviation from stoichiometry exists in this sample, initial progress in densification is illustrated. The lower magnification micrograph shows that the gel is fine grained and relatively dense; however, at higher magnification, pockets of porosity are evident. The work is continued in this area in drying and reacting the gels to obtain dense 123 monoliths.

A.1.6. Thin Films

In this work, the same precursor chemicals as the ones used for the powder and gel synthesis study were employed. By controlling the amount of solvent and hydrogen peroxide and water, a solution with appropriate viscosity was prepared. By dipping a polished yttria stabilized zirconia substrate repeatedly, with approximately 60 sec. of drying in air between each dip, and heating to 800°C, a 123 film, much like the one presented in Fig. A-12, was formed.

Although the film is not crack free, it shows that, for the most part, the film has a smooth surface finish. The accompanying XRD pattern shows that all the peaks other than those from the substrate are due to the presence of 123.

A.1.7. Synthesis of Precursor Compounds Suited for Film and Fibers Processing

As mentioned before, in order to obtain precursors with the proper chemical stoichiometry to give the 123 compound, it is advantageous to use homogeneous liquid solutions of the metallic components. Synthesis

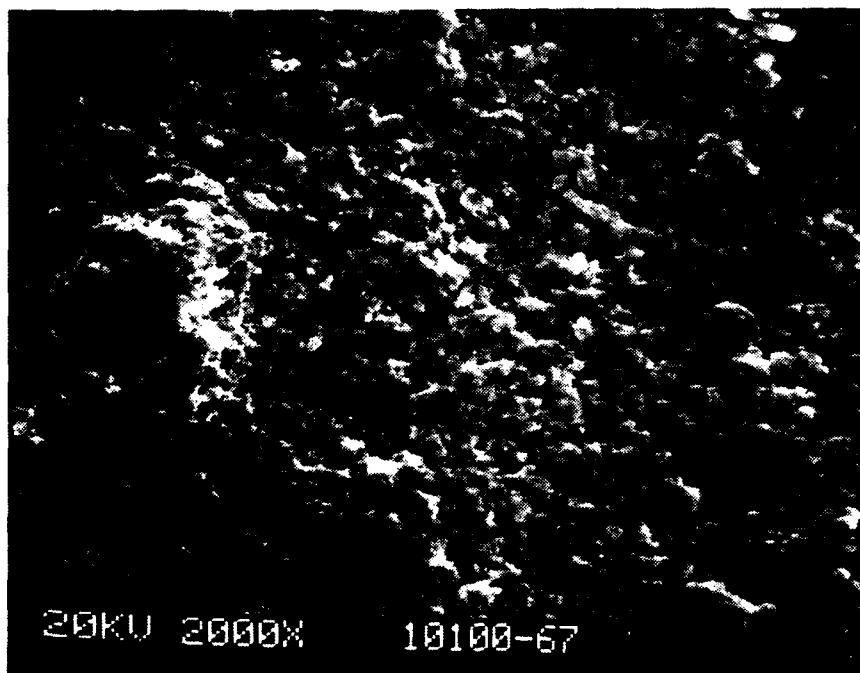
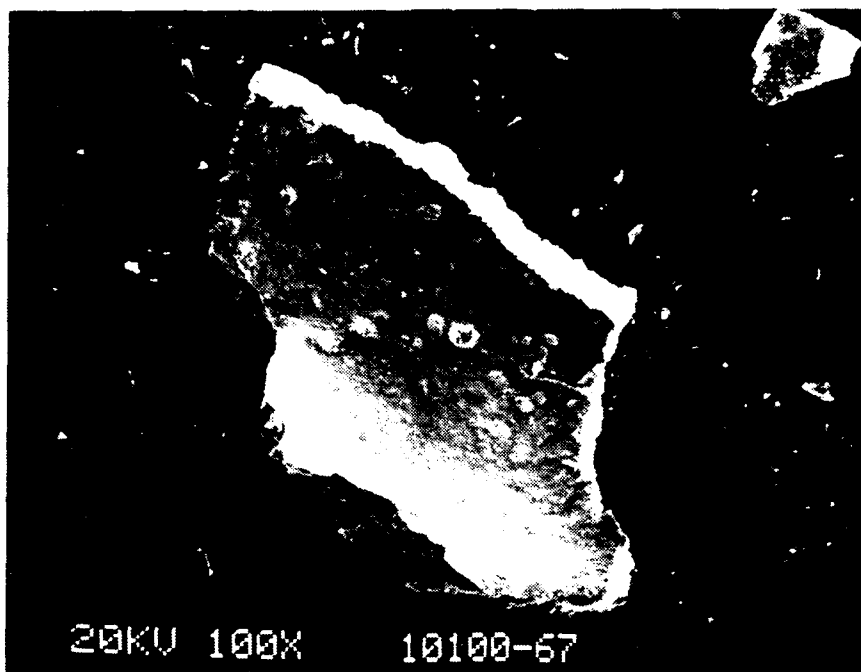


Fig. A-11. Scanning electron micrograph of 123 superconductor gel monolith sintered at 900°C

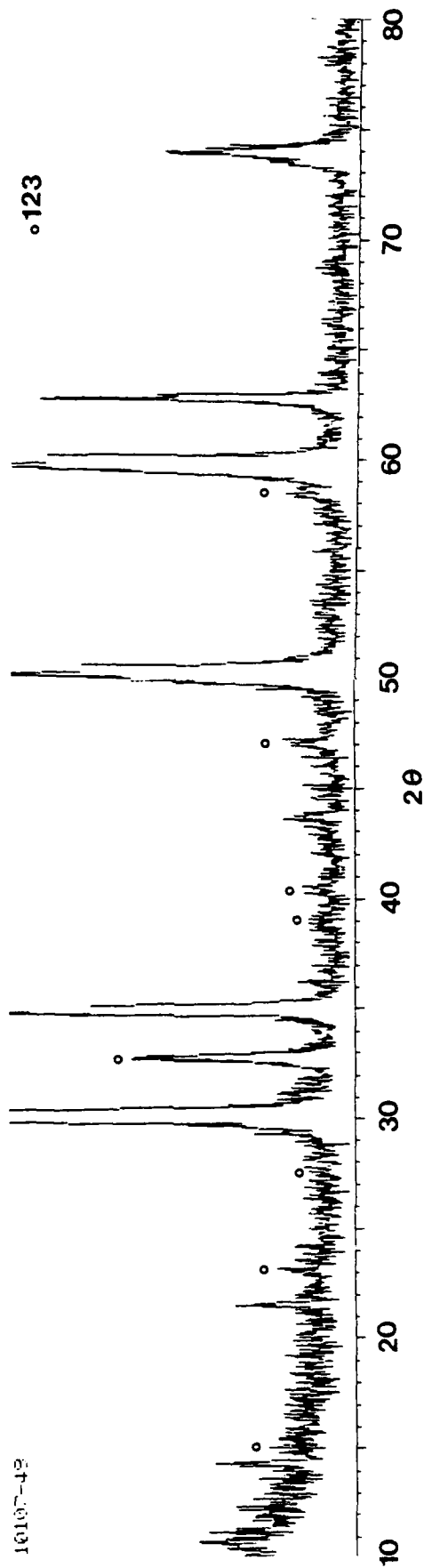
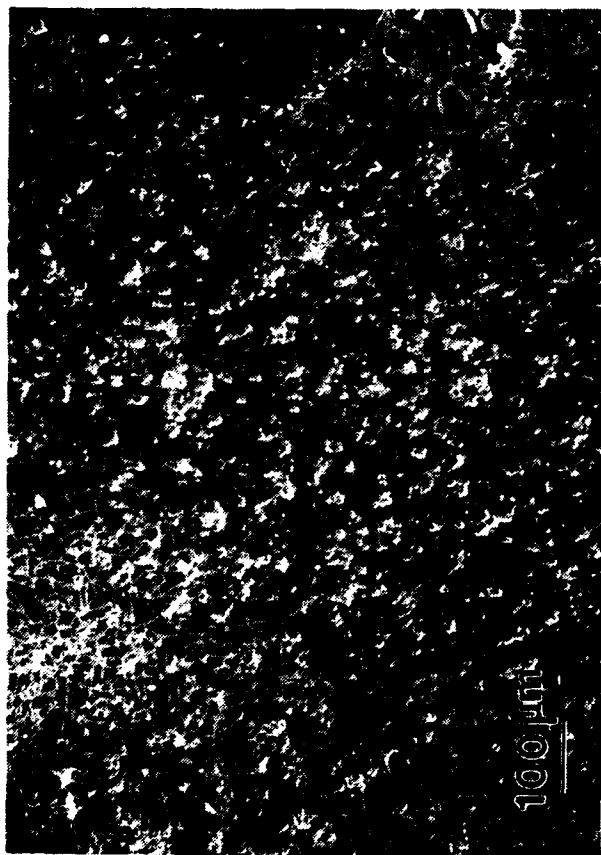


Fig. A-12. SEM images and XRD pattern of a thin film coated on a YSZ substrate

using the required ions and an organic acid (Ref. 5), the hyponitrites (Ref. 6), yttrium and barium alkoxides with different coordination compounds of copper (Refs. 7 through 9) have been reported.

A difficulty with the reported synthetic procedure has been precipitation of a solid containing copper when the soluble Cu(II) species is added to the yttrium alkoxide. Fahrenholtz et al. (Ref. 10) suggests that this is due to an exchange of the acetylacetonate ligand on the Cu(II) species with the yttrium alkoxide. Rather than to adjust the initial solution concentration by adding additional Cu(II) compound, we have been investigating the use of peroxides as stabilizing agents for the initial homogeneous solution.

In order to determine which one of the syntheses will yield superconducting films and fibers capable of carrying high currents at critical temperatures approaching 90 K, we were successful in preparing the 123 compound by combining certain aspects from syntheses reported by Payne (Ref. 10) and McCartney (Ref. 11).

Typically, homogeneous solutions containing the 123 compounds were prepared by reacting 0.033 g (0.00024 mole) of barium granules (Alfa Products) with 0.225 ml of the stock yttrium alkoxide (0.00012 mole) and 0.275 ml dry 2-ethoxyethanol. The barium reacted completely in about 2 h at room temperature. To this solution was added 0.0914 g (0.00036 mole Cu) of the Cu(II) compound, which dissolved readily. After stirring at room temperature for 20 min, 1 to 10 equivalents of water per mole of alkoxy ligand were added. After a 1- to 4-h reaction time, the solvent was removed under vacuum at 56°C, giving a black powder.

Figure A-13(a) shows the TGA decomposition behavior of a precursor powder when heated in oxygen at 1°C/min. Three regions of rapid weight loss are observed: 150° to 200°C, 550° to 600°C, and 775° to 825°C. The total weight loss for this sample approaches 50 wt %. The 25% loss at temperatures less than 200°C is thought to be bound solvent and

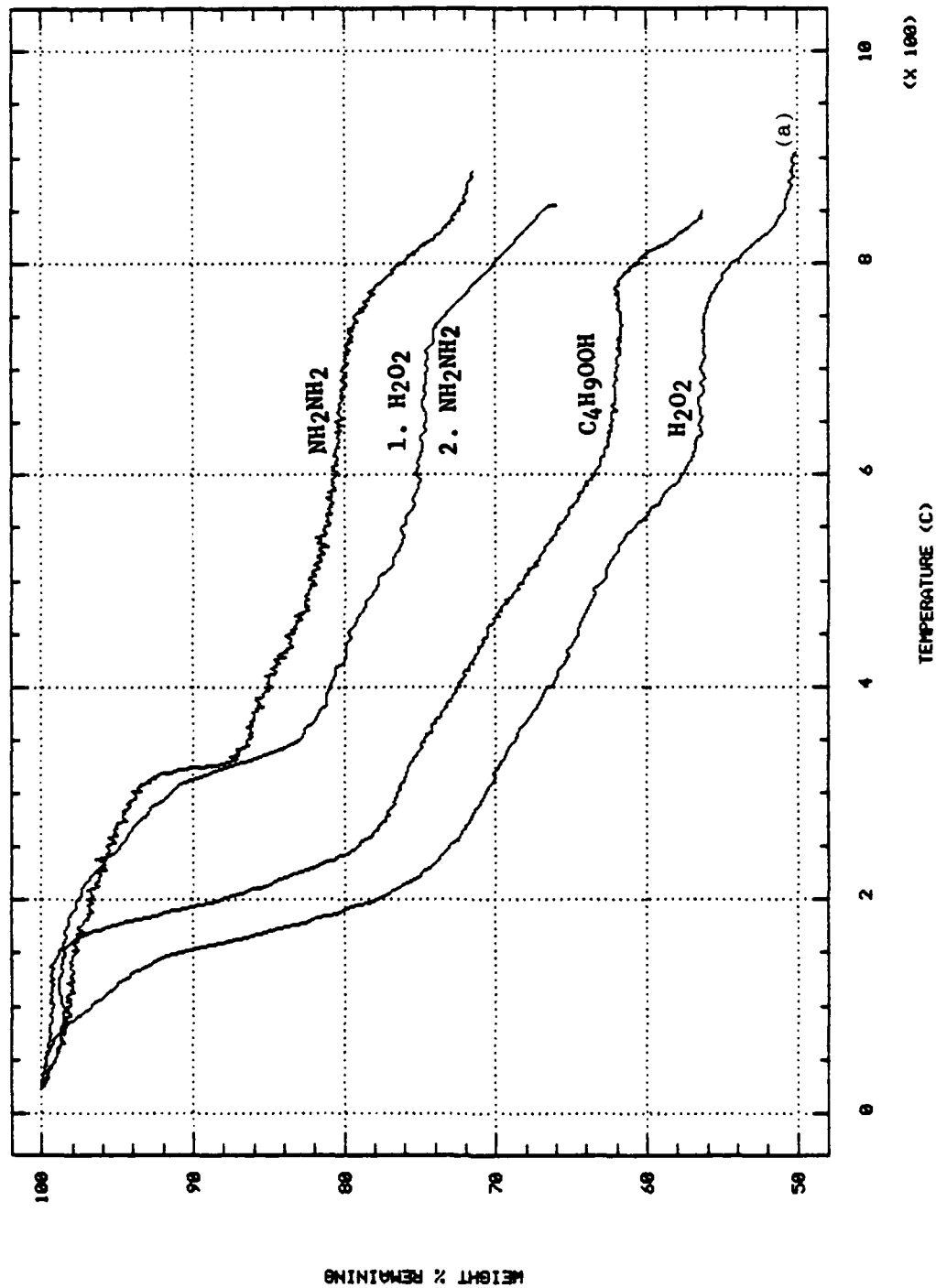


Fig. A-13. Comparison of thermal decomposition of 123 precursor powders produced with additives during the hydrolysis step

water, since a sample dried in a vacuum oven at 135°C lost only about 5 wt % up to 200°C. Furthermore, the latter sample lost only a total of 28 wt %. We are currently attempting to use gas chromatography to determine what species are evolved during the several regions of weight loss.

Based on Fig. A-13(a), a sample of 123 powder was prepared by calcining in oxygen according to the following schedule:

1. Heat at 60°C/h to 900°C.
2. Hold 5 h at 900°C.
3. Cool at 300°C/h to 500°C.
4. Hold 5 h at 500°C.
5. Cool to room temperature.

Figure A-14 shows the X-ray diffraction pattern for material prepared as described above using 3.6 equivalents of water per mole of alkoxide ligand. The diffraction data indicates that the 123 compound is clean, with undetectable amounts of barium carbonate, copper oxide, or barium cuprate, which have been found as contaminants in other syntheses.

In subsequent runs, combinations of water and other oxidizing agents were attempted. Table A-1 describes the reaction conditions used during hydrolysis of the alkoxides. Since the minimum amount of water necessary for hydrolysis is 0.5 mole per mole of alkoxide moiety, water was used in excess. Hydrogen peroxide and t-butyl hydroperoxide were added to keep the copper in the Cu(II) oxidation state. Also, hydrazine was used in an attempt to reduce the copper acetylacetonate, with the hope that decomposition to the 123 compound would occur at low temperature.

The stability of the solutions was estimated by observing the necessary time for mixing needed to observe a precipitate when a strong light beam was passed through the solution. Solutions without any

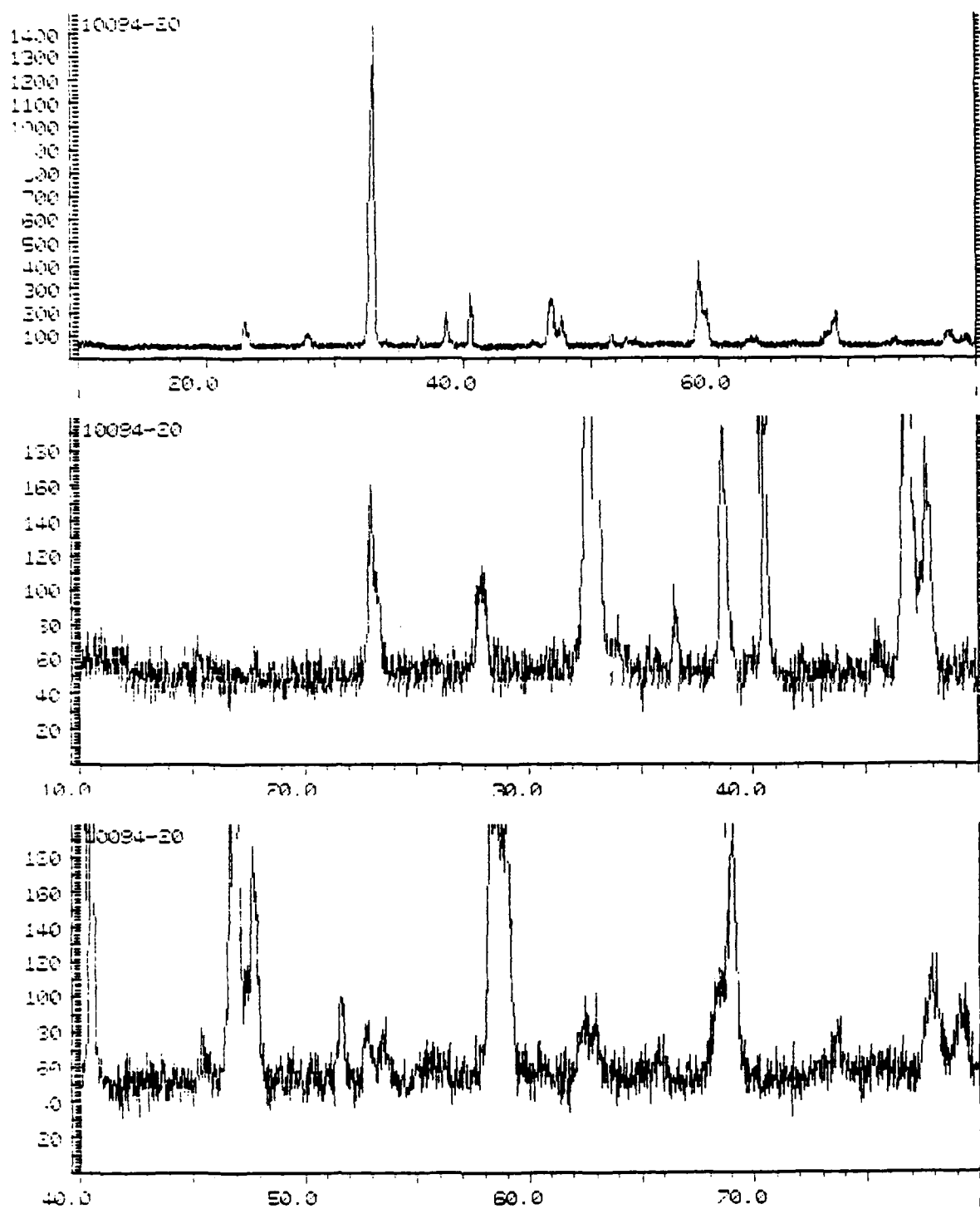


Fig. A-14. X-ray diffraction pattern for powder obtained by hydrolysis of 123, Y:Ba:Cu solutions with 3.6 equivalents of water per mole alkoxide

TABLE A-1
MOLAR RATIO OF ADDITIVES USED DURING HYDROLYSIS
AND POLYCONDENSATION OF ALKOXIDES

Test	Expected Y:Ba:Cu	Additive Mole/Mole Alkoxide Moiety				
		H ₂ O	H ₂ O ₂	C ₄ H ₉ OOH	NH ₂ NH ₂	H ⁺
10094-4	1:2:3	1.7			1.1	
10094-11	1:2:3	4.5	0.17			
10094-15	1:2:3	3.0			1.7	
10094-31	1:2:3	6.5	0.11		2.1	
10094-51	1:2:3	3.6		0.43		
10094-89	1:2:3	4.5	0.16			
10094-70	1:2:0	4.2	0.15			
10094-82	0:0:1	4.5	0.17			
10096-9	1:2:3	3.9				0.07
10096-13	1:2:3	3.9				1.0
10096-16	1:2:3	3.9				0.07

additives generally showed a precipitate within 20 to 30 min from the addition of Cu(II) to the solution containing the Y and Ba alkoxide. When oxidizing agents are added to the solution, no precipitates are observed for 2 to 4 h after the addition (Table A-2). Hydrazine, however, results in an immediate darkening of the solution and formation of a black precipitate. The use of hydrogen peroxide usually results in a product that, after calcining to 850, exhibits the diffraction pattern of only orthorhombic 123 (Table A-2). When hydrazine is used, orthorhombic 123 is the major product, but the diffraction pattern of an impurity is also observed with a d-spacing of 2.7 to 3.2°A. It is difficult to identify this impurity, but it may be a combination of the 211 and the 011 compounds.

In an attempt to understand the decomposition and conversion of the initial powder to the 123 compound, the weight loss of the samples as a function of the decomposition temperature (TGA, were measured. A comparison of the TGA for different hydrolysis additives is shown in Fig. A-13. Typically, there are two areas of rapid weight loss. The high temperature region occurs between 750° and 850°C and does not depend on the additive used during hydrolysis. The low temperature region, however, occurs between 300° and 350°C for samples treated with hydrazine and between 150° and 250°C for processes using oxidizing additives.

The weight losses are significantly smaller for processes in which hydrazine has been added. This suggests that the hydrazine reacts with Cu(II) compound liberating a high volatility material that is removed during the drying step, before the TGA run is conducted.

Since low temperature processing is desirable, one test (Fig. A-15) was conducted in which a hydrogen peroxide processed sample was heated to 350°C and held isothermally for about 2000 min. The temperature was then increased to 850°C. The weight loss 350°C reached a plateau that

TABLE A-2
STABILITY AND PRODUCTS OF HYDROLYZING SOLUTIONS
OF 123 ALKOXIDES WITH ADDITIVES

Test	Solution Stability (h)	Measured ^(a) Y:Ba:Cu	Products ^(b)
10094-4	0		123 (211,011)
10094-11	4		123
10094-15	0	1:2.4:4.0	123 (211,011)
10094-31	4	1:2.0:3.8	123 (211,011)
10094-51	2	1:1.5:2.3	123 (211,011)
10094-89	2	1:2.1:3.8	123 (211,011)
10094-70	0		BaCO ₃ (Y ₂ O ₃)
10094-82	0	0:0:1	CuO
10096-9	3	1:2.1:3.7	123
10096-13	0		123 (211,011)
10096-16	3		

(a) Measured by EDAX.

(b) Measured by X-ray diffraction.

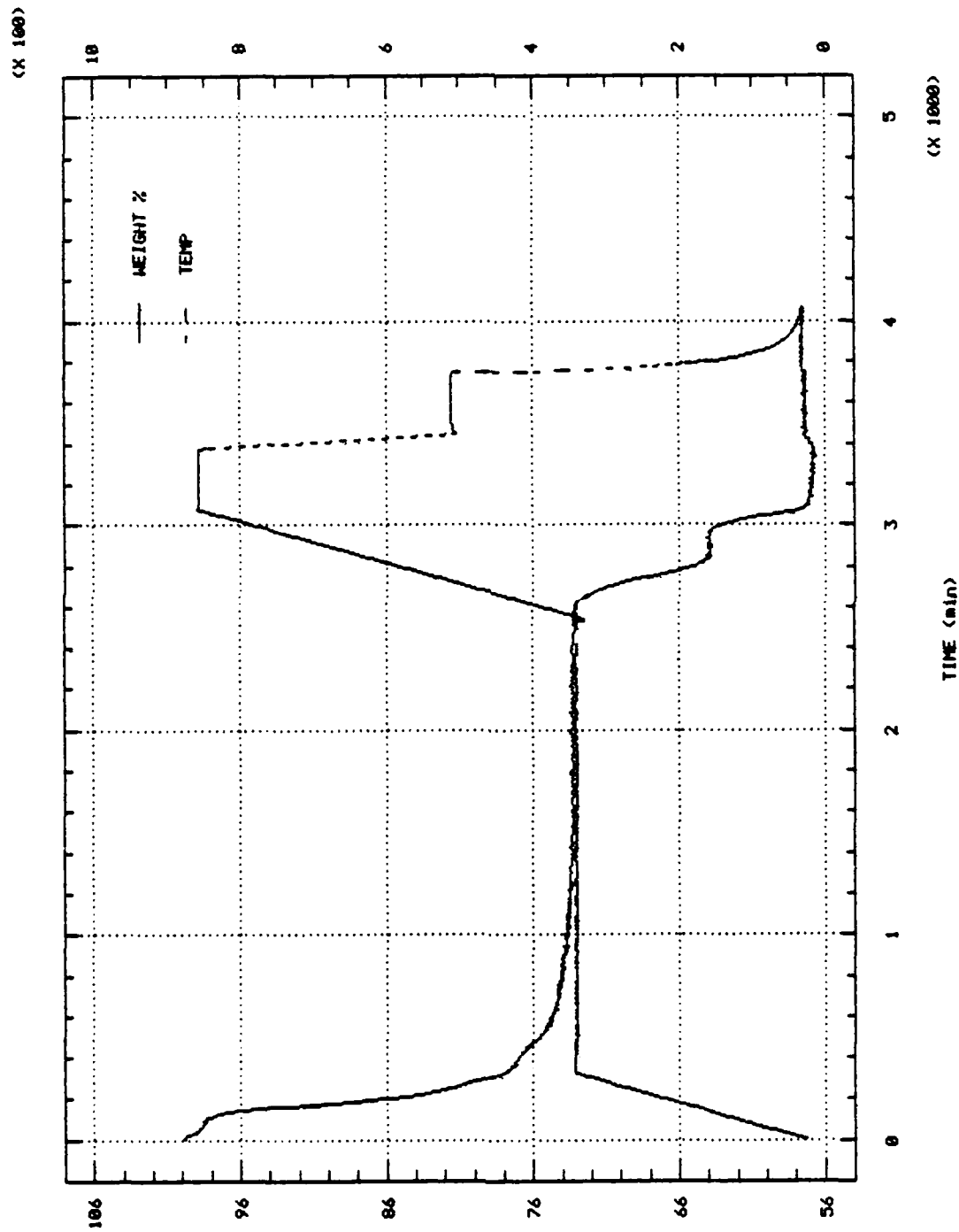


Fig. A-15. Weight loss during ramp and hold test of 123 precursor powder prepared using H_2O_2 additive

was similar to the weight loss during a continuous increasing temperature ramp. Further, on increasing the temperature, additional weight loss occurred. Currently, experiments are underway to determine the product composition in the different temperature regions.

A.2. SOL-GEL COATING

A.2.1. Dip Coating

Another important objective of this work is to produce superconducting thin films. Accordingly, appropriate experiments were initiated to develop thin films.

GA has constructed a microprocessor based dip coating machine for coating small disks or strips. This instrument consists of a sample holder device attached to a Berg linear clutch assembly. The holder is contained in an pyrex glass enclosure, which also surrounds the vial with the coating solution. Inert or reactive gas can be purged through the enclosure during the dipping process. Surrounding both ends of the enclosure are heaters, operated by separate Omega temperature controllers, that function as a coating dryer and a coating solution heater. The linear clutch is driven at a variable speed of 1-5 mm/s by a Minarek reversible dc motor. The direction of travel of the linear assembly, the position of the assembly, and the number of dips is controlled by an LFE microprocessor based controller. The ramp-and-soak feature of the LFE allows the operator to change the length of time that the sample is held in the coating solution or in the heater zone.

Figure A-16 is a photomicrograph of a coating prepared by dipping YSZP substrate 300 times into an alkoxide solution that had been hydrolyzed with a low concentration of H_2O_2 and water. In between dips, the solvent was evaporated at 90° to 95°C in the drying portion of the dip coater. After coating, the sample was dried in a vacuum at 94°C to remove residual solvent. Some small cracks can be observed, but the

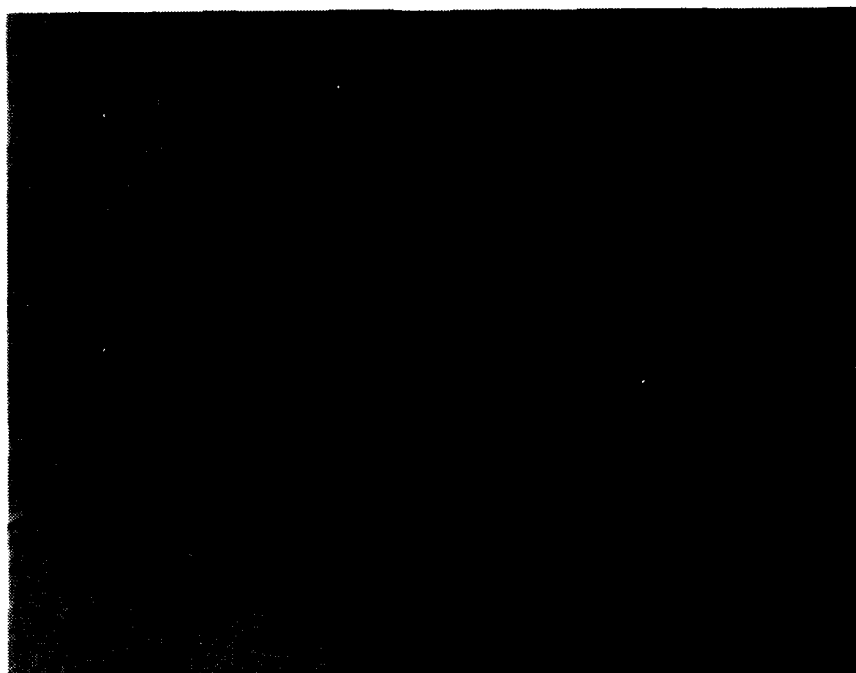


Fig. A-16. Photomicrograph of yttria stabilized zirconia substrate dip-coated 300 times with a solution hydrolyzed using water and hydrogen peroxide

coating is considerably more continuous than those obtained earlier by hand dipping.

Figure A-17 is a 400 magnification of a coating prepared by 40 dips into a solution that did not contain hydrogen peroxide. This coating is striated and seems to have cracks perpendicular to the withdrawal direction.

Work is continuing to study the effects of chemistry and solution rheology on the properties of these coatings.

A.2.2. Sol-Gel Derived Fiber

A.2.2.1. Fiber Processing. To form a useful ceramic fiber from sol-gel, all the parameters shown in Fig. A-18 must be understood and reproducibly controlled. In order to acquire suitable properties (namely, adequate solution stability, high solubility in organic solvents, spinnability, and thermosetting properties) in the polymeric material for fiber drawing, the structure of the solutions should first be controlled.

It is known that if each monomer contains more than three functional groups, a three-dimensional rigid network will form upon complete polymerization. Therefore, the number of active functional groups per molecule should be limited to two (or close to two) for the polymer to have some degree of flexibility. The two-dimensional chain-type structure should provide spinnability for fiber drawing and, at same time, have a better chance to be dissolved in organic solvents. To achieve this requirement in alkoxides, the alkoxy group could be replaced by organic acids or beta-diketones. Since the molecular structures of the alkoxides used are not well defined at the present time, the exact amount of organic acids needed to achieve chain-type structure should be determined experimentally.

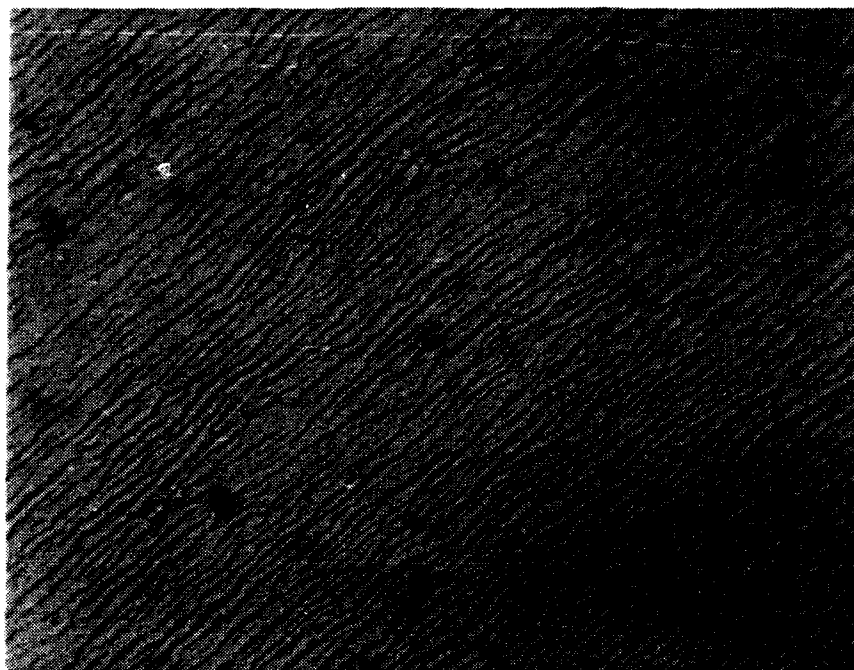


Fig. A-17. Photomicrograph of a coating prepared by dip coating yttria stabilized zirconia substrate 40 times with a solution hydrolyzed using water without hydrogen peroxide

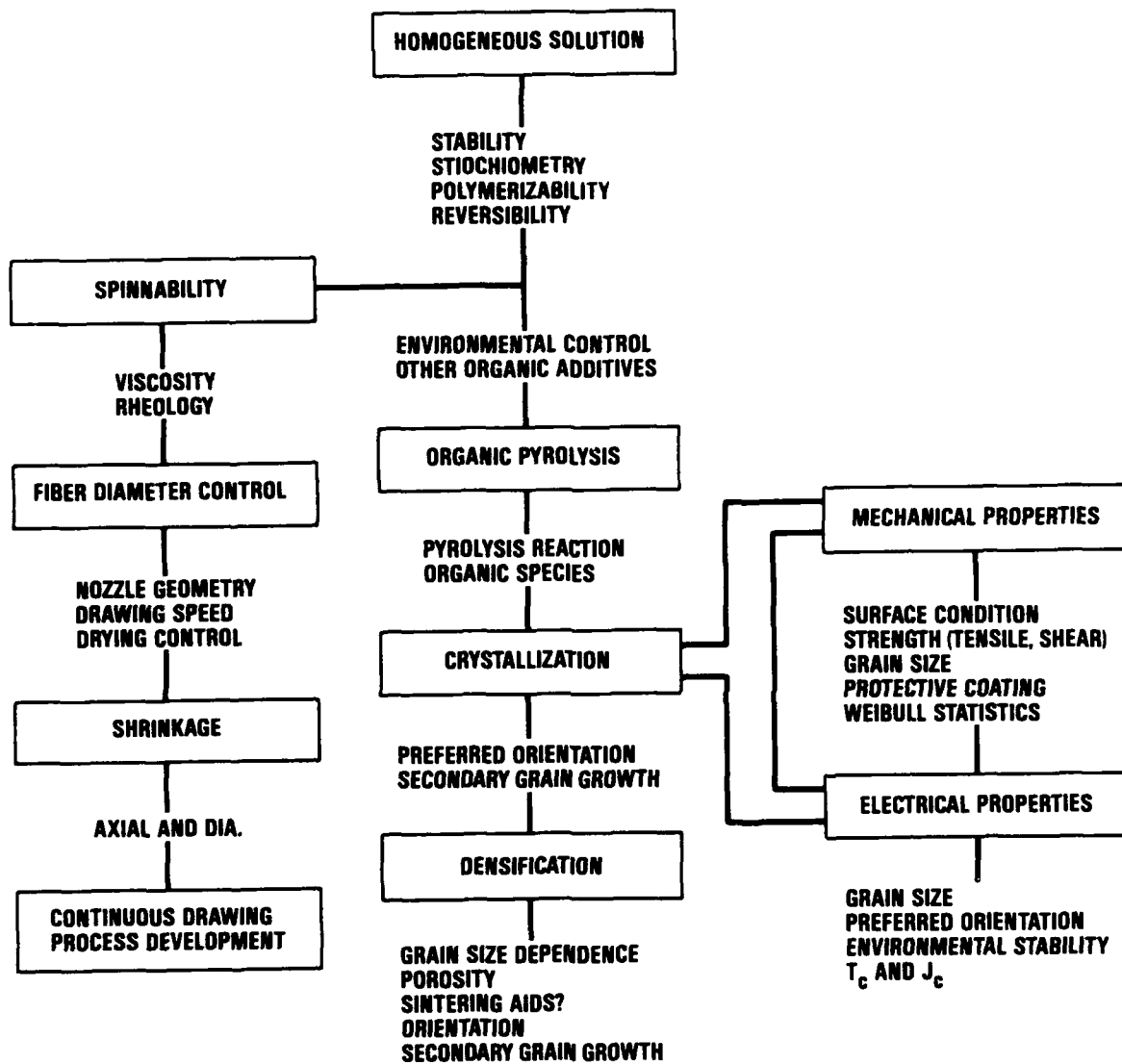


Fig. A-18. Fiber process parameters

Yttrium and barium isopropoxides were mixed in one to two molar ratio and were refluxed to obtain a possible "double alkoxide." An organic acid, e.g., 2-ethylhexanoic acid, was added to this solution in different molar ratios to replace the active alkoxy groups. The molar ratios of 2-ethylhexanoic acid added were 5.17/1, 2/67/1, 2/05/1, 1/5/1, and 1.0/1 of the total molar alkoxides in the solutions. The resultant solutions were exposed to moisture and concentrated to see if they would become viscous liquids. The fiber forming properties of those viscous polymeric materials were examined. After evaporation of solvents, the solutions with greater than 1.5/1 molar ratios of the acid became viscous. This viscous solution was successfully hand-drawn into fibers.

The attached organic acid groups, however, could not be removed by low temperature evaporation. They had to be removed by high temperature pyrolysis. Therefore, the optimal condition will be to maintain the viscous state but reduce the amount of residual organics as much as possible. Reduction of the amount of organic acid in the polymeric materials also have the advantage of smaller shrinkage and less chance of forming barium carbonate during firing. At the present time, the solution with 1.5/1 molar ratio acid addition seems to best fit all these requirements.

A.2.3. Preparation of Solution Containing the Necessary Elements with Fiber and Film Forming Abilities

Copper ethylhexanoate was found to be suitable for homogeneous solution preparation. After mixing yttrium and barium alkoxides in 1:2 ratio, an equivalent amount of 1.5/1 molar ratio of 2-ethylhexanoic acid/alkoxides was introduced to modify the structure of this alkoxide(s). To this homogeneous solution, copper ethylhexanoate propanolic solution was added. The volume of the solution was approximately 400 to 500 ml. By refluxing this solution in a nitrogen atmosphere for 30 to 60 min, a greenish precipitate was formed. When a few milliliters of water-propanol solution was distilled into the solution, the greenish precipitate immediately dissolved, and a dark brownish green solution was formed. This solution was further concentrated until the volume of

the solution was approximately 50 ml. A dark greenish brown precipitate formed on the bottom. The solution was distilled until almost dry. This precipitate was found to completely dissolve in less than 5 ml of benzene. The solution obtained was a clear dark brown solution. This dark brown solution was further concentrated to 0.5 to 1 ml. The flow diagram of the process developed is shown in Fig. (A-19). At this point, the solution became highly viscous and could be easily hand-drawn into fibers (Fig. A-20). Fibers as long as 80 cm were easily drawn. The fibers have adequate mechanical strength immediately after drawing and are flexible. Additionally, the strengths and flexibility were retained for about 5 days. After 5 days in ambient atmosphere, the fibers became more brittle. Short fibers were heat treated up to 900°C for 5 h and characterized as shown in Fig. A-21.

It was noted that even though the solution possessed good fiberizability, it was not at the right stoichiometry. Due to the fact that a small amount of the sample was prepared for the fiberizability test, small errors in the alkoxide solution concentrations and volume measurements can result in large variations in the composition from the intended (123) composition. Further experiments are being carried out to calibrate the solution concentrations to determine if the variations from the intended composition was due to the errors in the starting composition of the solution or due to loss of some element during pyrolysis.

A.2.4. Calibration of Solution Concentrations

From the above discussion, it is obvious that an accurate control method for determination of the solution concentrations is necessary. A method that is accurate, rapid, and adaptable for quality control purposes is titrimetry. The following paragraphs describe the standard titration procedures used for the determination of the concentrations of the solutions. These procedures have to be modified to remove i-propanol and other organic species and to adjust the solution pH before the standard procedure could be used.

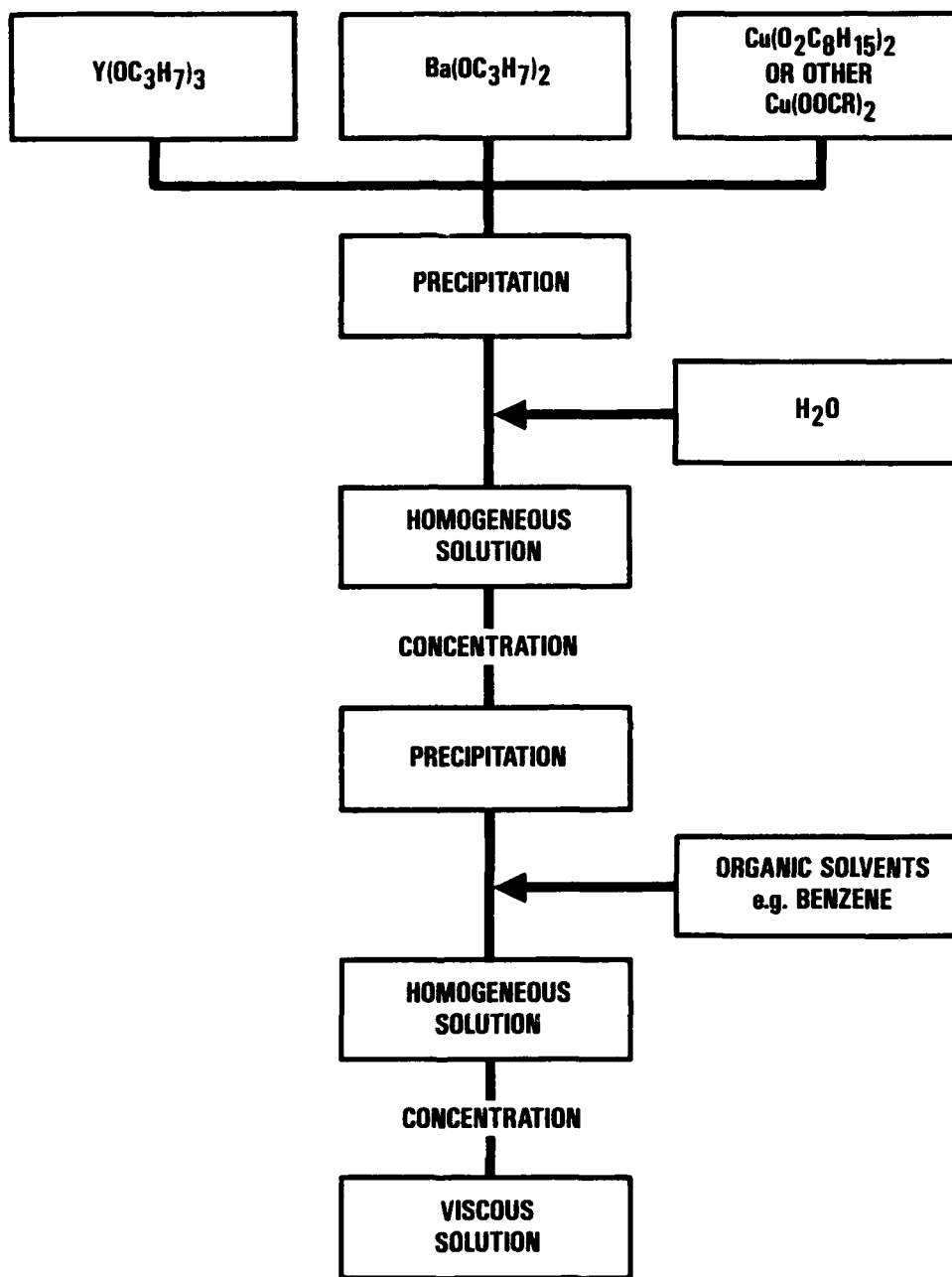


Fig. A-19. Flow diagram for BaYCuO high-temperature superconductor preparation

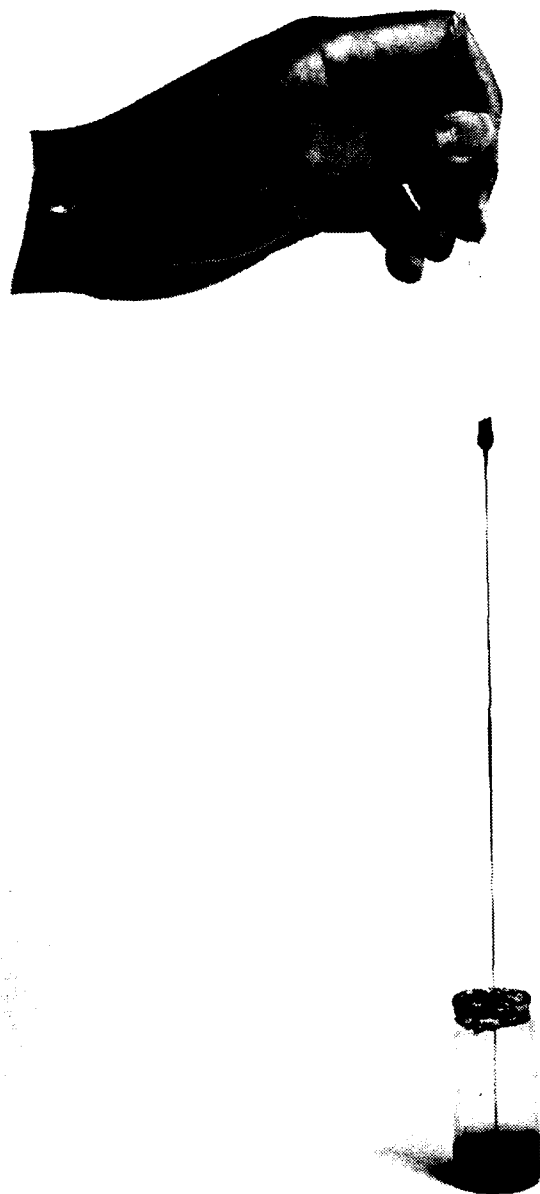
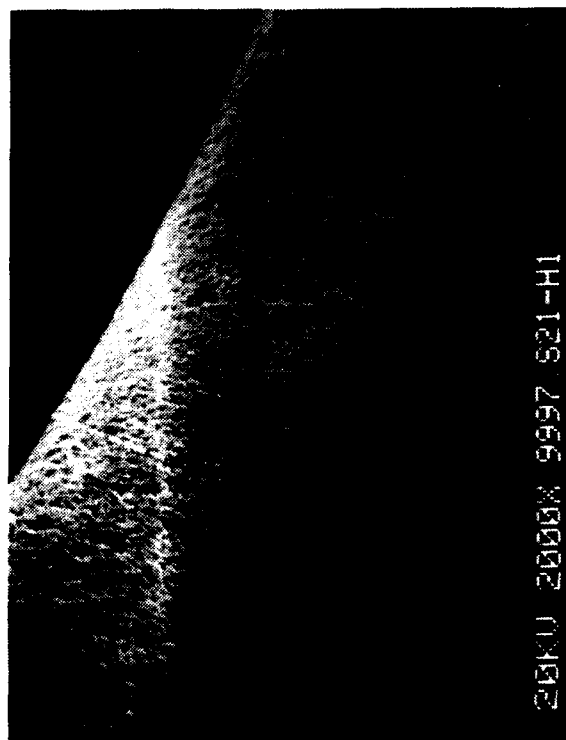
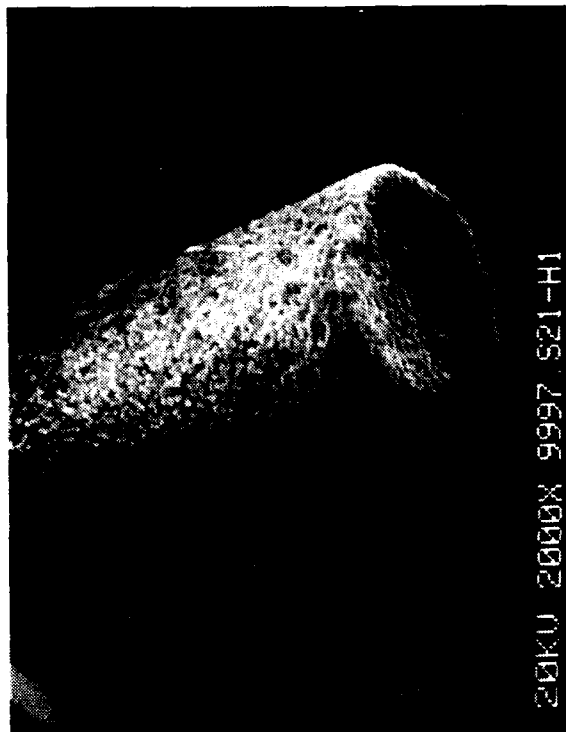


Fig. A-20. Sol-gel derived preceramic superconductor fiber



10 μm

I-784(1)
9-6-88



10 μm

Fig. A-21. SEM micrographs of sol-gel derived ceramic superconductor fibers (900°C, 5 h)

A.2.4.1. Determination of the Concentration of Yttrium Alkoxide Solution

EDTA titration is suitable for determination of rare earths (Ref. 12). To the slightly acidic solution, add a few crystals of NaK-tartrate, 5 ml pH 10 buffer per 50 ml of the solution until the pH of the solution is 8-9, and eriochrome black T indicator, and titrate the boiling solution with 0.1 M EDTA until the color becomes blue.

A.2.4.2. Determination of the Concentration of Barium Alkoxide Solution

To the barium aqueous solutions, add two drops of acetic acid, boil for 5 min., cool, add 10 ml buffer (8.25 g NH_4Cl and 113 ml NH_4OH diluted to 1 liter), and 0.4 g indicator (0.25 g eriochrome black T in 25 g NaCl) and titrate with EDTA reagent solution. For the EDTA reagent solution, dissolve 2.6 g $\text{MgCl}_2 \cdot 6\text{H}_2\text{O}$, 1.9 g $\text{CaCl}_2 \cdot 2\text{H}_2\text{O}$, 28.0 g EDTA and 7.9 ml 50% NaOH in H_2O and dilute to 1 liter. Titrate with EDTA until the color changes from wine-red to blue.

A.2.4.3. Determination of the Concentration of Copper Ethylhexanoate Solution

Method 1 (Ref. 13). Dilute 25.0 ml of the copper solution (0.02M) to about 100 ml with distilled water and add to the weakly acidic solution sufficient amounts of pyridine to produce an intense blue coloration. Add five to six drops of pyrocatechol violet as indicator and titrate with standard EDTA until the solution acquires a yellowish-green (or green) color.

Method 2. For <20 mg in 100 ml acidic solution, add 0.5 g NH_4NO_3 , four to five drops 0.1% pyrocatechole violet indicator and 0.5 N NH_4OH to give a blue color; add 1 to 2 g NH_4OAc and titrate with 0.02 0.1 M EDTA to a yellow color (Ref. 13).

At the present time, the concentrations determined by these methods are within 0.5% to 1% error. Further refinements of these procedures

are in progress to reduce this error. Solutions containing all three elements are being prepared using these calibrated solutions.

A.2.4.4. Error Analysis of Sol-Gel Synthesis

In the synthesis of 123 via the alkoxide sol-gel route, there must be some accumulation of errors in the process. In the 123 material, the short coherence length of circa 1-1.5 nm as an impediment to current flow sets a scale length for the total amount of impurity tolerable in the ceramic. One can ask whether the total error of the sol-gel operations permits synthesis of 123 with sufficient purity, to limit impurity phases to below 1-1.5 nm throughout the sample.

To set the scale length and an approximate purity requirement, consider a 123 particle of radius r , uniformly coated with 1 nm of impurity phase. One can calculate

$$dV/V = 4\pi r^2 dr / (4/3\pi r^3) = 3dr/r = 3(10 \text{ \AA})/r$$

For $r=1$ micron, $dV/V=0.3\%$ as a volume ratio. Within the presumption that the volume ratio is comparable to the mole ratios of 123 to the impurity phases, one has a figure of merit relating the mole fraction impurity to the thickness of a uniform coating on a spherical particle. If the total cumulative error exceeds 0.3%, then each one micron radius particle of 123 has a 1.0 nm impurity phase surrounding it.

TABLE A-1-2
Calibration Tolerances (Class A)

Equipment	Volume(ml)	error%
Volumetric flask	1000 \pm 0.3	0.03
	100 \pm 0.08	0.08
Pipettes	50 \pm 0.05	0.10
	10 \pm 0.02	0.02
	1 \pm 0.006	0.60
Burets	100 \pm 0.20	0.20
	50 \pm 0.10	0.20
	10 \pm 0.04	0.40

Table A-1-2 gives the calibration errors (accuracy) of this volumetric equipment for standard Class A calibrated materials. One can now consider the operations required to synthesize a solution containing all three metals (Y, Ba, Cu). Table A-2-2 gives a summary of the errors propagating during the operations. The operations are the synthesis of three independent one liter solutions of each metal alkoxide, the standardization of each solution by titration, and the making of the mixed solution by pipetting.

TABLE A-2-2
Alkoxide Operations and Errors

I. Synthesis of stock solutions

A) Make $\text{Cu}(\text{OMe})_2$, 0.100 M, 1.000 L 12.5546 \pm 0.001 g weighed out add solid to make up 1.000L solution in volumetric flask	0.008 % error 0.030
Net error in making solution A	<u>0.04%</u>
B) Make titrant solution (1.000 L of 0.100 M EDTA solution) 29.224 \pm 0.001 g weighed out add solid to 1.000 L volumetric flask, add water	0.004 % error 0.03
Net error in making titrant solution	<u>0.04%</u>
C) Titrate stock solution with titrant Add 50 ml of A with pipette Add 50 ml of B with buret	0.10% % error 0.20%
Net error in titration	<u>0.30%</u>
Net error in making and standardizing one metal solution (Sum A, B, C net error)	0.40%
Net error in making and standardizing three metal solutions	<u>1.20%</u>

II. Make mixed solution of three metal solutions

D) Pipette 50 ml of each solution (3 x 0.1%)	0.3 %
Total error (I + II) to make mixed solution:	<u>1.5%</u>

The above error analysis exemplifies how easily errors can propagate up to the one percent level, using volumetric equipment. This analysis presumes that three different standardizing titrants are required for the three metal solutions. This analysis also presumed the starting materials, made from solid alkoxides, are completely pure, with no second phases or impurity phases. Simply, the analysis sums the errors, rather than trying to estimate any cancellation of errors among operations by further statistical analysis. The analysis also does not take into account further "accuracy" by performing the standardizations multiple times and averaging the results. Thus, this simple error analysis is overly conservative, but it does give a measure of the difficulty in limiting errors in volumetric work. Any worker making one liter metal compound solutions in this field of work is probably working at near a 1% error in the composition of his solution.

A second source of potential error occurs when one is working with nonaqueous solutions: temperature variations of the stock solution density. For pure methanol and isopropanol, the relative error in their volumes (per gram of solvent) is $0.12\%/^{\circ}\text{C}$ and $0.11\%/^{\circ}\text{C}$ near $20-25^{\circ}\text{C}$. A 1.000 L volumetric flask of methanol, made at 20°C , will measure 1.006 L at 25°C . A solution which is 1.000 M at 20°C in methanol will be 0.994 M at 25°C , due to this volume expansion of the solvent. Thus, temperature control of the solutions is a significant component of reducing the total error. By contrast, aqueous solutions have a volume change of about $0.021\%/^{\circ}\text{C}$ near 20°C . Thus, the concentrations of aqueous solutions are less sensitive to temperature variation than are alcohol solutions by a factor of 5 to 6.

In looking at the error analysis, there are several places where errors can be reduced. The Class A calibration errors refer to accuracy and not precision. Careful calibration of each pipette in the lab may well reduce the error in delivery below the quoted error. The precision of the given pipette may be better than the accuracy of the quantity nominally delivered. Second, one can reduce the amount of

buretting required and use larger volumes of solution to reduce the errors in measurement. Third, one can rely on more gravimetric analysis, rather than volumetric analysis, since weighing has a smaller relative error (0.01%, or 10.000 ± 0.001 g). For example, an analysis of a solid state reaction of the three component oxides results in a total error of 0.2% in the weighing out of the three oxides. However, this 0.2% cannot be directly compared to the 1.5% solution error quoted above, since the solid state synthesis did not include any standardization of the component oxides. When a similar standardization is included, the errors are about the same, about 1 to 2% for the solid state synthesis.

In looking at the error analysis above, it first appears that while 0.3% total error is required, the solution method and solid state synthesis methods will both fail. This conclusion is not entirely warranted. First, the volume percent error presumed a one micron radius 123 particle, with a uniform impurity coating. The impurities may well segregate to form their own grains, so that the 123 particles may have cleaner grain boundaries than the above model presumed. Second, the sol-gel method can prepare materials of finer grain size than other techniques, such as solid state synthesis. Reducing the grain size to 0.1 micron radius will raise the volume percent error to 3%. Thus, cumulative errors of 1.5% will result in only a 0.5 nm thick impurity phase uniformly coating each particle. If the fine grained ceramic 123 can be achieved and maintained, each grain boundary ought to have a thinner impurity phase coating, compared to a larger grain size material. Processing conditions to limit grain growth strongly impact the ability to maintain the fine grain microstructure requirement. In light of this analysis, sol-gel processing would appear to have a favorable position, relative to many other techniques, in obtaining and maintaining a fine grain microstructure.

A.3. FIBER HEAT TREATMENT

A.3.1. OPTIMIZATION OF FIBER HEAT TREATMENT SCHEDULE

Optimization of heat treatment schedule for 123 fiber with adequate mechanical strengths as well as acceptable electrical properties is the primary objective under the program. The fiber integrity and fiber shape and morphology are strongly influenced by the organic removal rate between 200° and 500°C. The ideal conditions for organic removal of any preceramic fiber should be slow, decomposition and diffusion, rather than rapid removal of volatile species from the interior of the fiber. Since the organic pyrolysis is a kinetic process, both processing temperature(s) and time(s) need to be determined.

From a TGA study, shown before, most of the organic pyrolysis occurs between 200° and 400°C. Considerable weight loss occurs from 220°C to 360°C at a 10°C/min heating rate in flowing oxygen. To determine the time needed to slowly remove the organics in the as-drawn fiber at this temperature range, isothermal TGA was performed on 0.5 to 1 mm diameter fibers from 200° to 500°C at 50°C intervals for 2 h at each temperature in flowing oxygen. The objective of this experiment was to learn the time needed to reach a constant weight at each temperature. Figure A-3-1 shows that the isothermal weight losses at 200° and 250°C is critical for the slow decomposition and diffusion of the organic species. A longer hold, 5 h at these two temperatures, revealed that the weight losses at 200° and 250°C have not yet reached a constant weight Fig. A-3-2. Therefore, even longer time may be needed at these two temperatures. Additionally, it should be noted that the time needed also depends on the fiber diameter. It is expected that the time required is shorter for thinner fibers. The prolonged time needed is thought to be due to the slow diffusion and decomposition of the organics from the interior of the fiber. The isothermal weight losses above 250°C reach constant weight within 1 to 2 h. Rapid heating rate in the range of 100° to 400°C generally produces a dense crust on the fiber surface with porous interior.

Sample: 9997.929
Size: 10.1880 mg
Method: 2 HRS/TEMP
Comment: O2 ATMOSPHERE 10°C/MIN

TGA

File: 1801.01
Operator: T. TAMORIA
Run Date: 22-Feb-88 18:31

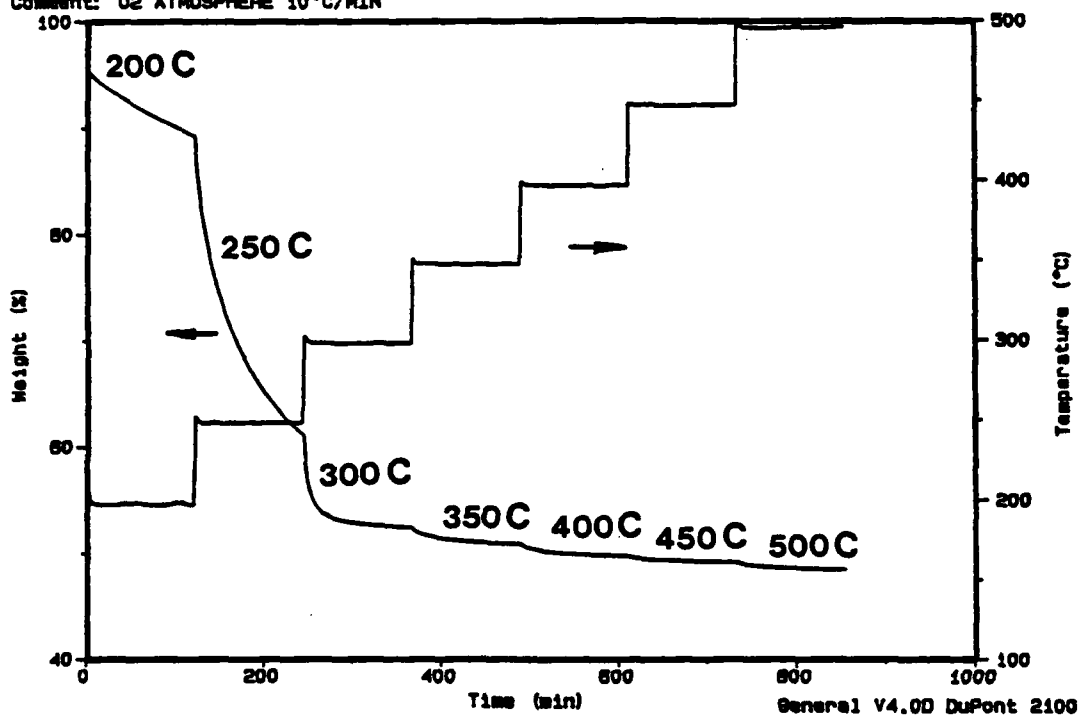


Fig. A-3-1. Isothermal TGA on preceramic fiber (0.5 to 1 mm diameter) with 2 h at each temperature

Sample: 9997.928
Size: 11.1270 mg
Method: X HRS/TEMP
Comment: 02 ATMOSPHERE

TGA

File: 1813.81
Operator: T. TAMORIA
Run Date: 3-Mar-88 16:58

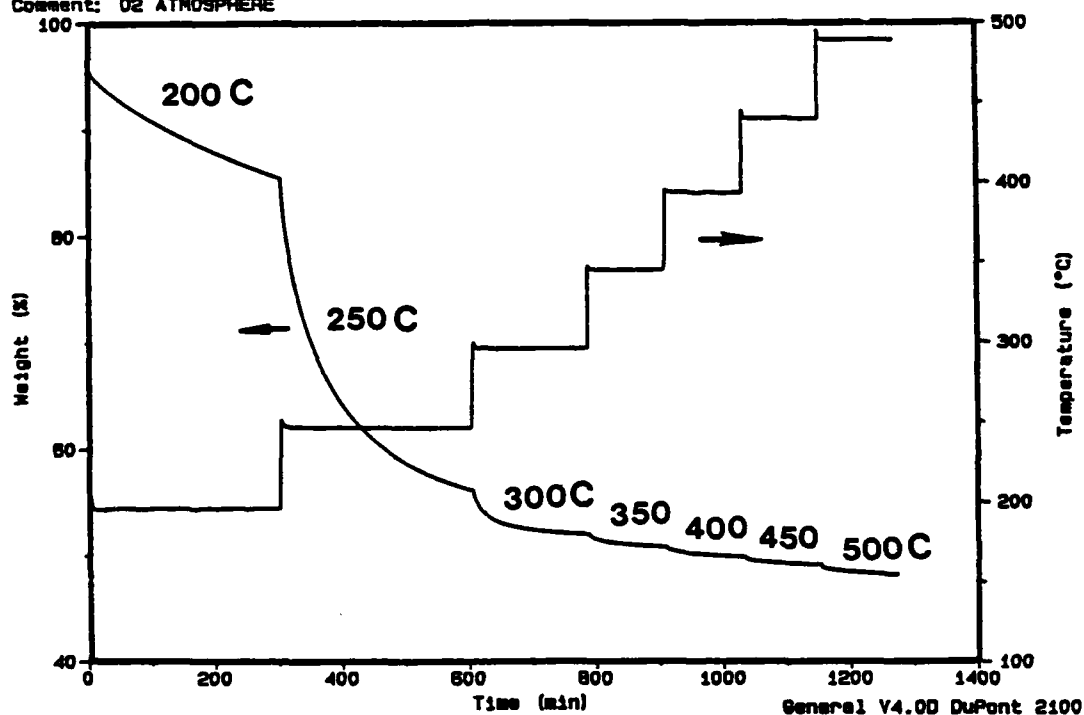


Fig. A-3-2. Isothermal TGA curve of preceramic fiber for 5 h hold at 200° and 250°C and 2 h hold at 300°C and above

Heat treatment schedule between 600° and 900°C will depend on the time and temperature where a single phase $\text{YBa}_2\text{Cu}_3\text{O}_{7-x}$ with desirable microstructure can be obtained (either by direct crystallization from the amorphous phase or fine-scale solid state reactions). Systematic experiments were conducted to determine the crystalline phase at the aforementioned temperature range. In order to distinguish the influence of the low temperature heat treatment (<400°C) from the higher temperature range, a fast heating rate is used (half an hour to reach the designated temperature) to study the phases existing between 700° and 950°C. Even though the experiment has not been completed at the present time, the x-ray results indicate that at 750°C, there are BaCO_3 and other phases, such as $\text{Y}_x\text{Cu}_2\text{O}_5$, present for 1 h heat treatment. Single phase of $\text{YBa}_2\text{Cu}_3\text{O}_{7-x}$ are obtained at 900°C for 4 h Fig. A-3-3. The tentative time-temperature-phase diagram for the appearance of $\text{YBa}_2\text{Cu}_3\text{O}_{7-x}$ phase is shown in Fig. A-3-4. The present research goal is to determine the shortest temperature and/or time boundary for the 100% $\text{YBa}_2\text{Cu}_3\text{O}_{7-x}$ phase. Though the time required for obtaining single phase $\text{YBa}_2\text{Cu}_3\text{O}_{7-x}$ may be greater than 4 h, it is presently believed that the time required for the full-densification, which is being studied separately, is the determining factor for eventually choosing the time and temperature profile for the fiber processing.

By stepwise heat treatment below 500°C and slow heating from 500° to 900°C, dense crust and hollow core morphology of the sol-gel derived fibers have been suppressed, and more or less uniform porous fibers have been obtained Fig. A-3-5. It is clear that (in order to prevent differential rates sintering) the same density throughout the fiber cross section is required before final densification heat treatment.

The heat treatment schedule will be extended beyond 900°C, from 870° to 1000°C, in order to determine the optimum temperature and time needed where full-densification can be achieved with no exaggerated

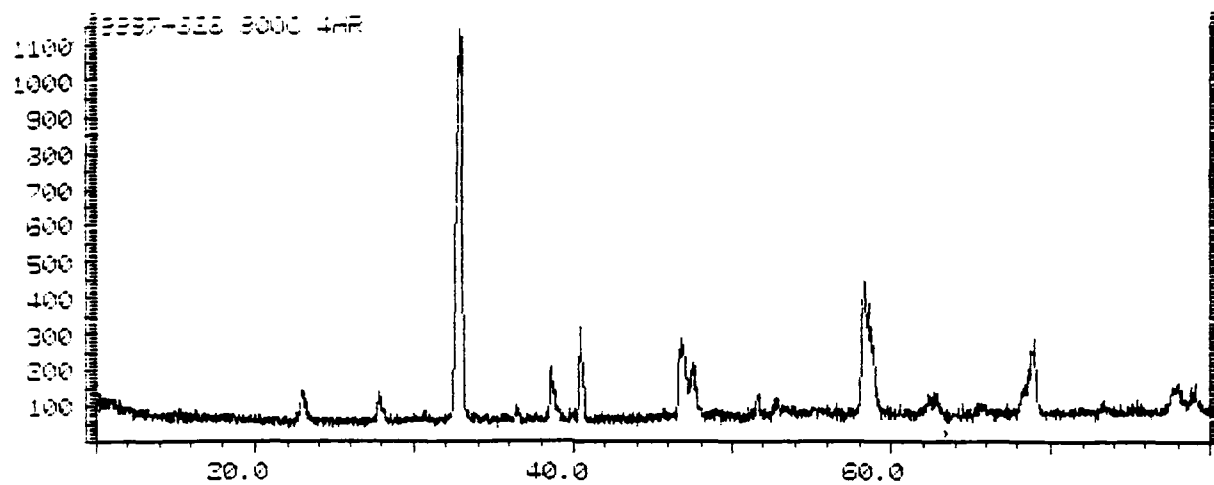


Fig. A-3-3. X-ray diffraction of sample heat treated at 900°C
4 hr in flowing oxygen

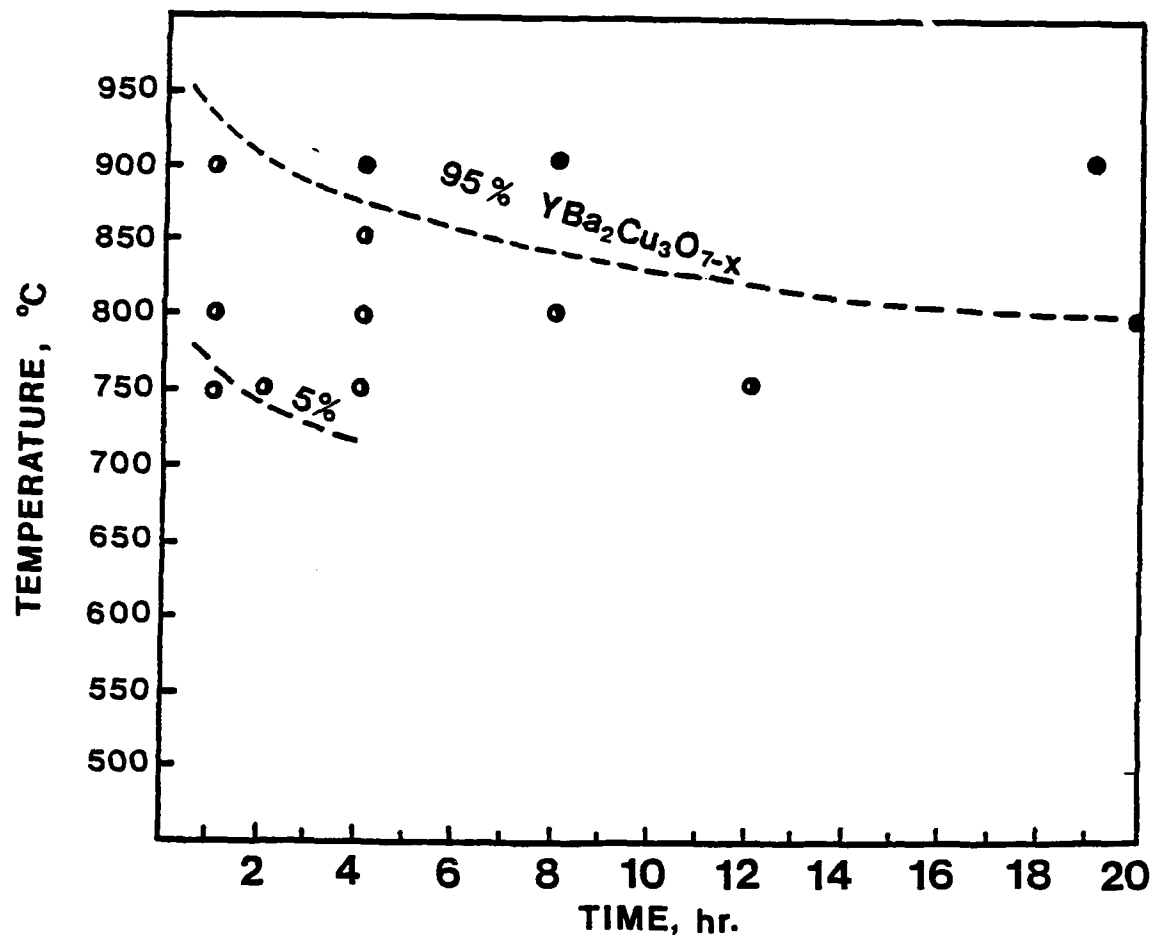
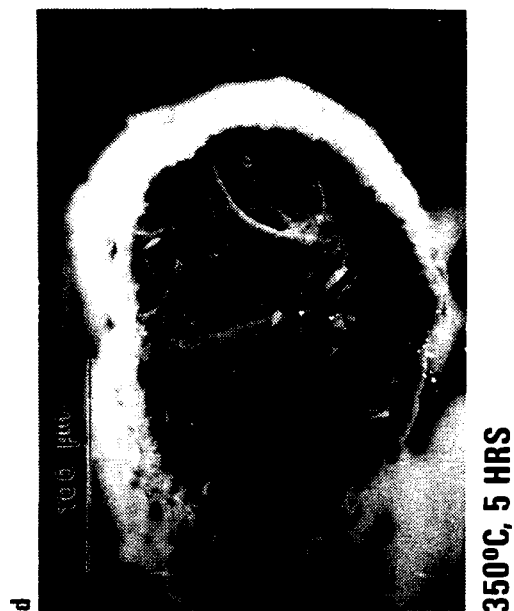
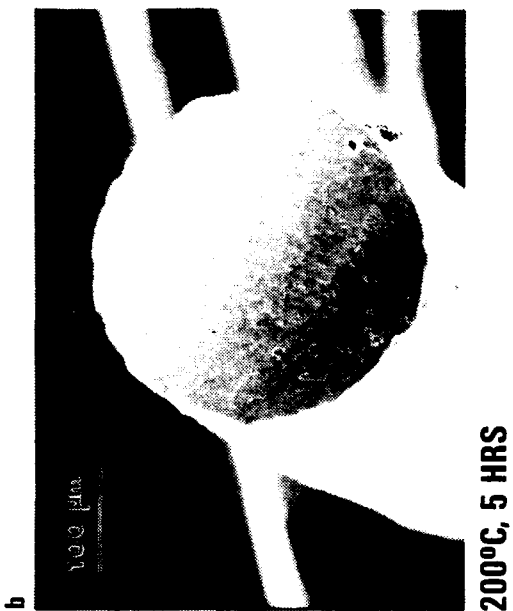


Fig. A-3-4. Time-temperature-phase diagram for the formation of $\text{YBa}_2\text{Cu}_3\text{O}_{7-x}$



J-033(10)
4-6-89

Fig. A-3-5. Microstructural evolution of the fibers during slow stepwise organic pyrolysis



(a) 900°C, 3 HR

10 μm



(c) 950°C, 10 MINS

10 μm



(b) 920°C, 2 HRS

10 μm



(d) 970°C, 2 HRS

4 μm

J-047(12)
4-14-89

Fig. A-3-6. Effect of high temperature annealing on the grain size and surface smoothness of the fiber

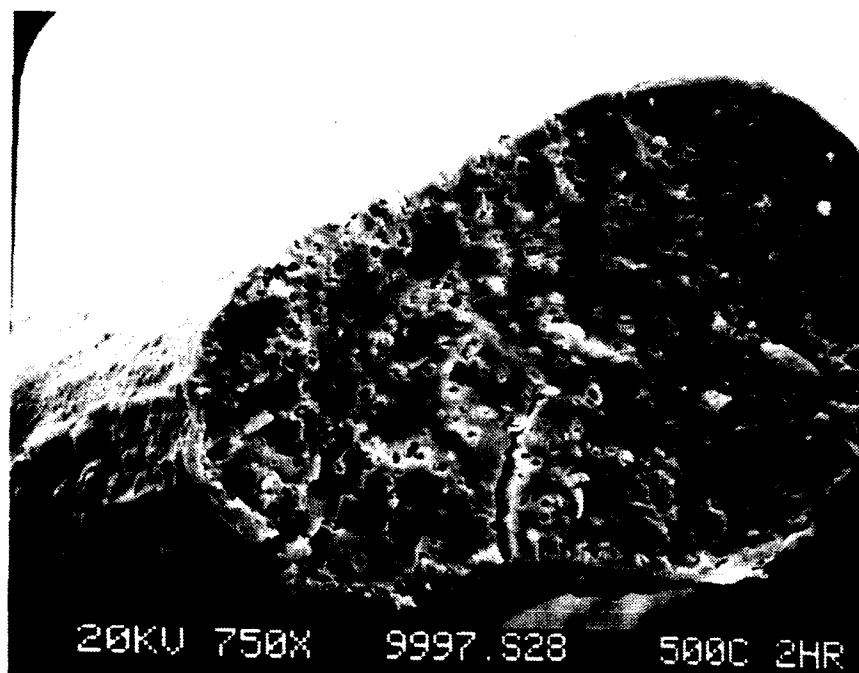


Fig. A-3-7. Pores formation in the fiber using high heating rate to 500°C and hold for 2 hours

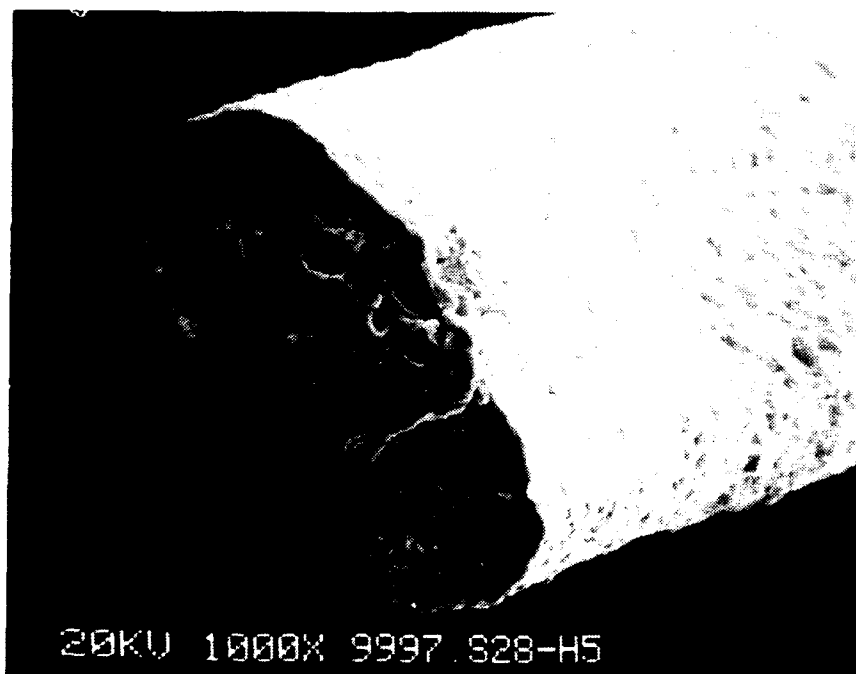


Fig. A-3-8. Dense 123 fiber obtained by proper heat treatment

grain growth. It has been found, by others, that abnormal grain growth occurs when the fiber is heated above 920°C. Fibers made under this program that have been heat treated to 970°C, 2 h, exhibit faceted crystals and are mechanically weak Fig. A-3-6.

Grain growth was observed above 950°C as shown in Fig. A-3-7. This grain growth around 950°C may signify the presence of liquid phase due to a slight off-stoichiometry in the composition.

A.3.2. FURTHER IMPROVEMENT IN COMPOSITION STOICHIOMETRY

As described before, the process of preparation of solution containing all three elements is fairly reproducible. Fibers can be successfully drawn from all the solutions. However, most of the fibers prepared from these solutions after heat treatment at 875 to 920°C contain not only $\text{YBa}_2\text{Cu}_3\text{O}_{7-x}$ but still a small amount of Y_2BaCuO_5 or BaCuO_2 . In order to further improve the solution stoichiometry and to eliminate the liquid phase formation, the combination of composition of the solution, and the optimal process conditions are needed. Additionally, it is imperative to eliminate liquid phase for optimum high current density and to avoid weak link behavior in the fiber.

These slightly off-stoichiometry may arise from several reasons. As indicated previously (see Section 2.4.4), it may be due to the inaccurate calibration in the stock solution, drifting of the concentration of the stock solutions with time, large total volumetric measurement errors during pipetting of the solutions, or variation of the volume of the solutions due to temperature fluctuation.

To achieve the precise stoichiometry, all the stock solutions have been re-calibrated (original calibrations are in the range of 0.1 to 0.5 at%) and 10 more batches of the solutions have been prepared. The compositions of these solutions are either right on the 123 composition or 2 at% more or less in yttrium, barium, or copper. It is intended to see

if the slightly off-stoichiometry can be corrected by this approach. The fibers prepared from these solutions were rapidly heat treated at 900°C for 4 to 8 hours, and the phase purities were determined by x-ray and DTA. Some of the results are shown in Fig. A-3-9. As can be seen in the figure, x-ray indicates the presence of a small amount of second phase. This second phase results in a liquid phase formation at 960°C (two are at 950°C) in DTA. However, it is possible to eliminate the second phase by carefully controlling the process as indicated by the smaller peak area in 960°C peak in one sample (10105-50) and none in another sample (powder, #10105-S35-P3). We are currently improving the consistency of phase purity in the process.

A.3.3. CONTINUOUS FIBER DRAWING DEVELOPMENT

Fiber drawing equipment has been completed to study the conditions, including the solution concentration, viscosity, evaporation of solvent, drawing speed, etc., required for the continuous drawing process. The conditions for hand-drawing and mechanical-drawing require different solvent evaporation rates. Continuous fibers have been successfully drawn from the solution by either up-drawing or down-drawing techniques Figures A-3-10(a) and A-3-10(b). The fiber diameter can be varied depending on the up- or down-drawing speeds and/or diameter of the spinneret (Fig. A-3-11).

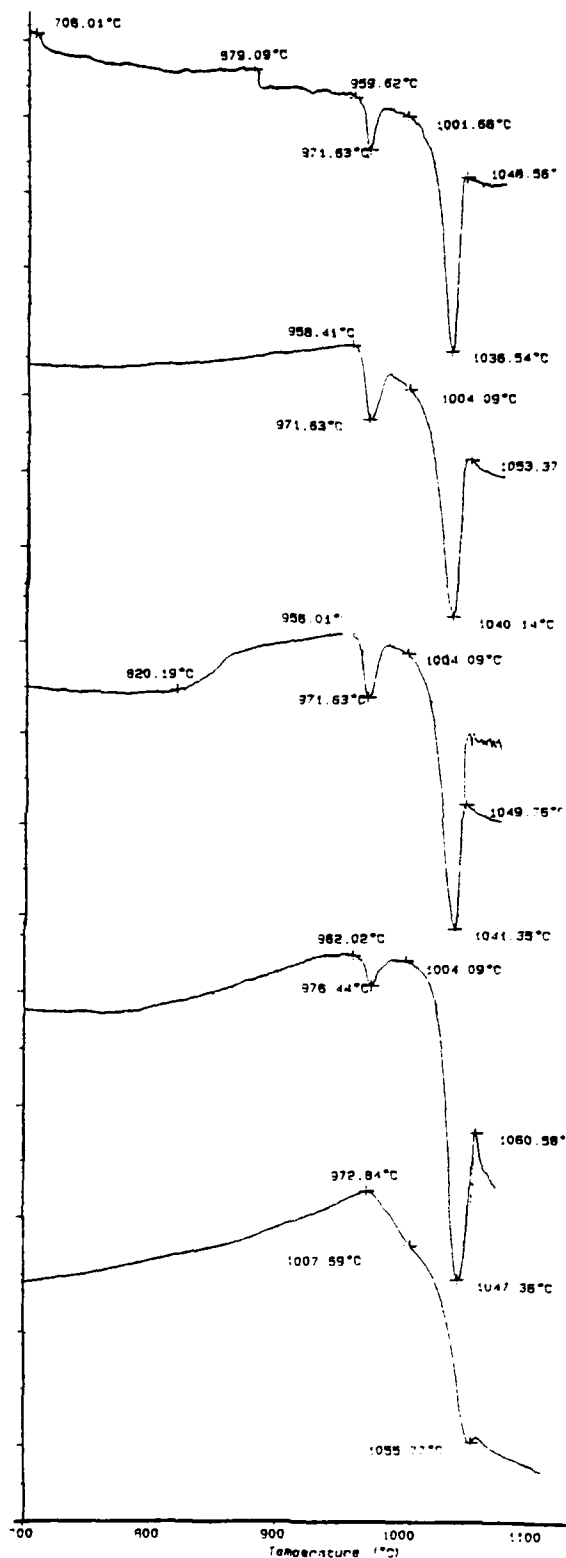
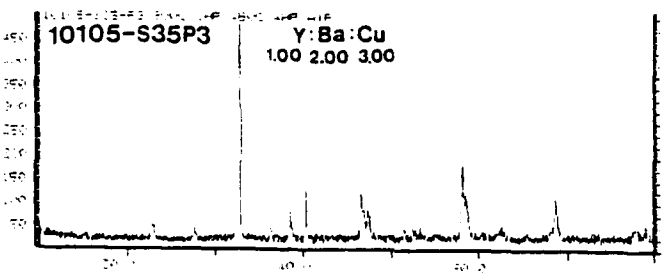
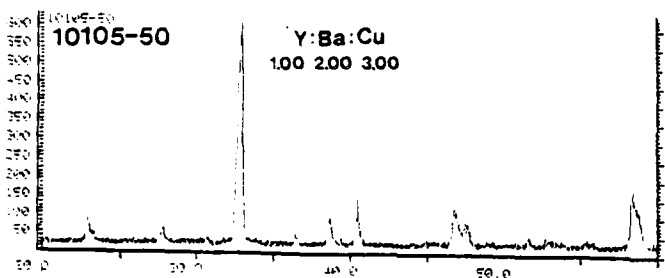
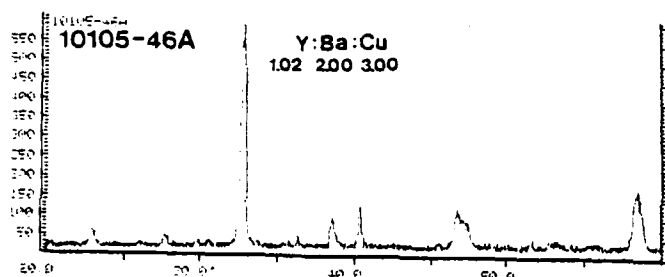
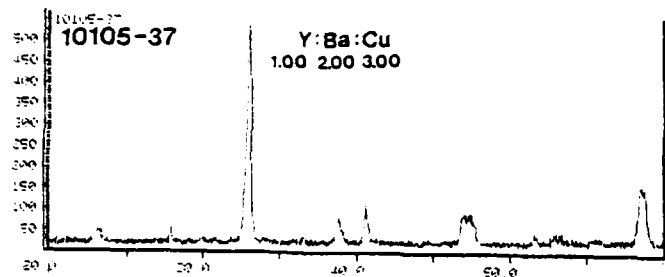
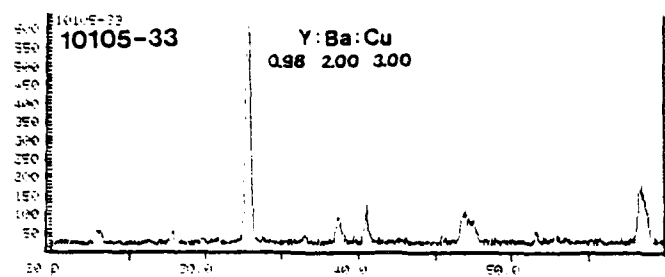


Fig. 3-9. X-ray and DTA characterization of some of the fiber batches

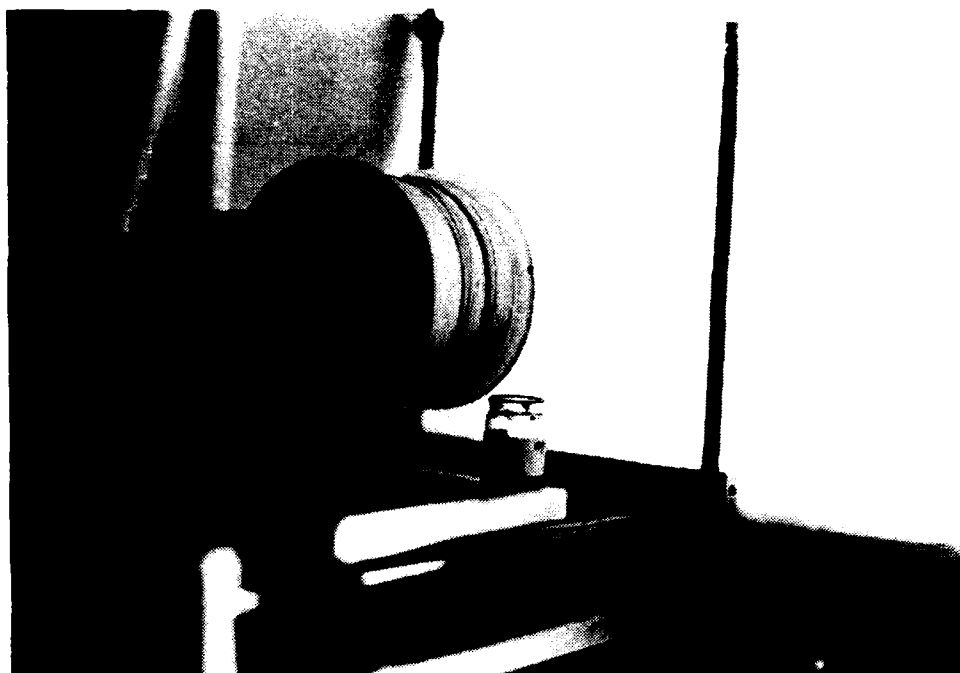


Fig. A-3-10-(a). Continuous preceramic fibers mechanically drawn (up-drawing method) from the polymeric solution

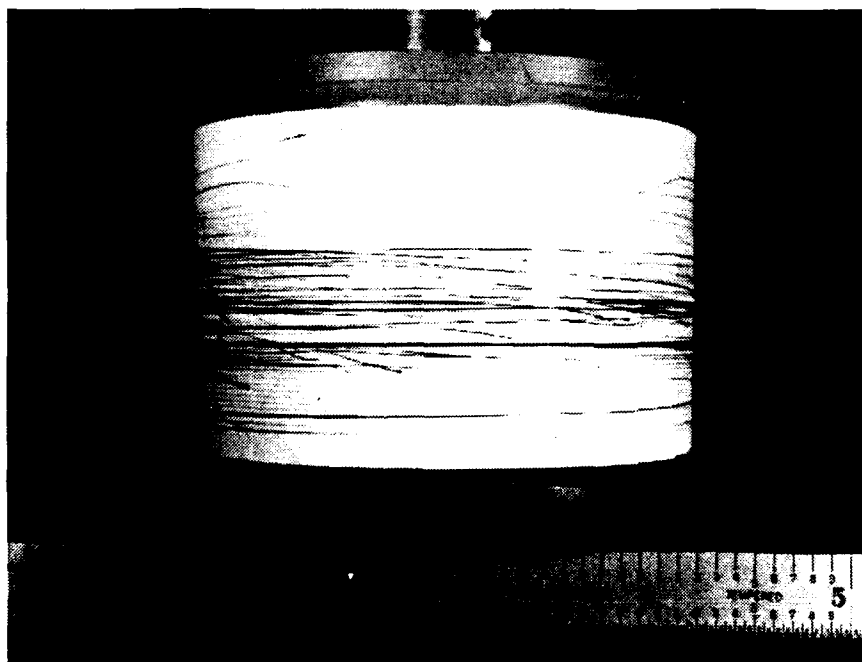


Fig. A-3-10(b). Continuous preceramic fiber spool prepared by the up-drawing method

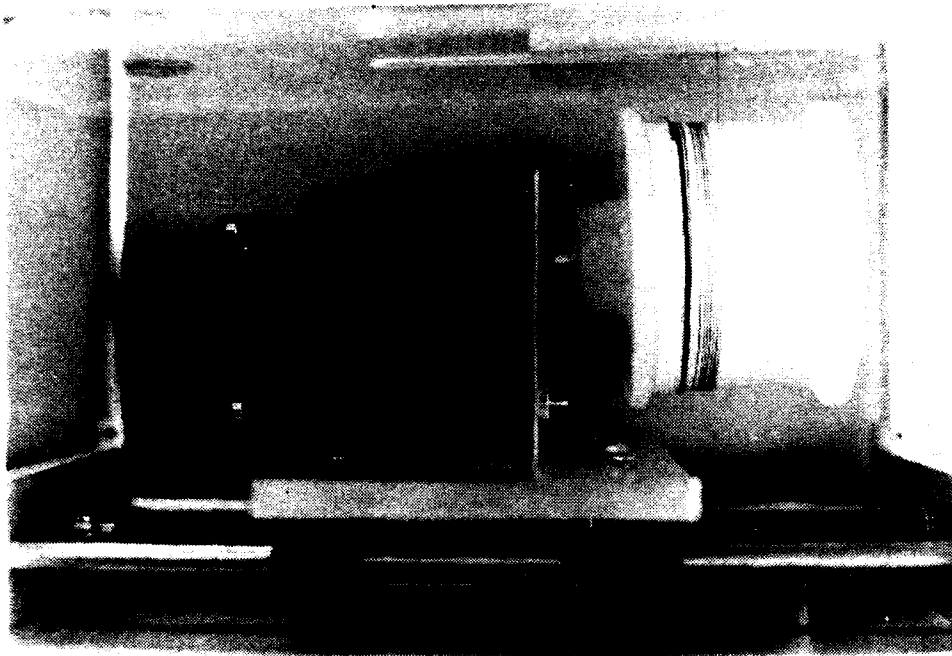


Fig. A-3-11. Continuous preceramic fiber prepared by the down-drawing and extrusion method

A.3.4. FIBER PREFERRED CRYSTALLOGRAPHIC-ORIENTATION DEVELOPMENT (TEXTURING)

Due to the anisotropy of orthorhombic $\text{YBa}_2\text{Cu}_3\text{O}_{7-x}$ crystal, the electrical conducting properties are strongly preferred crystallographic orientation dependent. It has been shown that it is necessary to align the crystals with their a-b plane parallel to and their c-axis perpendicular to the fiber axis in order to maximize the critical current density. Preferred orientation can be achieved in metallo-organic derived $\text{YBa}_2\text{Cu}_3\text{O}_{7-x}$ fibers either by melt-texturing, heterogeneous nucleation through seeding with the help of magnetic field or surface crystallization.

The heterogeneous nucleation through seeding the fine crystallites with the assistance of magnetic field alignment will first be tried. In order to seed the viscous solution, fine crystallite size 123 has been produced. For a fiber of 20 to 50 microns of final diameter, the seeds should be well below the micron-size, non-agglomerated, and well-crystalline. Large seeds will generate rough surface as well as enhance the secondary grain growth in the fiber. These will surely deteriorate fiber mechanical strength.

Preferred orientation development in the fiber through seeding of fine $\text{DyBa}_2\text{CuO}_{7-x}$ crystallites with the assistance of magnetic field alignment is in the stage of modification of the existing fiber drawing equipment. A magnet has been designed and built. The magnetic field strength can be adjusted by the distance between the pole pieces. The field strength of the designed magnet is 0.75 T at 0.5 cm spacing.

A.4. ELECTRICAL AND MAGNETIC PROPERTY DETERMINATION

A.4.1. RESISTIVITY MEASUREMENT

In this section, the measurements made on $\text{YBa}_2\text{Cu}_3\text{O}_{7-\delta}$ powders and some of the first sol-gel derived $\text{YBa}_2\text{Cu}_3\text{O}_{7-\delta}$ fibers are reported. Powders prepared by the sol-gel technique were pressed into pellet form, annealed in O_2 at 973°C for 14 h, and cooled in O_2 over a 12-h period. X-ray diffraction scans of the powders and reground pellets were identical and consistent with a high- T_c perovskite structure with less than 5 volume percent of impurity phases. Rectangular specimens were cut from the pellets with a diamond wheel saw. Figure A-4-1 shows the resistivity of an O_2 -treated specimen as a function of decreasing temperature T in zero applied magnetic field. We define T_n as the temperature at which the resistivity drops to the fraction n of the extrapolated normal-state value. The critical temperature $T_c = T_{0.5}$ has a value of 91K with a transition width $\delta T = T_{0.9} - T_{0.1}$ of less than 2 K. These values are in good agreement with published values for samples prepared by solid-state reaction (Ref. 14).

Resistivity measurements were also carried out in applied magnetic fields H up to 10 T. The transitions broadened with increasing H , suggesting some inhomogeneity and/or magnetic field anisotropy. Figure 17 shows upper critical fields H_n at which the resistivity drops to the fraction n of the extrapolated normal-state value at the field. Ignoring the curvature of H_{c2} vs T in low fields, the initial upper critical field slope $(dH_{c2}/dT)_{T_c} = -2.75 \text{ T/K}$ for $n = 0.1, 0.5$, and 0.9 are shown in Fig. A-4-2. These results are also in agreement with data reported for samples prepared by solid-state reaction (Ref. 8).

A.4.2. MAGNETIC SUSCEPTIBILITY

Magnetic susceptibility data were taken by first cooling the sample in zero field; then a field of $H = 25 \text{ Oe}$ was applied and the susceptibility was measured for increasing temperatures. Subsequently, the

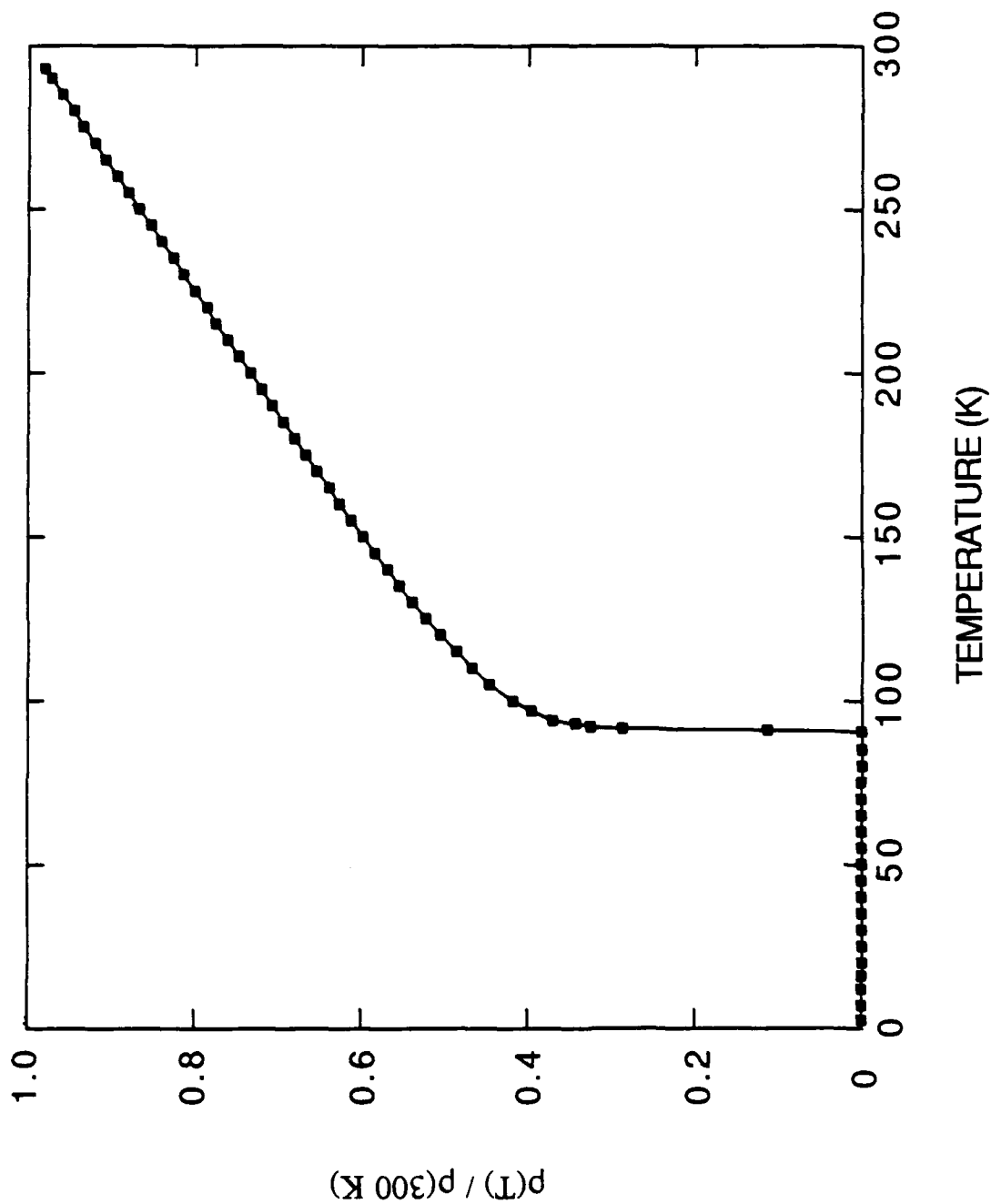


Fig. A-4-1. Resistivity, normalized to the value at 300 K, as a function of decreasing temperature for $\text{Y}_1\text{Ba}_2\text{Cu}_3\text{O}_{7-\delta}$

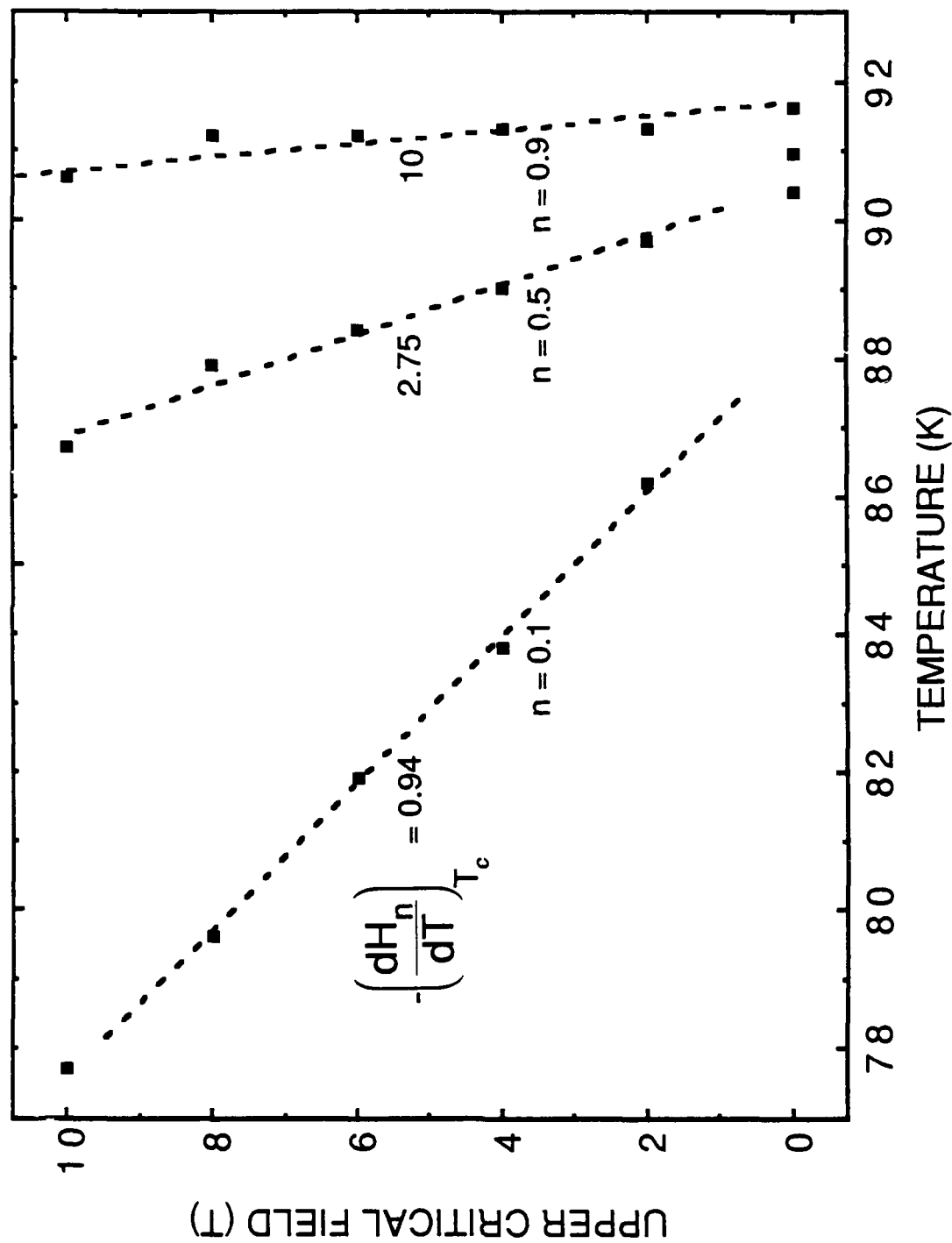


Fig. A-4-2. Upper critical field H_n as a function of temperature for $Y_1Ba_2Cu_3O_{7-\delta}$ powder. H_n is the field at which the resistivity drops to a fraction n of its extrapolated normal-state value at the field. Values are shown for $n = 0.1$, 0.5, and 0.9.

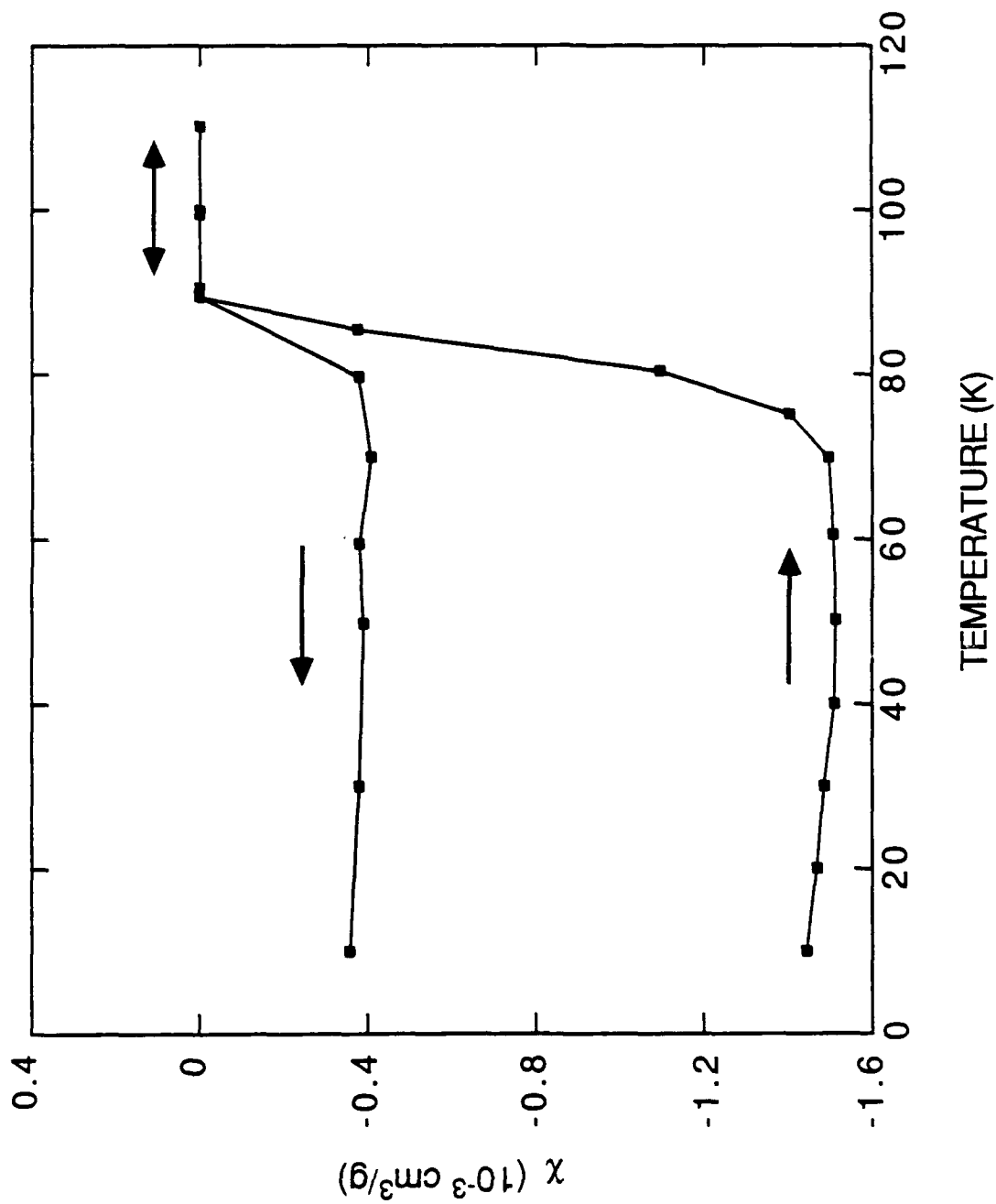


Fig. A-4-3. Magnetic susceptibility as a function of temperature for $\text{Y}_1\text{Ba}_2\text{Cu}_3\text{O}_{7-\delta}$ powder. A magnetic field of 25 Oe was applied after the sample was cooled in zero field. The sample was then warmed through its superconducting transition and subsequently cooled again.

Meissner signal was measured by cooling in the applied field, and is shown in Fig. A-4-3. The onset of superconductivity occurs below 89 K. The strength of the diamagnetic signal was greater than the Meissner signal by a factor of 3.9.

A.4.3. MAGNETIZATION MEASUREMENTS

The magnetization M was also measured as a function of magnetic field. After cooling the sample in zero applied field, the magnetic field was increased to 50 kOe and decreased back to zero at a fixed temperature of 5K. These results, shown in Fig. A-4-4, can be used to estimate the critical current density using Bean's model (Ref. 15). In this model, the current density is assumed to be uniform and is given by

$$J_c(\text{A/cm}^2)a = F\Delta M(\text{emu/cm}^3)d/(\text{cm}),$$

where F is a geometrical factor such that $F \approx 34$ for a sphere of diameter d (Ref. 16), and $F \approx 30$ for a long cylinder of diameter d with H parallel to the cylindrical axis (Ref. 17). Scanning electron micrographs of the sample reveal a granular structure with irregularly shaped grains varying in size from $<1 \mu\text{m}$ to $\sim 10 \mu\text{m}$. If intergranular coupling is negligible in the presence of the applied field, then a value of $d = 5 \mu\text{m}$ in Bean's model gives an order of magnitude estimate of the intrinsic critical current density associated with an individual grain. Estimates of J_c as a function of the applied field are shown in Fig. A-4-5, where the values of $F = 30$ and $d = 5 \mu\text{m}$ were used. At 5 K, the critical current density has values of $J_c \sim 6.2 \times 10^6 \text{ A/cm}^2$ at 3 kOe and $J_c \sim 2.0 \times 10^6 \text{ A/cm}^2$ at 40 kOe. These values are consistent with those obtained for bulk single crystals (Ref. 18-19) and field-aligned powders (Ref. 20).

The magnetic susceptibility for some of the first $\text{Y}_1\text{Ba}_2\text{Cu}_3\text{O}_{7-\delta}$ sol-gel fibers have also been measured. For a sample annealed in air at

850-900°C for 6 h and at 500°C for 3 h shown in Fig. A-4-6, it was found that the onset of superconductivity is at approximately 86 K. Although the magnetic transition was broad, we believe that it can be narrowed in samples prepared under more carefully controlled annealing conditions and with continuing refinements in the future sample preparation techniques.

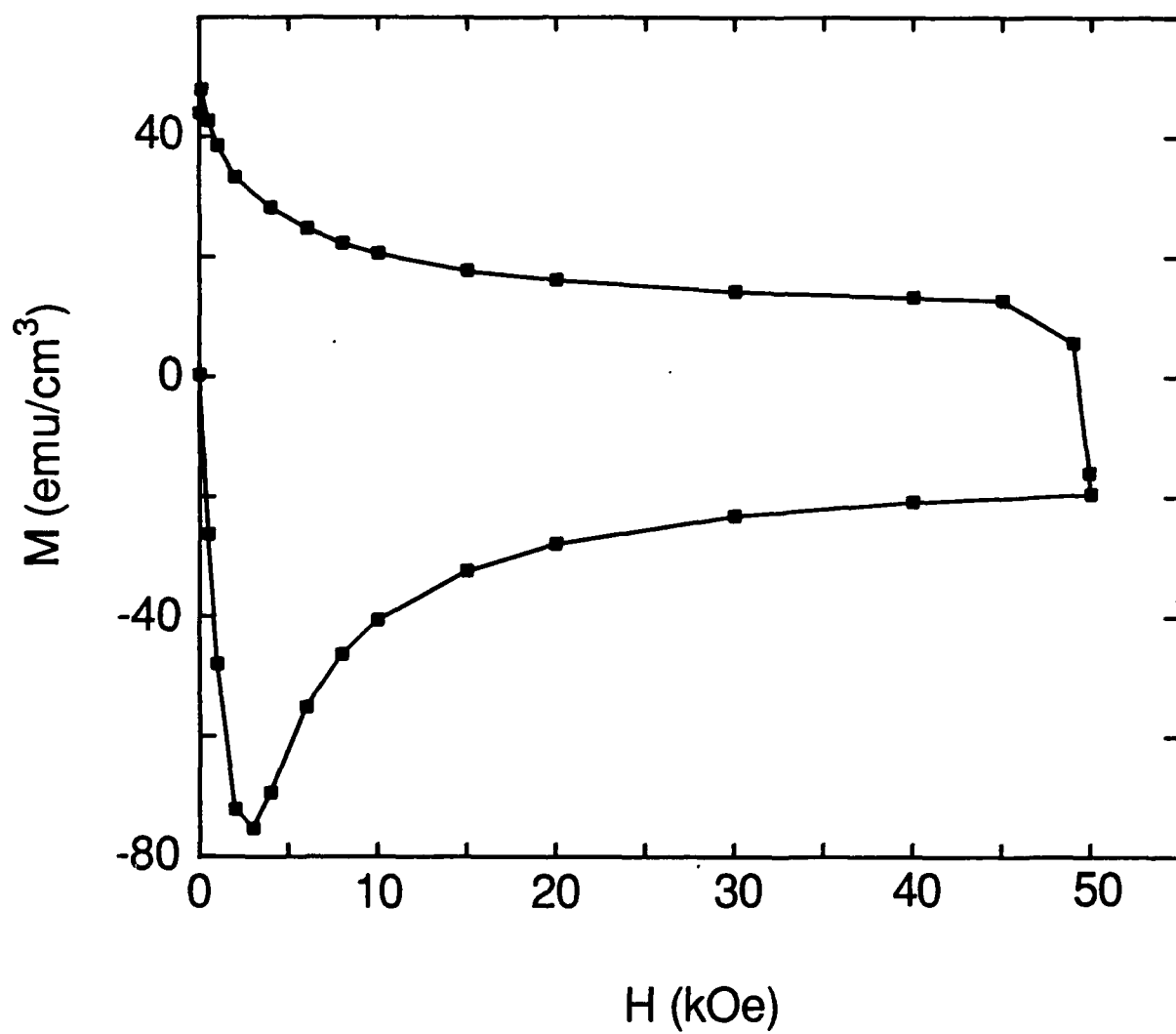


Fig. A-4-4. Magnetization as a function of magnetic field after cooling the sample in zero applied field

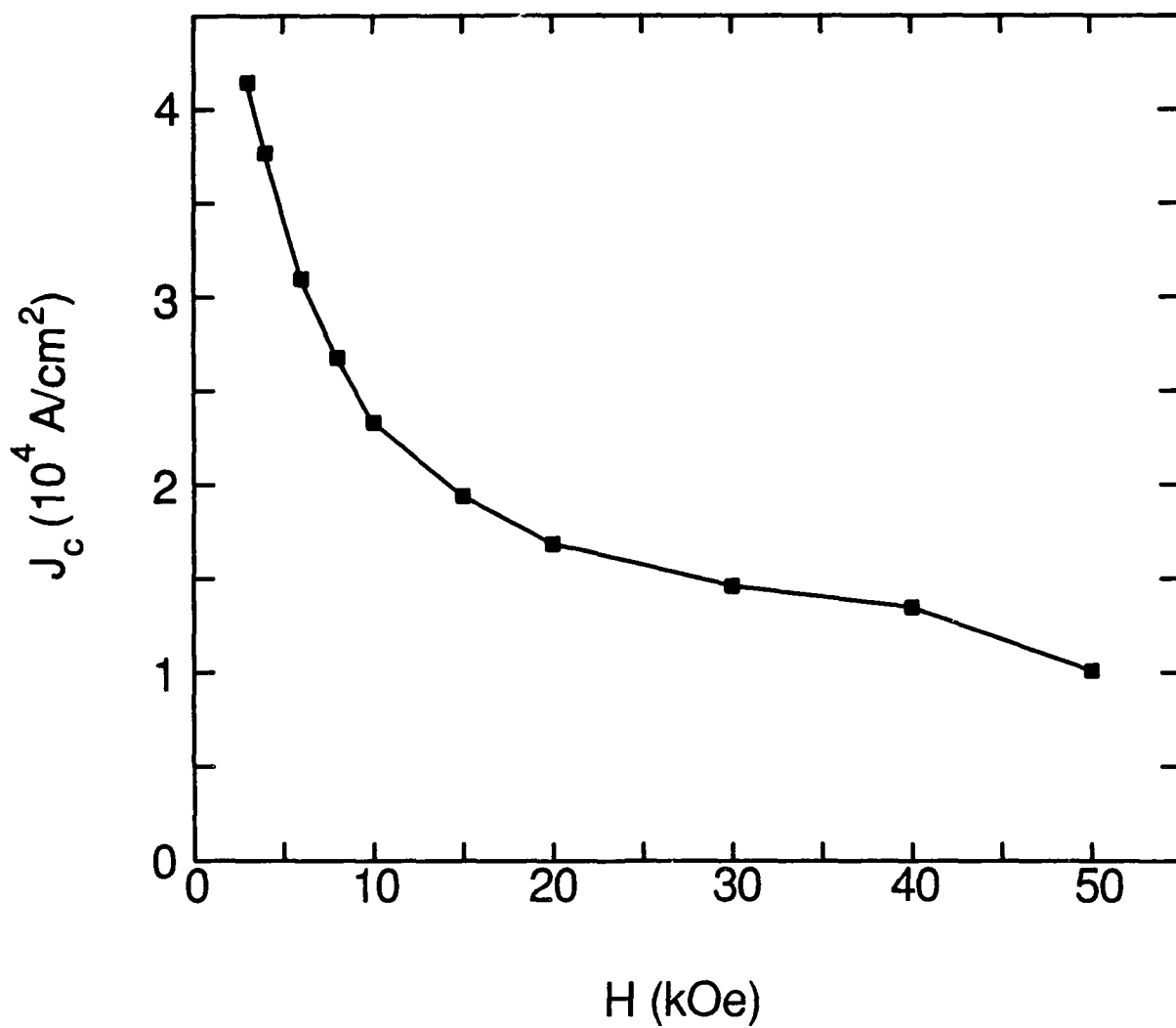


Fig. A-4-5. Estimated critical current density as a function of the applied field at 50 KOe at 5K

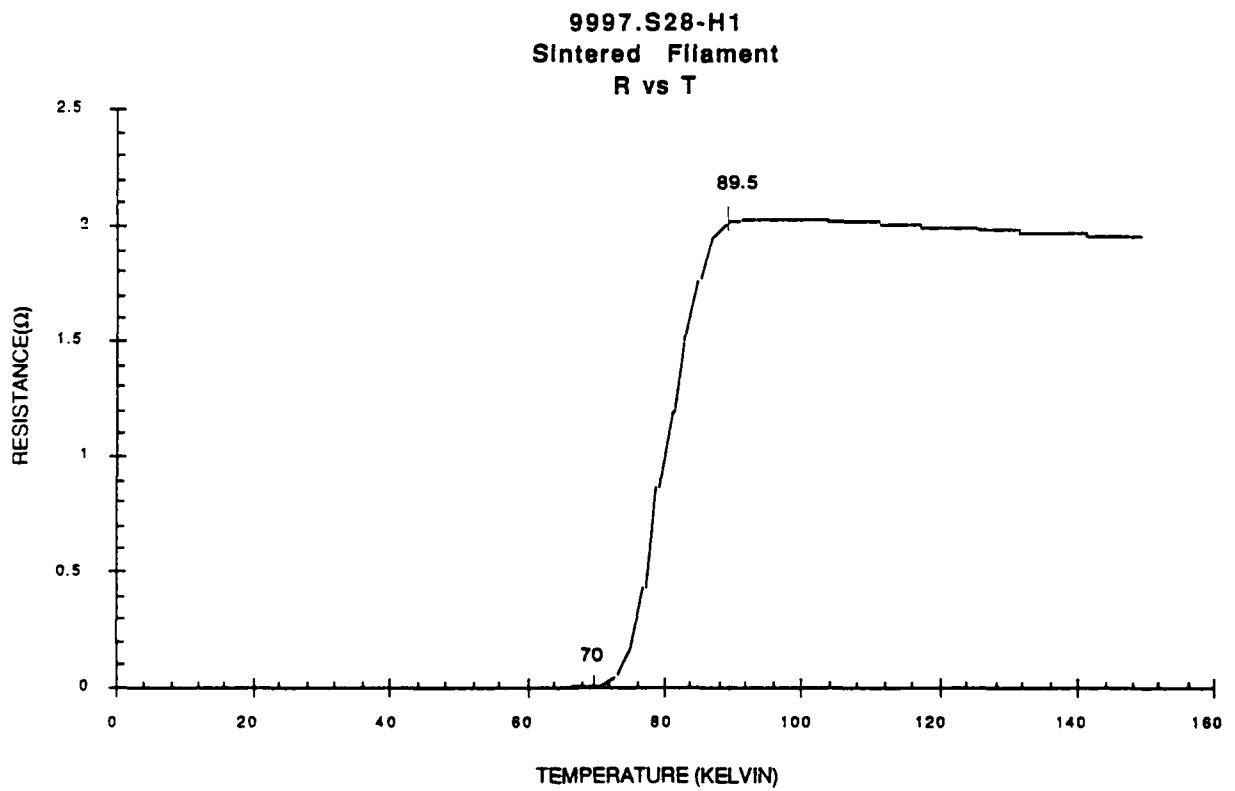


Fig. A-4-6. Resistance-temperature plot of sintered sol-gel derived fiber

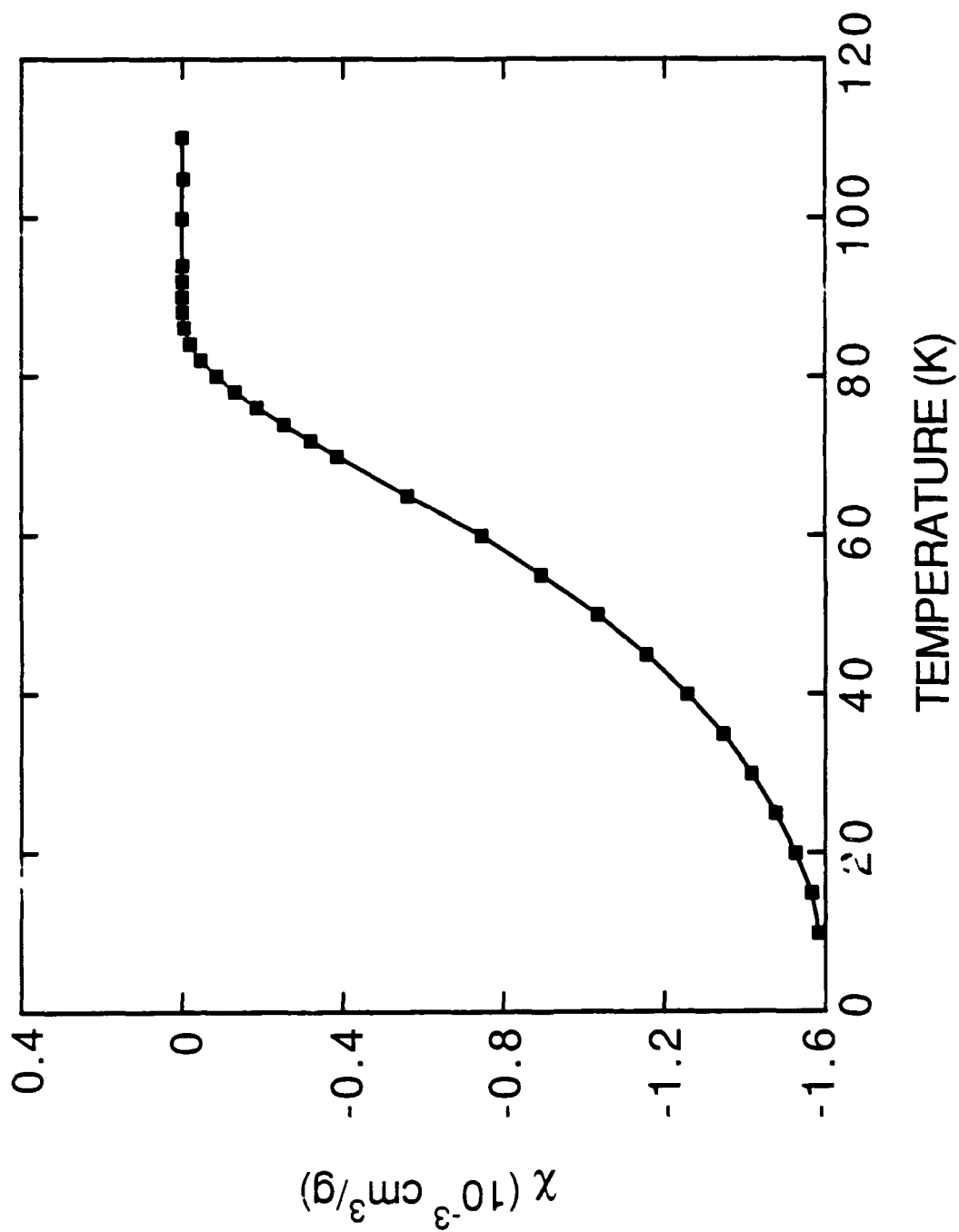


Fig. A-4-7. Magnetic susceptibility for the sol-gel derived 123 fiber

A.4.4. TECHNIQUE FOR MEASURING 123 RESISTIVITY AS A FUNCTION OF TEMPERATURE AT MICROWAVE FREQUENCY

The measurement of 123 resistivity at microwave frequencies as a function of temperature can be accomplished by constructing a microwave cavity in which the walls are coated with the material under test. If the cavity is driven by an external source at a frequency corresponding to one of its natural resonant modes, energy is transferred between the electric and magnetic fields of the resonance. A certain fraction of this stored energy is dissipated each cycle into the resistivity of the walls via the radio frequency (rf) currents associated with the electromagnetic wave structure. A useful figure of merit is the cavity's quality factor, or Q , for the mode under question which is given by:

$$Q = 2\pi \frac{\text{Stored Energy}}{\text{Energy Dissipated per Cycle}}$$
$$= \omega \frac{U_{\text{stored}}}{P_{\text{dissipated}}}, \quad (4-1)$$

where ω is the radian frequency of the resonant mode of interest. Numerous methods exist in the microwave art of the measurement of cavity Q , some of which will be discussed below, however, all require that the user is aware of all power dissipation mechanisms involved, and not just the dissipative wall losses, and that proper experimental technique is followed to separate out these other loss mechanisms.

One difficulty in the implementation of high Q cavities is the prevention of rf leakage at the mechanical joints where the cavity is assembled. This occurs because almost all modes, regardless of cavity shape, contain electromagnetic fields whose resultant wall currents perpendicularly cross these joints in at least some regions. One notable exception to this is the circular cylindrical TE_{0n1} family of modes. These modes are relatively insensitive to the tight tolerance fitting, joining, and clamping at the joints of other modes, even for high Q , low loss designs. This constructional advantage is particularly attractive for cryogenic designs that must undergo large temperature

excursion. For these reasons, we intend to begin construction on a TE₀₁₁ circular cylindrical cavity during the next reporting period.

The electric and magnetic fields (E and H, respectively) in the radial, azimuthal, and axial (r, θ , and z) directions for this cavity mode are given by:

$$E_{\theta} = E_0 J_1(k_c r) \sin(kz) e^{i\omega t} \quad , \quad (4-2)$$

$$E_r = E_z = H_{\theta} = 0 \quad , \quad (4-3)$$

$$H_r = -i \frac{k}{k_c} \frac{E_0}{Z_0} J_1(k_c r) \cos(kz) e^{i\omega t} \quad , \quad (4-4)$$

$$H_z = -i \frac{k_0}{k_c} \frac{E_0}{Z_0} J_0(k_c r) \sin(kz) e^{i\omega t} \quad . \quad (4-5)$$

The cutoff, free-space, and guide wave numbers are given by:

$$k_c = \frac{3.8317}{a} \quad , \quad (4-6)$$

$$k_0 = \frac{\omega}{c} \quad , \quad (4-7)$$

$$k = k_0^2 - k_c^2 = \frac{\pi}{L} \quad , \quad (4-8)$$

for a cavity of radius a and length L. The free space impedance, $Z_0 = 377$ ohms and the Js are the familiar Bessel functions of the first kind of order 0 and 1.

From these fields, we can calculate the cavity's stored energy, U, the wall loss, P, and the resulting Q:

$$U = \frac{\epsilon_0 \pi a^2 L}{8} E_0^2 J_0^2(k_c a) \quad , \quad (4-9)$$

$$P = \frac{\pi a L}{4k_0^2} \frac{E_0^2}{Z_0^2} R_s \left(k_c^2 + \frac{2a}{L} k^2 \right) J_0^2(k_c a) , \quad (4-10)$$

$$Q = a \sigma R_s \frac{k_0^2}{k_c^2 + \frac{2a}{L} k^2} = \frac{a}{\delta_{\text{skin}}} \frac{k_0^2}{k_c^2 + \frac{2a}{L} k^2} , \quad (4-11)$$

where R_s is the surface resistivity in ohms "per square," and the skin depth, δ_{skin} , is the e-folding distance for the rf wall currents into the imperfect conductor of conductivity σ .

We desire a test cavity with a TE_{011} resonance of 10 GHz. Although not critical, we choose the aspect ratio, $a/L = 0.766$, to minimize the cavity's internal surface area for coating. This then implies an internal diameter of 4.32 cm and an internal length of 2.82 cm. A high purity copper cavity at room temperature ($R_s = 26 \text{ m}\Omega$) of these dimensions would have an expected Q of 28,000. Work by Newman, et al. at NRL (APL 54, 389) showed an improvement of three in R_s for their high T_c material at 18 GHz. Since, as a first approximation, R_s varies as f^2 for a superconductor and as $f^{0.5}$ for conventional conductors, an improvement of 7.2, or $R_s = 3.6 \text{ m}\Omega$, might be expected for a similar experiment at 10 GHz. Since we intend to coat all internal conducting surfaces of our cavity, an overall Q of 200,000 is expected.

A troubling source of loss in many cavity Q measurements is the effect of the coupling probes or irises on the cavity resonance. This problem can be overcome by successively lessening the strength of the coupling. For example, using the two-probe transmission method, the most familiar of the Q measurement techniques, we desire a received signal strength of 1 mV from an HP 423B mic. detector diode, and furthermore assume a weak coupling factor of 0.01 (probe losses 1% of wall losses) into our $Q = 200,000$ cavity, a maximum H field of 11 A/m is developed on the superconductor and a source strength of 30 mW would be required, a level certainly feasible and requiring little amplification from commercial X-band synthesized signal generators.

Alternately, we could use a modification of the single port impedance technique of Q measurement (which reduces the complexity of the cryostat design) and measure the full width at half maximum of the reflected signal as the coupling is increased. At the critical point at which no reflection is detected, the measured Q is half of that due to wall losses alone and much smaller signal strengths are involved.

Barring any theoretical constructs that may limit our Q to 200,000, even higher Qs may be obtainable with improvements in coating purity and surface preparation. (Superconducting niobium cavities for use in particle accelerator research have demonstrated Qs of 10^9 at these frequencies.) For such narrow bandwidths, the cavity Q is more easily measured in the time domain, using the decrement method in which the ring-down time is measured following a pulsed stimulus.

A.4.5. CAVITY Q MEASUREMENTS

We have completed the design of the first 10 GHz TE_{011} cavity, Fig. A-4-8, and the parts are being machined now. The cavity is designed to fit inside our Janis Supravaritemp gas-flow cryostat; the cavity will be sealed by indium O-rings, pumped out through the central hole and backfilled with helium exchange gas. The two coaxial leads will be indise stainless steel tubes brazed into holes in the top of the cavity. The leads will be sealed at the top of the cryostat in such a way that they can still be moved up and down inside the tubes. The first cavity is being made of OFHC copper, polished to a mirror finish, and gold-plated to protect it against corrosion.

The Q of a TE_{011} cavity is given by

$$Q = R_s \sigma a / [(\lambda_0 / \lambda_c)^2 + (2a/L)(\lambda_0 / \lambda_g)^2] = (a/\delta) / [(\lambda_0 / \lambda_c)^2 + (2a/L)(\lambda_0 / \lambda_g)^2]$$

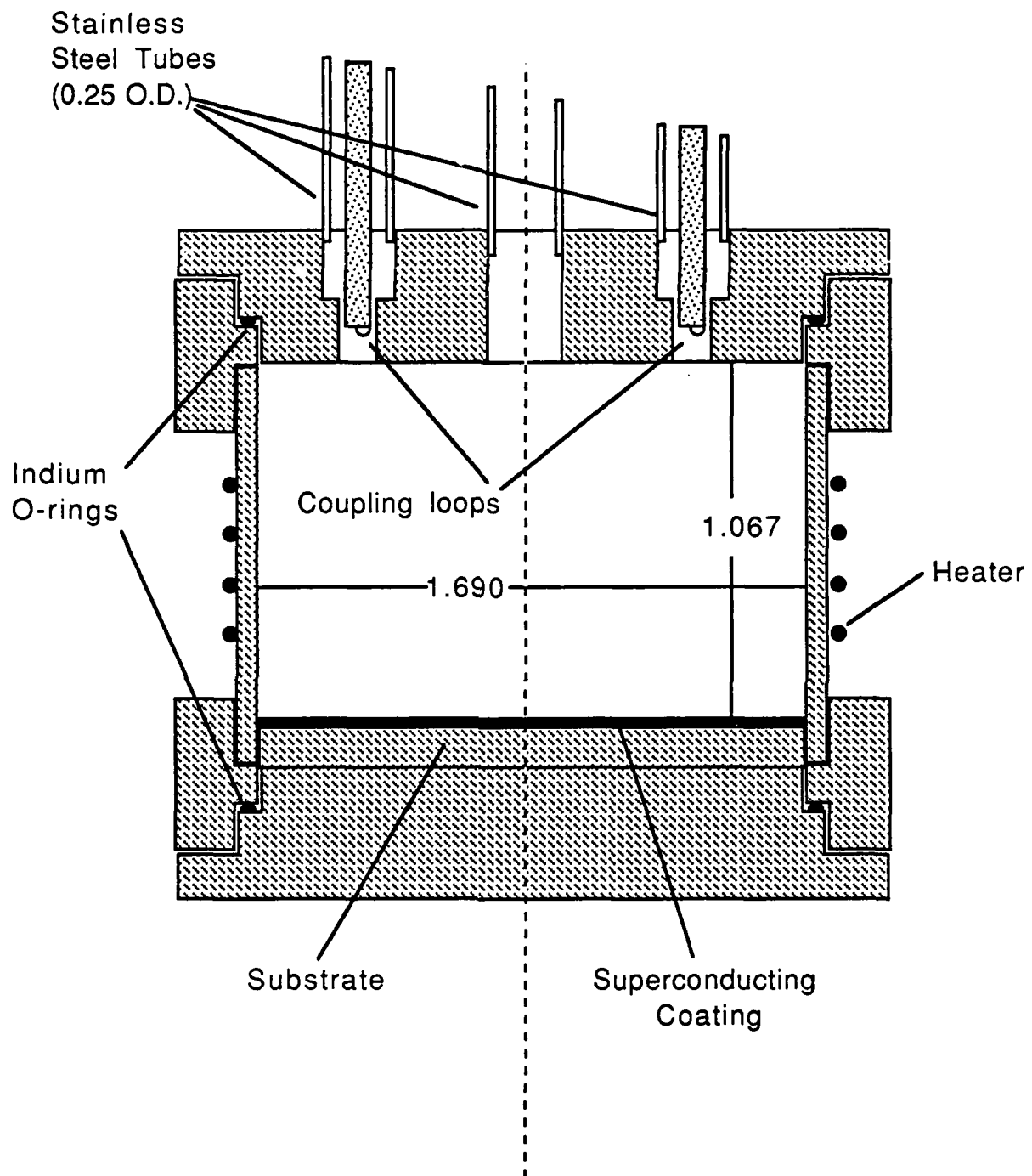


Fig. A-4-8. Schematic drawing of a cavity design to be coated with ceramic superconductors

where a and L are the inner radius and length of the cavity, respectively, and $R_x = 1/(\sigma\delta)$ are the dc conductivity, skin depth, and surface resistance in the walls of the cavity, respectively, λ_0 is the free space wavelength, $\lambda_c = 2\pi a/p_{01} = 3.8317$ is the first zero of the derivative of the zero order Bessel function, and $\lambda_g = \lambda_0[1-(\lambda_0/\lambda_c)^2]^{-1/2}$ is the guide wavelength.

The final dimensions chosen for the cavity are $a = 2.146$ cm (1.690 in.) and $L = 2.711$ cm (1.067 in.); this gives a resonant frequency of 10.16 GHz. Using the textbook value (N. Ashcroft and D. Mermin, Introduction to Solid State Physics, Saunders College, Philadelphia, PA, 1976) for the conductivity of gold, $\sigma = 5.0 \times 10^5$ (Ω -cm) $^{-1}$ at room temperature and $\sigma = 2.0 \times 10^6$ (Ω -cm) $^{-1}$ at liquid nitrogen temperature, gives unloaded Q's of 31000 and 62000 at room temperature and liquid nitrogen temperature, respectively, if the small perturbation due to the central hole in the top plate is not considered.

The most important effect of the central hole in the top plate is to decrease the resonant frequencies for the two TM_{010} modes, which would otherwise be degenerate with the desired TE_{011} mode, so that they are well away from the desired resonance. Calculations for very similar cavities (S. Sridhar, J. Appl. Phys. 63, 159, 1988) show that each TM_{010} mode should be shifted by at least 20 MHz. The Q for the TE_{011} mode would have to be below 500 for the resonant frequency of the nearest TM_{010} mode to fall inside the 3 dB points. The lack of azimuthal symmetry due to the coupling holes and the small gaps between the end plates and the cylinder will lift the degeneracy further. Since currents flow between the end plates and the cylinder in both TM_{010} modes but not in the TE_{011} mode, the small gaps between the end plates and the cylinder will act as mode traps: they will lower the Q of the TM_{010} modes without affecting the Q of the TE_{011} mode.

A.5. THE EFFECT OF FLUX CREEP ON THE SURFACE RESISTANCE OF HIGH T_c SUPERCONDUCTORS

A.5.1. INTRODUCTION

Ceramic oxide superconductors have both low pinning strength, because of their short coherence length and low carrier density, and a high operating temperature compared to conventional superconductors. As a consequence, magnetic flux can creep by thermal activation over relatively low barriers. This phenomenon, which is relatively hard to detect in conventional superconductors (Ref. 21), can dominate the transport properties in the ceramic oxides (Ref. 22), as a result, one never achieves a true zero resistance state in these superconductors (Ref. 21), and the usefulness of these superconductors depends on the tolerance of flux motion in each specific application.

In the sections which follow, expressions are developed, roughly following the lead of the Anderson-Kim model (Refs. 23 and 24), which describe the effect of flux motion in the superconductors. As a result of two years of frantic work since the original discovery of these superconductors, most of the parameters in these equations are reasonably well known. One, the flux attempt frequency, is not known and will be used to fit the equations to reliable transport measurements. Finally, using the fitted equations, we make predictions about the surface resistance at high frequencies.

A.5.2. FLUX CREEP EQUATIONS

Here a line of analysis advanced by Anderson (Ref. 23) and Kim (Ref. 24) is used. Additionally, the discussions of Campbell and Evetts, (Ref. 25) as applied to the ceramic oxide superconductors by Yeshurun and Malozemoff (Ref. 26), are heavily emphasized. However, for the purpose of this discussion, the main theme of their argument is applied in a somewhat different direction by focussing on the relatively low field requirements for a cavity application and by considering the

effect of the flexibility of flux lines as defined by Campbell and Evetts (Ref. 8) and Kramer (Ref. 27).

The energy cost, U_{pin} , of moving a magnetic flux bundle from some pinning site, which is not superconducting, into a completely superconducting volume ought to scale with the energy required to force (from the presence of the flux bundle) some of the superconductor into the normal state (Refs. 21 and 26). The change in the superconducting volume is proportional to the volume of the pinning centers which the flux left behind. Their minimum size is set by the superconducting coherence length ξ , and the Helmholtz free energy density of an extreme Type II superconductor (the Ginzberg-Landau parameter $\kappa \gg 1$) has the form (Ref. 26)

$$-(f_s - f_n^h) = \frac{\frac{1}{2} \mu_0 (H_{c2} - B/\mu_0)^2}{[1 + (2\kappa^2 - 1) \beta_A]} \cong \frac{1}{2} \mu_0 H_c^2 (1 - h)^2, \quad (5-1)$$

where $H_{c2} = \sqrt{2\kappa} H_c$ is the upper critical field and H_c is the thermodynamic critical field, $h = H/H_{c2}$. The pinning energy is thus

$$U_{pin}^{point} = \frac{1}{2} \mu_0 H_c^2 \xi^3 (1 - h)^2. \quad (5-2a)$$

We assume that the pinning sites are present at a density of $1/d_{26in}$. If the minimum flexible length of a flux bundle, $s < d_{pin}$ (see Appendix A.1), then the flux bundle can hop from one pinning site at a time, and the activation energy for hopping is given by Eq. 2a. If $s > d_{pin}$, then the rigidity of the flux bundle forces it to hop from all the pinning sites within that length, n_p , simultaneously, so Eq. 5-2a changes to:

$$U_{pin}^{point} = \frac{1}{2} \mu_0 n_p H_c^2 \xi^3 (1 - h)^2. \quad (5-2b)$$

That same rigidity prevents the bundle from being pinned except by sites within ξ of its flexing distance, d_{disp} . As a result, $n_p \approx 1$ up to $s_0 \approx$

$d_{pin} (d_{pin}/\xi)^2$, and only then increases $n_p \propto s/s_0$ (see Appendix A.2). Hereafter, the flux lattice will be considered floppy if $s < d_{pin}$, and rigid if $s > d_{pin}$. In the latter case, the distance between effective pinning sites is increased to $d_{pin}^* \approx s$ up to $s = s_0$.

Now, suppose the superconductor carries a current J and the bundle contains a field B . Then the flux bundle experiences a Lorentz force which tries to displace it from the pinning center. The pinning center experiences a force:

$$F_{magn} = BJA_s = J\Phi_0 d_{pin}^* \quad , \quad (5-3)$$

where $A = a_0^2$ is approximately the cross section of the flux lattice surrounding each bundle, and we assume that each bundle carries only one quantum of flux. The flux is shifted inside the pinning site until the restoring force caused by the gradient of the potential well restores equilibrium. It unpins only when the Lorentz force equals the maximum force exerted by the potential well, $F_{pin} \approx U_{pin}/\xi$. From that one gets

$$F_{pin} = J_c^0 \Phi_0 d_{pin}^* = U_{pin}/\xi \quad , \quad (5-4)$$

where $J_c^0 = U_{pin}/(\xi \Phi_0 d_{pin}^*)$ is the critical current in the absence of flux creep.

The current tilts the potential well of the pinning sites, as shown in Fig. 5-1, so that

$$\begin{aligned} U^+(J) &= (U_{pin} + J\Phi_0 d_{pin} d_{pin}^*) \\ &= U_{pin} [1 + (d_{pin}/\xi) (J/J_c^0)] \quad , \end{aligned} \quad (5-5a)$$

$$U^-(J) = (U_{pin} - J\Phi_0 \xi d_{pin}^*) = U_{pin} (1 - J/J_c^0) \quad . \quad (5-5b)$$

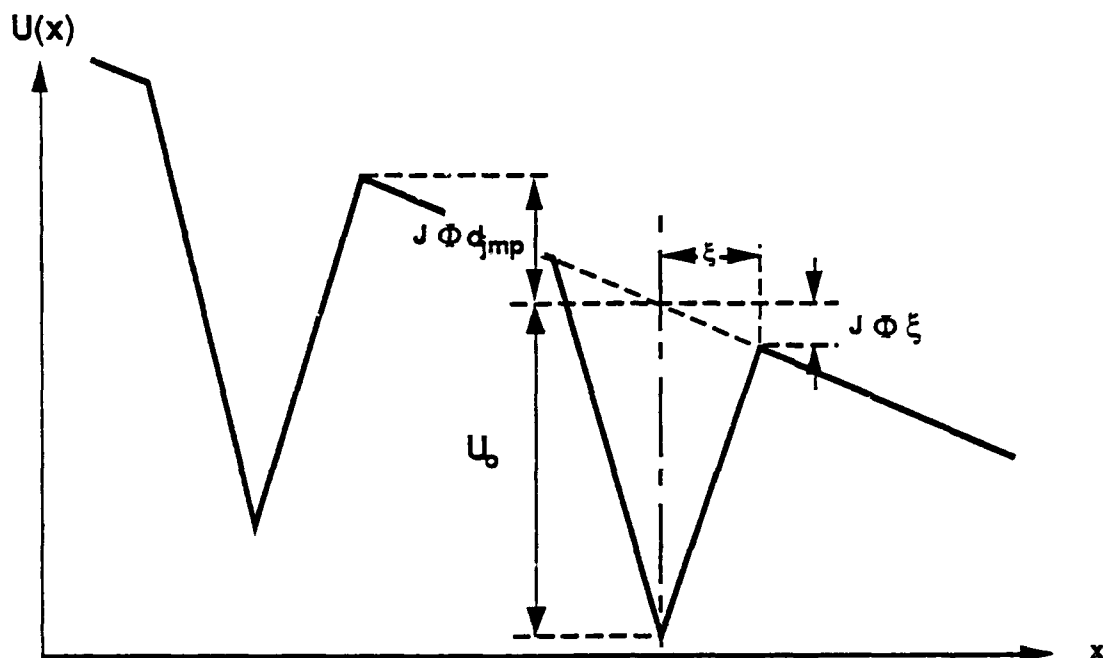


Fig. A-5-1. Effect of Lorentz force $J \times B$ on the energy barrier to a unit length of flux bundle in a pinning site. The initial barrier has a height of U_0 and a width of ξ . The pinning sites are separated by a distance d_{pin} . Each bundle contains one quantum, Φ_0 of flux.

When $J = J_C^0$, flux flows without a barrier - it need not be thermally activated, and the flux motion is limited by the dissipative forces (viscosity) involved in moving flux through a superconductor (Ref. 4).

The net diffusion velocity of the flux lines is the difference in the probability of jumps in the opposite direction times an attempt frequency, Ω , and a jump distance, $d_{\text{jmp}} \cong d_{\text{pin}}$. Since the distance to a maximum in the potential is ξ in one direction and d_{pin} in the other (Ref. 11), the equation is somewhat messy:

$$v_{\text{pin}} = \Omega d_{\text{pin}} \exp \frac{\xi}{d_{\text{pin}}} x - \exp(-x) \exp - \frac{U}{T} , \quad (5-6a)$$

where

$$x = \frac{d_{\text{pin}}}{\xi} \frac{J}{J_C^0} \frac{U}{T} .$$

One would expect $d_{\text{pin}}/\xi > 1$, so one can ignore the backward hops except at the highest temperatures and lowest currents (e.g., $xd_{\text{jmp}}/\xi < 1$), where Eq. 5-6a takes the limiting forms:

$$v_{\text{pin}} = \Omega d_{\text{pin}} \exp - \frac{U}{T} (1 - J/J_C^0) \quad x > 1 , \quad (5-6b)$$

$$v_{\text{pin}} = \Omega d_{\text{jmp}} \left[1 + \frac{d_{\text{pin}}}{\xi} \frac{J}{J_C^0} \frac{U}{T} \exp - \frac{U}{T} \right] \quad x < 1 . \quad (5-6c)$$

Equations 5-6a through 5-6c are valid so long as the flux is strongly pinned: flux spends more time pinned than moving between pinning sites. In the weak pinning case, viscous forces limit the flux speed to

$$v_{\text{visc}} = J \Phi_0 / \eta = J \rho_n / H_{c2} , \quad (5-7)$$

where η is the viscosity and ρ_n the normal resistance (Ref. 21). For intermediate strength pinning, the average flux velocity is

$$v_{flux}^{-1} = v_{pin}^{-1} + v_{visc}^{-1} \quad (5-8)$$

If we assume that v_{pin} will dominate in any region in which we are interested, we can take $v_{flux} = v_{pin}$.

The electric field, E , generated by the flux motion is just

$$E = B v_{flux} = E_0 \exp - \frac{U}{T} (1 - J/J_c^0) \quad x > 1, \quad (5-9a)$$

$$= E_0 \frac{J}{J_c^0} \left(1 + \frac{d_{pin}}{\xi} \right) \frac{U}{T} \exp - \frac{U}{T} \quad x < 1, \quad (5-9b)$$

where $E_0 = B \Omega d_{pin}$. Solving for J_c one finds

$$J_c \cong J_c^0 [1 - (T/U) \ln (E_0/E)] \quad x > 1, \quad (5-10a)$$

$$\cong J_c^0 \frac{E}{E_0} \frac{1}{1 + \frac{d_{pin}}{\xi}} \exp - \frac{U}{T} \quad x < 1. \quad (5-10b)$$

The size of the "critical current" J_c depends on the measurement limits for the electric field E . That is, these "super" conductors still have a finite resistance.

A.5.3. SUPERCONDUCTING RESISTANCE - ZERO FREQUENCY

Going back and solving the above equations for resistance, one finds that in the absence of pinning, the viscosity for flux motion for the superconductor yields a large resistance that is linear in B and T (the latter through the temperature dependence of ρ_n):

$$\rho_s = \frac{E}{J} = \rho_n \frac{B}{H_{c2}} \quad (\text{no pinning sites}) \quad (5-11)$$

$$\approx 0.01 \mu\Omega\text{-m at 1 Tesla} \quad .$$

This is no better than copper!

The presence of pinning makes things more complicated. For dc currents, the flux cannot move without hopping out of pinning sites. The hopping rate rapidly becomes very small as T decreases. One can get a feeling for this situation by looking at Eq. 5-9. For high temperatures and/or for low currents (e.g., $UJ_{d_{pin}} < \xi J_c^0 T$), Eq. 9b can be rewritten as

$$\rho \cong \rho_0 \frac{U}{T} \exp - \frac{U}{T} \quad , \quad (5-12)$$

where

$$\rho_0 = \frac{E_0}{J_c^0} \cong 2 \frac{\Phi_0 B}{\mu_0 H_c^2} \frac{d_{pin}^3}{\xi} \Omega \quad . \quad (5-13)$$

Flux is only weakly pinned at high temperatures, so the resistance in that case is limited by the viscosity for flux flow in the superconductor

$$\rho_{flux}^{-1} = \rho_{pin}^{-1} + \rho_{visc}^{-1} \quad . \quad (5-14)$$

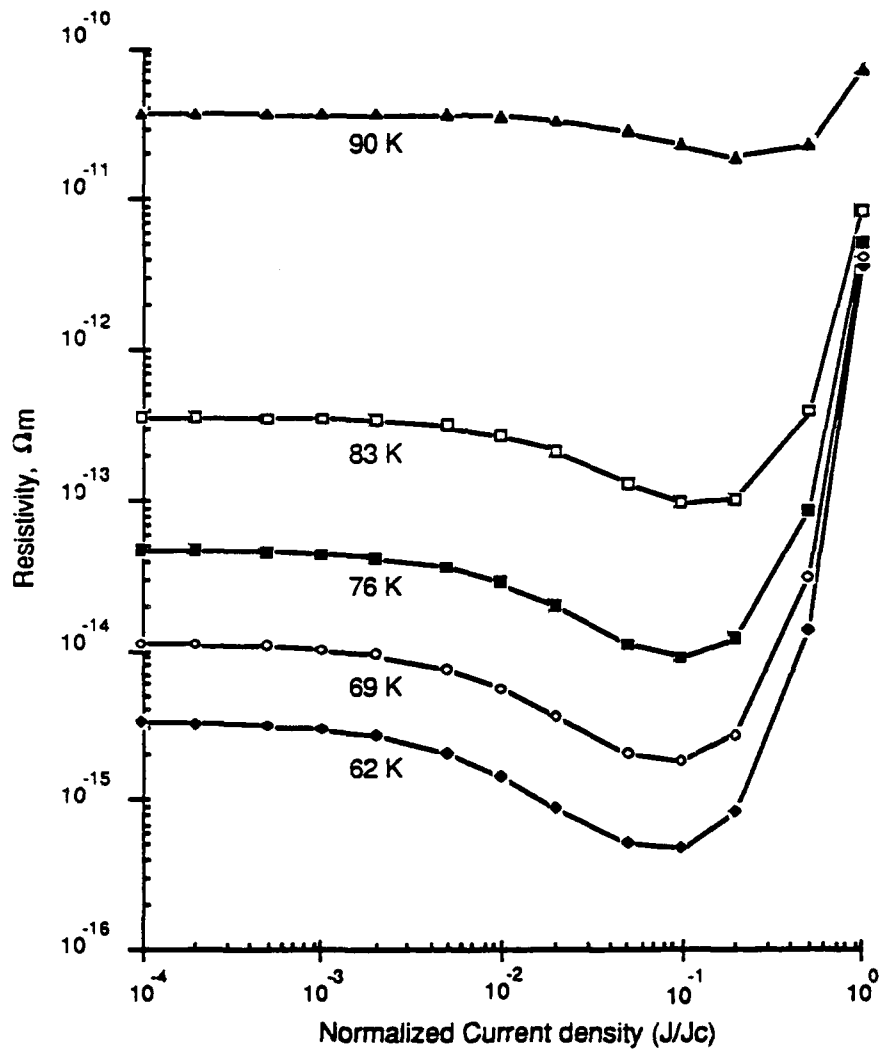


Fig. 5-2. Effective resistivity from flux creep for a high T_c superconductor with $T_c = 92$ K, $\xi_{\perp} = 2.5$ nm, $\xi_{\parallel} = 0.5$ nm, and $H_c = 0.82$ T (this gives $U_0 \approx 0.05$ eV), and $d_{pin} = 1.5$ nm. $\Omega = 10^9$ s $^{-1}$ to force J_c between 10^{10} and 10^{11} A/m 2 .

The resistivity, E/J , was calculated from Eq. 5-9 and plotted in Fig. 5-2 using the following parameters: $H_c = 0.82$ eV (Ref. 29) and ξ_{\perp} and $\xi_{\parallel} = 0.5$ and 2.5×10^{-9} m (Ref. 30) which give $U_0 = 0.05$ eV, $d_{pin} = 1.5 \times 10^{-8}$ m (Refs. 30 through 32), $\Omega = 10^9$ s $^{-1}$; the last was chosen to give $J_c^0 \approx 10^6 - 10^7$ A/cm 2 at 0 K. With this combination of parameters, and a field of 0.1 Tesla,

$$E_0 \approx 1.5 \text{ V/m in Eqs. 5-9 and 5-10}$$

and

$$\rho_0 \approx 7.8 \times 10^{-11} \text{ } \Omega\text{-m in Eq. 5-12}$$

All of the above parameters are temperature dependent. The Ginsberg-Landau forms are a reasonable approximation to the observed behavior (Ref. 33) and were used in the calculation of the curves in Fig. 5-2: H_c and $H_{c2} \propto (1 - t^2)$, $\xi \propto \sqrt{(1 + t^2)/(1 - t^2)}$, and $U \propto (1 + t^2)^{3/2} (1 - t^2)^{-1/2} (1 - b)^2$, where $b = H/H_{c2}$. In addition, $\rho_0(T) = \rho_0 [(1 + t^2) (1 - t^4)]^{-1/2}$. One can see that at low currents, the resistance is constant, and its value decreases rapidly with temperature. It increases dramatically as one approaches J_c .

A.5.4. SUPERCONDUCTING RESISTANCE - HIGH FREQUENCY

For ac currents, the resistance does not disappear even for completely pinned flux. The pinning sites have a finite size, ξ , and the flux lines can move back and forth within them. There is a restoring force retarding the motion of the flux that will eventually bring them to a halt, so we assume that on the average, the flux bundles move at about half the speed they would if free. With this model, each cycle causes a resistance $Bv_{\text{visc}}/2J$ for time $2\xi/v_{\text{visc}}$. In multiplying by cycles per second, one has for the loss from this source:

$$\rho_s(\omega) = \frac{\omega \xi B}{J} \quad (5-15)$$

This only dominates at frequencies such that

$$\omega > \frac{v_{\text{visc}}}{2\xi} \quad (5-16)$$

at which point $\rho_s(\omega)$ approaches half that of unpinned flux. It increases further for higher frequencies until the flux is effectively completely unpinned; the analytic form of this increase depends on the shape of the pinning potential well.

AC currents cause resistance even at low frequencies. This is especially visible in the floppy case; the flux lines distort and move freely in between the pinned locations (Fig. 5-3). If we assumed that the Lorentz force applied to the flux bundle between pinning sites stretches it until the restoring force equals the Lorentz force the shape (Ref. 27) of the bowed flux line is

$$y(x) = \frac{f_p}{2sC_{66}} \frac{\cosh(x/s)}{\sinh(d_{\text{pin}}^*/2s)} \quad (5-17)$$

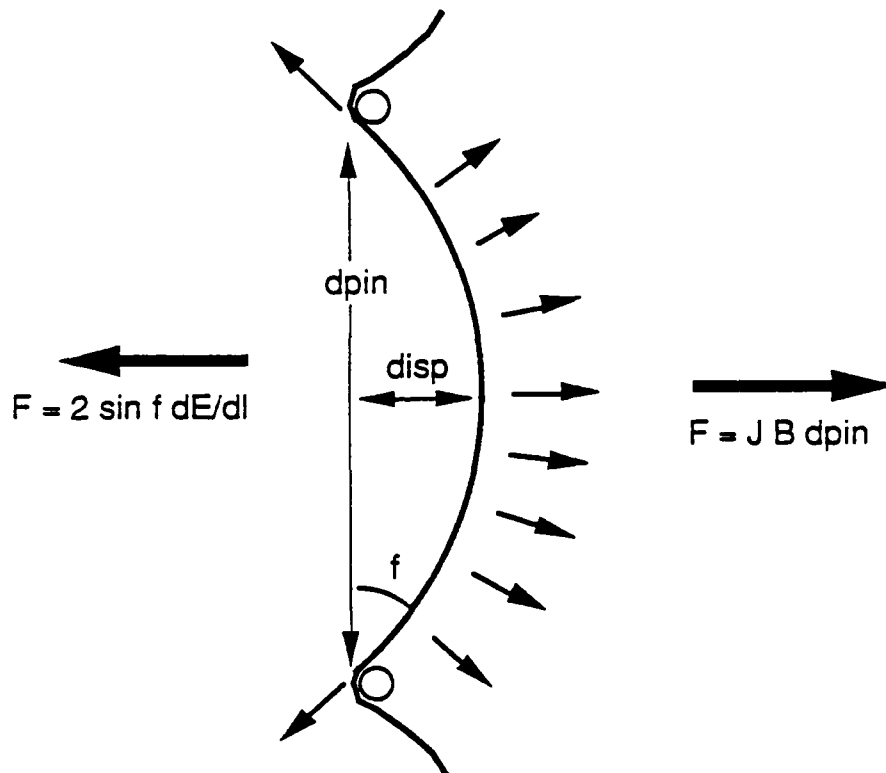


Fig. 5-3. When flux lines are floppy, the Lorentz force bows them out between pinning sites. The stretching force is normal to the curve at every point, so not counting the rigidity of the flux lines, the flux bundle is roughly bent into the arc of a circle. For small forces, the flux displacement in the center is $d_{disp} = f_p / C_{66} \frac{d_{pin}^*}{4s^2}$ (Ref. 10)

The amplitude of this motion, d_{disp} , increases with the separation between sites, d_{pin} , and decreases with the square of the minimum flexible length s (see Appendix A.1). This causes a motion just as described in Eqs. 5-15 and 5-16, except that only about half of the line moves to the full extent, and ξ is replaced by d_{disp} . As a result, the resistance is larger and the saturation frequency is much lower.

$$\rho_s = f_{pin} \frac{\omega B d_{disp}}{4s^2} , \quad (5-18)$$

$$\omega > \frac{v_{visc}}{d_{disp}} . \quad (5-19)$$

The above are very crude models. A more sophisticated analysis, based on rf studies (Refs. 34 through 36) of conventional Type II superconductors, has shown that flux pinning is effective below a frequency (Refs. 35 and 36)

$$\omega \approx \frac{\rho_n U_{pin}}{E_{c2}} (B\Phi_0)^{-1/2} . \quad (5-20)$$

Because the superconducting parameters are quite different for the oxide superconductors considered here, Eq. 20 may not be valid.

We suggest that it is necessary to repeat the old experiments of measuring the surface resistance of the high T_c superconductors under the external applied magnetic field. Such experiments will yield information of the nature of the flux flow and pinning in the high frequency regime and will provide a different method to determine the critical magnetic fields of the new superconductors. Measurements of the ac resistivity as a function of frequency for the samples with different pinning strength will also be useful. This type of experiment can be done in a transmission line configuration. In particular, whether the critical frequency, ω , specified in Eqs. 5-16, 5-19, and 5-20, exists in the new superconductors, and its analytic dependence remain to be determined.

A.5.4.1. High Q Cavities. Finally we have the derived equations needed as result of flux motion (not including ω^2 term - that is in addition) to estimate the resistivity of superconductors as function of temperature at high frequency.

Suppose one wanted to drive a 10 GHz cavity in the TE_{011} mode with a Q of 10^5 . Such a cavity would be a cylinder approximately 2 cm in radius by 3 cm long that gives $V \approx 4 \times 10^{-3} \text{ m}^3$. Suppose one could tolerate a wall loss of 1 W. Energy lost per cycle is $P \approx 10^{-10} \text{ J}$. The energy density stored in the cavity is $E \approx PQ/V \approx 3 \times 10^{-3} \text{ J/m}^3$. Average field $B = \sqrt{2E\mu_0} \approx 10^{-5} \text{ T}$, so the fields are smaller than H_{c1} in this case, and magnetic fields only penetrate a magnetic field penetration length, λ_L ; one would have to reach energy densities of MJ/m^3 for flux to penetrate as bundles.

From

$$H \cdot dA = I \cdot dS \quad , \quad (5-21)$$

one can estimate the currents needed to contain these fields. Equation 5-21 reduces in the cylindrical case to $I \text{ (A/m}^{-1}\text{)} = 5 \times 10^6 / 2\pi$. $H(T)r(m) \approx 10 \text{ A}$ per unit length along a cylinder of radius r . The superconducting surface sets up this current in a layer whose thickness is the skin depth, $\delta \approx 0.2 \text{ } \mu\text{m}$, so the current density at the surface, $J \approx 5 \times 10^7 \text{ A/m}^2$. If power loss is $3 \times 10^{-4} \text{ W}$ for a surface area of $5 \times 10^{-3} \text{ m}^2$, then resistance can be $R = P/I^2 = 10^{-13} \text{ } \Omega\text{-m}$. One can see from Fig. 5-2 that if one only worries about the dc loss, these materials can operate up to 77 K.

Suppose the cavity had to have a Q of 10^{11} . Then the fields would be above H_{c1} and the flux would penetrate as bundles. The required current would also increase by 10^3 . The penetration depth now depends on how far the flux can penetrate in one cycle. At 10 GHz, that is far

less than λ_L . For the cavity described above: $J = 5 \times 10^9 \text{ A/m}^2$, $H_{c2} = 140 \text{ T}$, and using $\rho_n \cong 1 \mu\Omega\text{-m}$, one finds $\approx 4 \times 10^{11} \text{ s}^{-1}$ (Eq. 5-16), implying that at a frequency of 10^{10} s^{-1} , the flux lines would move a distance of $40 \xi \approx 4 \times 10^{-8} \text{ m}$ in a cycle. As a result, the field penetration length is still λ_L . The required surface resistance is now $\approx 10^{-19} \Omega\text{-m}$, and these materials cannot be used above about 40 K.

At sufficiently high frequencies, the flux lines behave as if they were not pinned. For the cavity described above: $J = 5 \times 10^9 \text{ A/m}^2$, $H_{c2} = 140 \text{ T}$, and using $\rho_n \cong 1 \mu\Omega\text{-m}$, one finds $\approx 4 \times 10^{11} \text{ s}^{-1}$ and $3 \times 10^9 \text{ s}^{-1}$ for Eqs. 5-16 and 5-19, respectively, implying that the flux lines would be effectively pinned at 10 GHz, but that they would flop back and forth freely; the surface resistance would be nearly that of copper unless the pinning density could be raised.

A.5.5. SUMMARY

We have shown that flux pinning is sufficient to reduce the surface resistance of the ceramic oxide superconductors to tolerable levels only in the dc limit. At microwave frequencies, the flux lines can distort with their pinning framework and contribute an unacceptable level of loss to the superconductor.

The model developed in this paper is rather simple and implies the same kind of ac losses in more conventional Type II superconductors. As they operate quite well at sufficiently low temperatures, it is clear that the model is incomplete and needs further investigation; at this stage it should be treated as a guide to future experiments, rather than a quantitative analysis.

TABLE A-5-1
MATERIAL PARAMETERS

Maximum pinning strength and thermal activation calculated for several Type II superconductors. Underlined numbers were calculated from the others.

		Y ₁₂₃ (\perp , \parallel to c-axis) (Ref. 29)	Pb-10% Tl (Ref. 38)	Nb-Ti (Ref. 39)	NbN (Refs. 13 and 40)	Nb ₃ Sn (Refs. 23 and 41)
H _{c0}	(Tesla)	0.82	0.08	0.25 (Ref. 26)	<u>0.19</u>	<u>0.48</u>
H _{c10}	(Tesla)	0.5, 0.005	--	--	0.0093	0.03
H _{c20}	(Tesla)	29, 140	0.2	13	15.8	23
T _{c0}	(°K)	90	7.2	9.5	16 (Ref. 43)	18
ξ_0	(nm)	0.5, 2.5	100	4	4.6	3
λ_0	(nm)	810, 94	200	300	440	65
κ_0		230, 36	1.8	70	60	22
k _B T _c	(eV)	0.007	0.0006	0.0007	0.0014	0.0016
U=H ² ξ^3	(eV)	0.02 (Ref. 22)	16	0.04	0.03	0.06
U _{exp}	(eV)	0.05 (Ref. 42)	1 to 2	--	--	--
k _B T _c /U	Maximum	0.1	0.00001	0.02	0.04	0.03
k _B T _c /U	Exptl	0.1	0.0006	-	--	--

APPENDIX II

A.II.1 MINIMUM FLEXIBLE LENGTH OF FLUX LINE, s [Derived from expressions in Kramer (Ref. 27)]

We define s as the distance between pinning pins such that the maximum flexing of the center of a flux line, $d_{\text{disp}} = \xi$. If $d_{\text{disp}} > \xi$, then the line could hop from a pinning site in the center of the line without hopping from either of its neighbors. The maximum force one can exert on the line is U_{pin}/ξ . The shape of the flux line is given by Kramer (Ref. 27) - in our notation, as

$$y(x) = \frac{U_{\text{pin}}}{2s \xi C_{66}} \frac{\cosh(x/2s)}{\sinh(d_{\text{pin}}/2s)} \quad , \quad (\text{A-1})$$

where the shear modulus C_{66} (n/m^2) = $1.5 \times 10^5 H_c^2(T) (1 - h)^2$, $h = H/H_{c2}$, $d_{\text{pin}} = s$, and $U_{\text{pin}} = 1/2 \mu_0 H_c^2 \xi^3 (1 - h)^2$. This displacement of the center relative to the ends is just

$$y(0) - y(1/2) = \frac{\mu_0 \xi^2}{6 \times 10^5 s} \frac{\cosh(1/2) - 1}{\sinh(1/2)} \quad . \quad (\text{A-2})$$

Setting $y(0) - y(1/2) = \xi$ and solving for s one finds:

$$s = 3.2 \xi \quad . \quad (\text{A-3})$$

A.II.2. DISTANCE BETWEEN EFFECTIVE PINNING CENTERS, d_{pin}^*

The only effective pinning sites lie within ξ of the maximum flex distance of the flux line. A flux line with pins separated by $2d_{\text{pin}}^*$ probes a volume $\xi d_{\text{disp}} d_{\text{pin}}^*$. The product of the volume probed and the density of pinning sites is the probability of finding a pinning center between the two original pinning sites. If the density of pinning centers is $1/d_{\text{pin}}^3$, then one finds

$$d_{pin}^* = d_{pin}^3 / \xi d_{disp} \quad . \quad (A-4)$$

One finds from Eq. A-1

$$d_{disp} = \frac{\mu_0 \xi^2}{6 \times 10^5 s} \frac{\cosh (d_{pin}^*/2s) - 1}{\sinh (d_{pin}^*/2s)} \quad . \quad (A-5)$$

Since $d_{pin}^*/2s < 1/2$, Eq. A-5 can be simplified to

$$d_{disp} = \frac{\mu_0 \xi^2 d_{pin}^*}{1.2 \times 10^6 s^2} \quad , \quad (A-6)$$

so

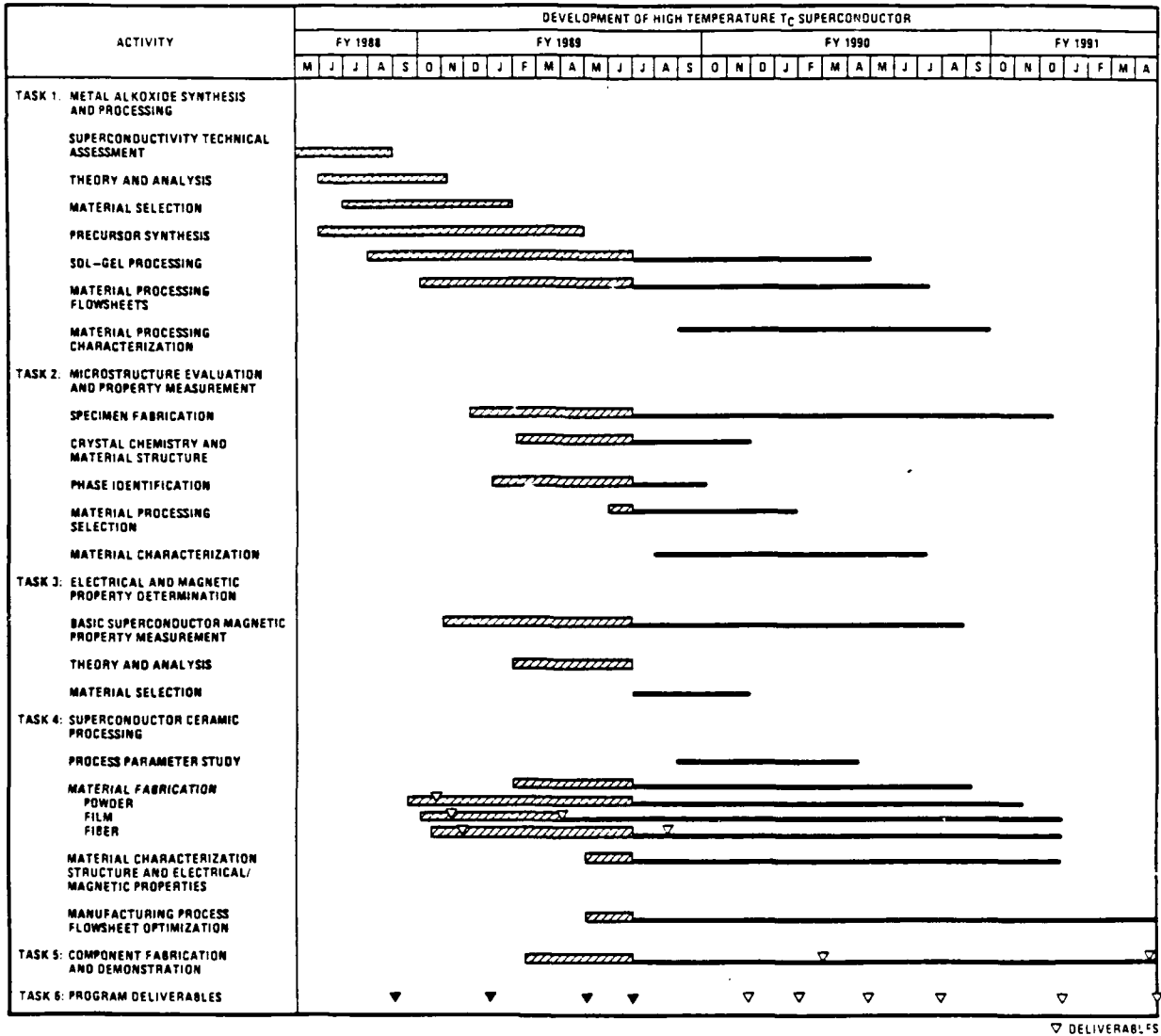
$$d_{pin}^* = 0.4 s \frac{d_{pin}^{3/2}}{\xi} \quad , \quad (A-7)$$

and

$$n_p = s/d_{pin}^* = 2.5 \frac{\xi}{d_{pin}^{3/2}} \quad . \quad (A-8)$$

One can see from Eq. A-8 that $n_p \cong 1$ unless the density of pinning sites is extremely high.

MILESTONES



6. REFERENCES

- 1a. C. W. Chu, et al., $\text{YBa}_2\text{Cu}_3\text{O}_7$, Science, 58, 405 (1987).
- 1b. J. S. Subramaman, $\text{Bi}_2\text{Sr}_2\text{CaCu}_2\text{O}_8$, Science, 239, 1015 (1988).
- 1c. Z. Z. Steg, et al., $\text{Tl}_2\text{Sr}_2\text{CaCu}_2\text{O}_8$, PR Letter 60(10), 937, 1988.
2. A. W. Sleight, Chemistry of High Temperature Superconductors
Science, Vol. 242. pp. 1519-1527, 1988.
3. Brown, L. M., and K. S. Mazdiyasni, Inorg. Chem., 9, 2783 (1970);
K. S. Mazdiyasni, L. M. Brown, and C. T. Lynch, US Patent
3,757,412, September 11, 1973.
Mazdiyasni, K. S., and L. M. Brown, US Patent 3,917,780, November
4, 1975; US Patent 3,923,675, December 1, 1975.
4. Horowitz, H. S., S. J. McLain, A. W. Sleight,, J. D. Druliner, P.
L. Gai, M. J. Vankavelaar, J. L. Wagner, B. D. Biggs and S. J.
Poon, Submicrometer, Superconducting $\text{YBa}_2\text{Cu}_3\text{O}_{(6+x)}$ by a Low
Temperature Synthetic Route,: Science, to be published.
5. Accibal, M. A., J. W. Draxton, A. H. Gabor, W. L. Gladfelter, B.
A. Hassler and M. L. Mecartney, "Comparison of several CFDu(I) and
 CU(II) Precursors for the Sol-Gel Preparation of High Tc
Superconducting Metal Oxides,, to be published.
6. Shibata, S., T. Kitagawa, H. Okazaki, T. Kimura and T. Murakami,
"Superconducting Oxides by the Sol-Gel Method using Alkoxides."
Japanese Journal of Applied Physics, 27(1), 153-154, 1988.
7. Laine, R. M., K. A. Youngdahl, W. M. Carty G. C. Stangle, C. Han,
R. A. Kennish, K. S. McElhancy, T. K. Yin, T. Yogo, M. Sarikaya
and I. A. Aksay, "Organometallic Precursors for the Fabrication of
High Tc Superconducting Fibers," J. of the American Ceramic
society, to be published.
8. Bertrand, J. A. and R. I. Kaplan, "Preparation and Properties of
 $\text{Di-u-methoxo-bis(2,4-pentanedionato)dicopper(II)}$," Inorganic
Chemistry, 4(11), N1657-N1659, 1965.

9. Neumeier, J. J., Dalichaouch, Y., Ferreira, J. M. Hake, R. R., Lee, B. W., Maples, M. B., Torikachvili, M. S., Yang, K. N., and Zhou, H., Appl. Phys. Lett. 51 (1987), 371.
10. Fahrenholtz, W. G., D. M. Millar, and D. A. Payne, "Preparation of $\text{YBa}_2\text{Cu}_3\text{O}_{7-x}$ from Homogeneous Metal Alkoxide Solution," Advanced Ceramic Materials, to be published.
11. Accibal, M. A., J. W. Draxton, A. H. Gabor, W. L. Gladfelter, B. A. Hassler, and M. L. Mecartney, "Comparison of Several Cu(I) and Cu(II) Precursors for the Sol-Gel Preparation of High T_c Superconducting Metal Oxides," to be published.
12. Vogel, A. I., Quantitative Inorganic Analysis, John Wiley and Sons, New York, 1961.
13. Kodama, K., Methods of Quantitative Inorganic Analysis - An Encyclopedia of Gravimetric, Titrimetric, and Colormetric Methods Interscience Pub, New York, 1963.
14. Neumeier, J. J., Dalichaouch, Y., Ferreira, J. M. Hake, R. R., Lee, B. W. Maples, M. B., Torikachvili, M. S., Yang, K. N., and Zhou, H., Appl. Phys. Lett. 51 (1987), 371.
15. Bean, Co Po., Phys. Rev. Lett. 8 (1962) 250.
16. Finnemore, K. K., Ostenson, J. E., Ji, L., McCallum, R. W., and Clem, J. R., to be published.
17. Fietz, W. A., Webb, W. W., Phys. Rev. 178 (1969) 657.
18. Shibata, S., T. Kitagawa, H. Okazaki, T. Kimura and T. Murakami, "Superconducting Oxides by the Sol-Gel Method using Alkoxides." Japanese Journal of Applied Physics, 27(1), 153-154, 1988.
19. Laine, R. M., K. A. Youngdahl, W. M. Carty, G. C. Stangle, C. Han, R. A. Kennish, K. S. McElhancy, T. K. Yin, T. Yogo, M. Sarikaya and I. A. Aksay, "Organometallic Precursors for the Fabrication of High T_c Superconducting Fibers," J. of the American Ceramic Society, to be published.
20. Ferreira, J. M., Maple, M. G., Zhou, H., Hake, R. R., Lee, B. W., Seamons, C. L., Kur'ic, M. V., and Guertin, R. P., Applied Physics A 47, 105 (1988).

- 21a. Tinkham, M., Introduction to Superconductivity, McGraw Hill, New York (1975).
- 21b. Tinkham, M., "Resistive Transition of High-Temperature Superconductors," Phys. Rev. Lett., 61, 1658 (1988).
22. Yesherun, Y., and A. P. Malozemoff, "Giant Flux Creep and Irreversibility in an Y-Ba-Cu-O Crystal: An Alternative to the Superconducting Glass Model," Phys. Rev. Lett., 21, 2022 (1988).
23. Anderson, P. W., Phys. Rev. Lett., 9, 309 (1962).
24. Kim, Y. B., Rev. Mod. Phys., 36, 39 (1964).
25. Campbell, A. M., and J. E. Evetts, "Flux Vortices and Transport Currents in Type II Superconductors," Phys. Rev., 181, 682 (1972).
26. Malozemoff, A. P., T. K. Worthington, Y. Yesherun, F. Holtzberg, and P. H. Kes, "Frequency Dependence of the AC Susceptibility in an YBaCuO Crystal: a Reinterpretation of H_{c2} ," Submitted to Phys. Rev., B (1988).
27. Kramer, E. J., "Scaling Laws for Flux Pinning in Hard Superconductors," J. Appl. Phys., 44, 1360 (1973).
28. Sun, J. Z., K. Char, M. R. Hahn, T. H. Geballe, and A. Kapitulnik, "Magnetic Flux Motion and Its Influence on Transport Properties of the High T_c Oxide Superconductors," App. Phys. Lett., 54, 663 (1989).
29. Worthington, T. K., W. J. Gallagher, and T. R. Dinger, "Anisotropic Nature of High-Temperature Superconductivity in Single Crystal $Y_1Ba_2Cu_3O_{7-x}$," Phys. Rev. Lett., 59, 1160 (1987).
- 30a. Kes, P. H., "Irreversible Magnetic Properties of High T_c Superconductors," Physica, C153-155, 1121 (1988).
- 30b. Kes, P. H., J. Aarts, J. van den Berg, C. J. van der Beek, and J. A. Mydosh, "Thermally Assisted Flux Flow at Small Driving Forces," to be published in Superconductor Science and Technology (1988).
31. Dolan, G. J., G. V. Chandrashekhar, T. R. Dinger, C. Feild, and F. Holtzberg, "Vortex Structure in $YBa_2Cu_3O_7$ and Evidence for Intrinsic Pinning," Phys. Rev. Lett., 62, 827; Pinning Structure on Scale <100 nm (1989).

32. Watanabe, K., H. Yamane, H. Kurosawa, T. Hirai, N. Kobayashi, H. Iwasaki, and K. Noto, "Critical Currents at 77.3 K Under Magnetic Fields up to 27 T for an Y-Ba-Cu-O Film Prepared by Chemical Vapor Deposition," Appl. Phys. Lett., 54, 575; Observed Maximum Pinning Strength at 9 T When B_{c2}
33. De Vries, J. W. C., G. M. Stollman, and M. A. M. Gijs, Analysis of the Critical Current Density in High- T_c Superconducting Films," to be published in Physica C (1989).
34. Cardona, M., G. Fischer, and B. Rosenblum, Phys. Rev. Lett., 12, 101 (1964).
35. Rosenblum, B., M. Cardona, and G. Fischer, RCA Review, 25, 491 (1964).
36. Gittleman, J. I., and B. Rosenblum, Phys. Rev. Lett., 16, 734 (1966).
37. Gallagher, W. J., T. K. Worthington, T. R. Dinger, F. Holtzberg, D. L. Kaiser, and R. L. Sandstrom, Physica, 14B, 228, Amsterdam (1987).
38. Beaseley, M. R., R. Labusch, and W. W. Webb, "Flux Creep in Type-II Superconductors," Phys. Rev., 181, 682 (1969).
39. Anderson, H. L., Ed., Physics Vade Mecum, AIP, New York (1981).
40. Roberts, B. W., J. of Phys. and Chem. Ref. Data, 5, 581 (1976).
41. Roberts, B. W., Properties of Selected Superconductor Materials: 1978 Supplements, NBS Techn. Note 983 (October 1978).
42. Dew-Hughes, D., "Model for Flux Creep in High T_c Superconductors," Cryogenics, 28, 674 (1988).
43. Kittel, C., Introduction to Solid State Physics, 3rd Ed., John Wiley & Sons, New York (1968).